Computational Investigation of Nanoscale Electrocatalysts for Clean Energy Conversion

Thesis by

Yalu Chen

In Partial Fulfillment of the Requirements for

the degree of

Doctor of Philosophy

Caltech

CALIFORNIA INSTITUTE OF TECHNOLOGY

Pasadena, California

2021

(Defended December 14, 2020)

Yalu Chen
ORCID: 0000-0002-0589-845X

ACKNOWLEDGEMENTS

The experience to pursue my graduate studies at Caltech has been special and unforgettable. I've been incredibly fortunate to meet so many talented people here, to whom I want to give a bounty of thanks.

I would first and foremost like to thank my advisor, Prof. William A. Goddard III, for the continued support and guidance throughout my graduate studies. Bill has always been warm and supportive, and given me a great amount of freedom to explore my own research interests. His sharp scientific intuition and true passion for science has inspired me a lot on my academic adventure. I'm extremely grateful to have Bill as my research advisor, my life mentor, and the best role model ever. I wish I could be a mentor like him one day.

My gratitude also extends to my thesis committee, Prof. Harry B. Gray, Prof. Brent Fultz, and Prof. Harry A. Atwater, for the time they dedicated to my thesis and research progress. Their insightful comments and encouragement have meant a lot to improve this thesis work.

Next, I want to thank Dr. Soo-Kyung Kim for the guidance on the Cargill project. I still remember the early days of my graduate school when Soo-Kyung patiently taught me everything about GPCR. I've also received an incredible amount of moral support from her during emotional tough times.

My sincere thanks then go to Dr. Yufeng Huang and Prof. Tao Cheng for introducing me to the world of electrocatalysis and machine learning, and for providing tons of valuable advice on many of the projects we worked on together. Those long hours of discussions on research, career, and life have helped me a lot to become a better scientist from a higher level.

I'm also thankful to my B207 officemates, Dr. Yufeng Huang, Dr. Jin Qian, Dr. Soonho Kwon, and Prof. Hyeyoung Shin, for all the funs we've had in the past four years. Thank you Yufeng again for being the best cycling and running buddy ever. Thank you Jin for helping me through the crazy MS coursework and for the numerous funny conversations over many different subjects. Thank you Soonho for organizing many activities and trips

outside the office. Thank you Hyeyoung for being such a great friend to share our life stories.

I would also like to thank the many other MSC group members who I have had the pleasure professionally, or personally interacted with: Dr. Daniel Brooks, Dr. Saber Naserifar, Prof. Qi An, Prof. Yuanyue Liu, Prof. Ravinder Abrol, Prof. Hai Xiao, Prof. Sijia Dong, Dr. Matthew Gethers, Shane Flynn, Charles Musgrave, and any name that I may have missed.

I also want to take the chance to thank all my friends met at Caltech or outside Caltech. They are just too many to name. My graduate life would not have been so enjoyable without them.

In the end, I want to thank my family for their unconditional love and support. Thank you for always supporting me in whichever path I choose to take.

To all the amazing people, thank you.

ABSTRACT

Electrocatalysis provides a practical solution to the increasing global energy demand while maintaining a sustainable environment. Recently nanoscale catalysts (nanoparticles, nanowires, and dealloyed surfaces) have been shown to have experimentally far superior performance than metallic crystals at sustainable energy conversion. However, the surface feature of these improved catalysts is still unknown, as the detection of the active sites directly from experiment has not been possible.

In this thesis work, we discuss using the quantum mechanics based muitiscale simulations and machine learning to understand the nature of these superior materials. We first studied jagged Pt nanowire (J-PtNW), which was shown to have performance at oxygen reduction reactions (ORR) 50 times better than Pt/C. We used multiscale simulations (reactive force field, and density functional theory) to explain this remarkably accelerated ORR activity from an atomistic perspective. Next, we looked into the irregular gold surfaces and copper surfaces (nanoparticles and dealloyed surfaces), which showed dramatically improved performance at CO_2 reduction reactions (CO2RR) and CO reduction reactions (CORR). We developed the strategy to combine the reactive force field, density functional theory, and machine learning to identify the active sites responsible for their improved performance. This approach provided the possibility to understand the highly irregular and disordered surface, which is impossible with surface science experiments or with quantum mechanics. The identification of the active sites provides insights into new design concepts (alloys, NP, NW, and electrolytes such as ionic liquids) aimed at increasing product selectivity and rates simultaneously with reducing energy requirements.

PUBLISHED CONTENT AND CONTRIBUTIONS

Huang, Y.; **Chen, Y.;** Cheng, T.; Wang, L.-W.; Goddard, W. A. Identification of the Selective Sites for Electrochemical Reduction of CO to C $_{2+}$ Products on Copper Nanoparticles by Combining Reactive Force Fields, Density Functional Theory, and Machine Learning. ACS Energy Letters 2018, 2983–2988. doi: 10.1021/jacs.9b13218

> Chen, Y. participated in the conception of the project, performed the calculations, analyzed the data, and wrote the manuscript.

Chen, Y.; Huang, Y.; Cheng, T.; Goddard, W. A. Identifying Active Sites for CO2 Reduction on Dealloyed Gold Surfaces by Combining Machine Learning with Multiscale Simulations. *J. Am. Chem. Soc.* 2019, *141* (29), 11651–11657. doi: 10.1021/jacs.9b04956

> Chen, Y. came up with the concepts, performed all the quantum mechanics calculations, developed the machine learning algorithm, analyzed the data, and wrote the manuscript.

Chen, Y.; Cheng, T.; Goddard III, W. A. Atomistic Explanation of the Dramatically Improved Oxygen Reduction Reaction of Jagged Platinum Nanowires, 50 Times Better than Pt. *J. Am. Chem. Soc.* 2020, *142* (19), 8625–8632. doi: 10.1021/acsenergylett.8b01933

> Chen, Y. came up with the concepts, performed the molecular dynamic simulations and quantum mechanics calculation, did the data analysis, and wrote the manuscript.

TABLE OF CONTENTS

LIST OF ILLUSTRATIONS

LIST OF TABLES

Chapter I

INTRODUCTION

1.1 STATEMENT OF THE PROBLEM

Electrochemical reduction of CO2 to fuels and chemical products[1-3], electrochemical conversion from hydrogen to electricity[4-6] are promising techniques to fulfill the increasing global energy demand while still maintaining a sustainable environment. The key barrier for these sustainable energy conversions is the development of efficient, selective, and stable catalysts.

Nanoscale catalysts have been shown to have experimentally far superior performance than metallic crystals. For example, Pt-alloy nanomaterials[7-12], especially PtNi alloys[13-14] have been shown to have enhanced performance. Researchers even observed dramatically improved performance in dealloyed Pt nanomaterials[15]. Similarly, the enhanced catalytic activity and selectivity have been observed at Copper nanomaterials for reducing CO to C2+ products[16] and at Gold nanomaterials for reduction CO2 to CO[17]. However, experimental synthesis and characterization of such nanoscale systems are difficult. The detection of the active sites responsible for the dramatically enhanced performance directly from experiment has not been possible.

Recently, the development of computational methods, such as density-functional theory, molecular dynamics etc., allows reliable prediction of material structures, energetics, and electronic properties of model systems. We and others have also recently demonstrated that machine learning methods provide a promising approach to enhance the link between experiments and computation in the surface sciences[18-20]. We discuss here to use the quantum mechanics based multi-scale simulations and machine learning to help us understand the nature of these superior nanomaterials. This can provide insights into new design concepts (alloys, NP, NW, and electrolytes such as ionic liquids) aimed at increasing product selectivity and rates simultaneously with reducing energy requirements.

1.2 ORGANIZATION OF THE THESIS

Proton Exchange Membrane Fuel Cells (PEMFCs) utilizing hydrogen (H2) and oxygen (O2) to produce electricity is one of the most promising means to address the global renewable energy supply and clean environment. To develop high performance and low cost electrocatalysts of oxygen reduction reactions (ORR) is crucial for its large-scale commercialization. In *Chapter II*, we describe using multiscale simulations to explain the dramatically improved ORR performance of Jagged PtNW (50 times better)[21].

Electrochemical CO2 reduction to fuels and chemical products provides solutions to the renewable energy supply while remediating CO2. Among all the products of CO2 reduction, CO is one of the most promising ones as it could serve as the intermediate to synthesize other hydrocarbon fuels. A significant improvement of Faraday Efficiency(FE) for reducing CO2 to CO at very low overpotentials has been demonstrated at AuNPs derived from Au oxide films. In *Chapter III*, we combine machine learning and multiscale simulations to identify active sites for CO2 reduction on nanoscale gold catalysts[22].

Copper is the only catalyst that can reduce CO or CO2 by more than two electrons to generate valuable products in nontrivial amounts. In *Chapter IV*, we then summarize the new methods of combining QM, ReaxFF reactive FF, and machine learning to explain improved selectivity and activity of Copper nanoparticle to reduce CO to C2+ Products[23].

BIBLIOGRAPHY

(1) Schuur, E. A. G.; McGuire, A. D.; Schädel, C.; Grosse, G.; Harden, J. W.; Hayes, D. J.; Hugelius, G.; Koven, C. D.; Kuhry, P.; Lawrence, D. M.; et al. Climate Change and the Permafrost Carbon Feedback. Nature 2015, 520 (7546), 171–179. https://doi.org/10.1038/nature14338.

(2) Foster, G. L.; Royer, D. L.; Lunt, D. J. Future Climate Forcing Potentially without Precedent in the Last 420 Million Years. Na-ture Communications 2017, 8, 14845. https://doi.org/10.1038/ncomms14845.

(3) van der Giesen, C.; Kleijn, R.; Kramer, G. J. Energy and Climate Impacts of Producing Synthetic Hydrocarbon Fuels from CO 2. Environmental Science & Technology 2014, 48 (12), 7111–7121. https://doi.org/10.1021/es500191g.

(4) Peighambardoust, S. J.; Rowshanzamir, S.; Amjadi, M. Review of the Proton Exchange Membranes for Fuel Cell Ap-plications. International Journal of Hydrogen Energy 2010, 35 (17), 9349–9384. https://doi.org/10.1016/j.ijhydene.2010.05.017.

(5) Steele, B. C. H.; Heinzel, A. Materials for Fuel-Cell Technolo-gies. Nature 2001, 414 (6861), 345–352. https://doi.org/10.1038/35104620.

(6) Wang, S.; Jiang, S. P. Prospects of Fuel Cell Technologies. Natl Sci Rev 2017, 4 (2), 163–166. https://doi.org/10.1093/nsr/nww099.

(7) Huang, X.; Zhao, Z.; Chen, Y.; Zhu, E.; Li, M.; Duan, X.; Huang, Y. A Rational Design of Carbon-Supported Dispersive Pt-Based Octahedra as Efficient Oxygen Reduction Reaction Catalysts. Energy Environ. Sci. 2014, 7 (9), 2957–2962. https://doi.org/10.1039/C4EE01082E.

(8) Peng, Z.; Yang, H. Designer Platinum Nanoparticles: Control of Shape, Composition in Alloy, Nanostructure and Electrocatalytic Property. Nano Today 2009, 4 (2), 143–164. https://doi.org/10.1016/j.nantod.2008.10.010.

(9) Wu, J.; Yang, H. Platinum-Based Oxygen Reduction Electrocata-lysts. Acc. Chem. Res. 2013, 46 (8), 1848–1857. https://doi.org/10.1021/ar300359w.

(10) Porter, N. S.; Wu, H.; Quan, Z.; Fang, J. Shape-Control and Elec-trocatalytic Activity-Enhancement of Pt-Based Bimetallic Nano-crystals. Acc. Chem. Res. 2013, 46 (8), 1867–1877. https://doi.org/10.1021/ar3002238.

(11) Wang, D.; Xin, H. L.; Hovden, R.; Wang, H.; Yu, Y.; Muller, D. A.; DiSalvo, F. J.; Abruña, H. D. Structurally Ordered Intermetal-lic Platinum-Cobalt Core-Shell Nanoparticles with Enhanced Ac-tivity and Stability as Oxygen Reduction Electrocatalysts. Nat Ma-ter 2013, 12 (1), 81–87. https://doi.org/10.1038/nmat3458.

(12) Mazumder, V.; Chi, M.; More, K. L.; Sun, S. Core/Shell Pd/FePt Nanoparticles as an Active and Durable Catalyst for the Oxygen Reduction Reaction. J. Am. Chem. Soc. 2010, 132 (23), 7848–7849. https://doi.org/10.1021/ja1024436.

(13) Stamenkovic, V. R.; Fowler, B.; Mun, B. S.; Wang, G.; Ross, P. N.; Lucas, C. A.; Marković, N. M. Improved Oxygen Reduction Activity on Pt3Ni(111) via Increased Surface Site Availability. Science 2007, 315 (5811), 493–497. https://doi.org/10.1126/science.1135941.

(14) Synthesis and Characterization of 9 nm Pt–Ni Octahedra with a Record High Activity of 3.3 A/mgPt for the Oxygen Reduction Reaction| Nano Letters https://pubs.acs.org/doi/10.1021/nl401881z (accessed Oct 31, 2019).

(15) Li, M.; Zhao, Z.; Cheng, T.; Fortunelli, A.; Chen, C.-Y.; Yu, R.; Zhang, Q.; Gu, L.; Merinov, B. V.; Lin, Z.; et al. Ultrafine Jagged Platinum Nanowires Enable Ultrahigh Mass Activity for the Oxygen Reduction Reaction. *Science* 2016, *354* (6318), 1414–1419. https://doi.org/10.1126/science.aaf9050.

(16) Cheng, T.; Huang, Y.; Xiao, H.; Goddard, W. A. Predicted Structures of the Active Sites Responsible for the Improved Reduction of Carbon Dioxide by Gold Nanoparticles. *The Journal of Physical Chemistry Letters* 2017, *8* (14), 3317–3320. https://doi.org/10.1021/acs.jpclett.7b01335.

(17) Cheng, T.; Xiao, H.; Goddard, W. A. Nature of the Active Sites for CO Reduction on Copper Nanoparticles; Suggestions for Optimizing Performance. *J. Am. Chem. Soc.* 2017, *139* (34), 11642–11645. https://doi.org/10.1021/jacs.7b03300.

(18) Huang, Y.; Chen, Y.; Cheng, T.; Wang, L.-W.; Goddard, W. A. Identification of the Selective Sites for Electrochemical Reduction of CO to C $_{2+}$ Products on Copper Nanoparticles by Combining Reactive Force Fields, Density Functional Theory, and Machine Learning. *ACS Energy Letters* 2018, 2983–2988. https://doi.org/10.1021/acsenergylett.8b01933.

(19) Carrasquilla, J.; Melko, R. G. Machine Learning Phases of Matter. *Nature Physics* 2017, *13* (5), 431–434. https://doi.org/10.1038/nphys4035.

(20) Butler, K. T.; Davies, D. W.; Cartwright, H.; Isayev, O.; Walsh, A. Machine Learning for Molecular and Materials Science. *Nature* 2018, *559* (7715), 547–555. https://doi.org/10.1038/s41586-018-0337-2.

(21) Huang, Y.; Chen, Y.; Cheng, T.; Wang, L.-W.; Goddard, W. A. Identification of the Selective Sites for Electrochemical Reduction of CO to C $_{2+}$ Products on Copper Nanoparticles by Combining Reactive Force Fields, Density Functional Theory, and Machine Learning. ACS Energy Letters 2018, 2983–2988.

(22) Chen, Y.; Huang, Y.; Cheng, T.; Goddard, W. A. Identifying Active Sites for CO2 Reduction on Dealloyed Gold Surfaces by Combining Machine Learning with Multiscale Simulations. *J. Am. Chem. Soc.* 2019, *141* (29), 11651–11657.

(23) Chen, Y.; Cheng, T.; Goddard III, W. A. Atomistic Explanation of the Dramatically Improved Oxygen Reduction Reaction of Jagged Platinum Nanowires, 50 Times Better than Pt. *J. Am. Chem. Soc.* 2020, *142* (19), 8625–8632.

Chapter II

ATOMISTIC EXPLANATION OF THE DRAMATICALLY IMPROVED OXYGEN REDUCTION REACTION OF JAGGED PLATINUM NANOWIRES, 50 TIMES BETTER THAN PT

ABSTRACT

Pt is the best catalyst for the oxygen reduction reactions (ORR) but it is far too slow. Huang and coworkers showed that dealloying 5 nm Ni_7Pt_3 Nanowires (NW) led to 2 nm pure Pt Jagged NW (J-PtNW) with ORR 50 times faster than Pt/C. They suggested that the under-coordinated surface Pt atoms, mechanical strain, and high electrochemically active surface area (ECSA) are the main contributors. We report here multiscale atomic simulations that further explain this remarkably accelerated ORR activity from the atomistic perspective. We used the ReaxFF reactive force field to convert the 5 nm Ni_7Pt_3 NW to the jagged 2 nm NW. We applied Quantum Mechanics to find that 14.4% of the surface sites are barrier-less for $O_{ads} + H_2O_{ads} \rightarrow 2OH_{ads}$, the rate determining step (RDS). The reason is that concave nature of many surface sites pushes the OH bond of the $H2O_{ads}$ close to the O_{ads}, leading to a dramatically reduced barrier. We used this observation to predict the performance improvement of the J-PtNW relative to Pt (111). Assuming every surface site reacts independently with this predicted rate leads to a 212-fold enhancement at 298.15K, compared to 50 times experimental. The atomic structures of the active sites provide insights for designing high-performance electrocatalysts for ORR.

2.1 INTRODUCTION

Proton Exchange Membrane Fuel Cells (PEMFCs) provide the most promising means for addressing the global renewable energy supply and clean environment[1–3]. Currently the main impediment for large-scale PEMFCs commercialization is the sluggish oxygen reduction reactions (ORR), which dramatically increases catalyst costs. Extensive efforts are underway to develop electrocatalysts for ORR with much higher performance and lower cost[4–6]. Pt-alloy nanomaterials show enhanced performance[7–12], especially PtNi alloys[13–17]. In particular, very dramatically improved performance has been observed in dealloyed Pt

nanomaterials[18–22]. Thus Debe and coworkers showed that Ni_7Pt_3 nanoparticles (NP) led to significantly improved ORR activity, 4 times higher than pure Pt and 60% higher than for the NSTF standard $Pt_{68}Co_{29}Mn_3$ alloy[23–26]. However, no Ni was observed in the XPS, suggesting the NP was a dealloyed Pt NP. Fortunelli and Goddard (FG) used the ReaxFF reactive force field[27] to predict the structure of the dealloyed Debe NP and found that starting with 70% Ni led to a porous Pt with significant interior area exposed to the surface. FG found that the O_{ads} hydration reaction,

$$O_{ads} + H_2O_{ads} \rightarrow 2OH_{ads} \quad (1)$$
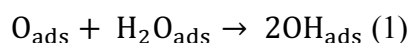
which is the rate determining step (RDS) on Pt (111), is dramatically accelerated on this porous NP compared to Pt (111)[28].

Later, Huang, Duan, Goddard, and co-workers[29] showed that dealloying 5 nm Ni_7Pt_3 Nanowires (NW) led to 2 nm Pt Jagged NW (J-PtNW) with 50 times faster ORR than current state-of-the-art Pt/C, but they found that all Ni was extracted! Building this dramatically improved performance into commercial fuel cells would be a game-changer, dramatically decreasing the costs of hydrogen fuel cells needed to extract the power from fuel generated and stored at solar power plants to provide practical transportation without CO2 emissions.

Although several factors, such as under-coordinated surface Pt atoms, mechanical strain, and high electrochemically active surface area (ECSA), have been suggested to contribute to this remarkably accelerated ORR activity[29], there was no atomistic explanation about which sites on this very complex surface are responsible, leaving no roadmap to build this activity into practical electrodes.

To address this conundrum, we report here multiscale simulations to explain the dramatically improved performance and to characterize the atomic features of active sites responsible. Starting with the J-PtNW synthesized computationally using ReaxFF reactive force field, we selected randomly 500 of the more than 10,000 surface sites and carried out Quantum Mechanics (QM) Calculations on clusters within 8 Å of the surface site. Here we considered reaction (1), the RDS on Pt (111). We observed a strong correlation between OO Distance (the distance between O_{ads} and the O of $H2O_{ads}$) and the free energy barrier for reaction (1). Indeed 14.4% of the 500 surface sites sampled are barrier-less of reaction (1) at room temperature, compared to 0.29 eV for Pt (111) and hence increased reaction rate. We then

modeled the reaction rates of all surface sites based on their OO Distances and estimated the performance of the whole J-PtNW.

We found two distinct geometric patterns,

o   Triangles where the H2O binds to one vertex and O to the other two;

o   Concave-Up Rhombi where O binds to one edge and the H2O to one of the remaining two vertices.

The atomic structure of these active sites provides insights on designing high-performance electrocatalysts for ORR.

2. 2 RESULTS AND DISCUSSION

2.2.1 Structure Analysis and Surface Extraction of J-PtNW

Starting with the J-PtNW synthesized using ReaxFF reactive molecular dynamics (RMD) as in the previous work[29], we identified all surface atoms using the surface vector based methodology. The detailed description of structure synthesis and surface vector based methodology are listed in *A1 and A2 of Supporting Information.* The nanowire has 6926 Pt atoms, with 3881 on the surface (surface ratio: 56.0%). We partitioned these surface sites into coordination groups based on the number of first-neighbor atoms, using a first-neighbor cut-off at 3.50 Å based on the radial distribution functions in Figure A-2(a) of Supporting Information. The J-PtNW showed broader peaks with the first peak located close to the first peak of Pt single crystal, as expected. We observed many under-coordinated and over-coordinated sites both on the surface and in the bulk. The surface site distribution versus coordination is shown in Figure A-2(b) of Supporting Information. For better visualization, we plotted the surface in Figure A-3 of Supporting Information*,* with all surface sites colored by their coordination (ranging from 3 to 12). This structural analysis showed that the J-PtNW have an extremely disordered and irregular surface, making it challenging to characterize experimentally and computationally.

2.2.2 Bridge Nanocluster Model

To study the relationship between the structure and catalytic activity, we need to define a physical descriptor that might correlate with the performance (reaction rate). Based on the reaction mechanism revealed by earlier work[30–32], we focused on the O_{ads} hydration,

reaction (1).

Our full solvent QM Metadynamics showed that this step is the rate determining step (RDS) for applied potentials of U ≤ 0.9 V reversible hydrogen electrode (RHE)[30,33,34]. Since this reaction requires two sites for water adsorption and oxygen adsorption, instead of the single site nanocluster model used in our previous machine learning studies for Copper[35,36] and Gold[37,38], we developed a new bridge nanocluster model in this work. As shown in Figure 2-1, we generated the bridge nanocluster by cutting two spheres of size R around the Pt atom for water adsorption (Pt-1) and the Pt atom for oxygen adsorption (Pt-2). Then, we merged these two spheres to a single nanocluster. The choice of R was based on the benchmark calculations in *A3 of Supporting Information*. We found that 8.0 Å is already sufficient to provide 0.02 eV accuracy in the adsorption energy for both reactants and products. Therefore, we consider that 8.0 Å provides the best balance between accuracy and efficiency and used this cut-off throughout this work.

2.2.3 OO Distance as Physical Descriptor

We carried out DFT calculations[39] for the O_{ads} hydration, reaction (1), using the bridge nanocluster model defined in *Section 2.2.2*. We chose the free energy barrier (G_a) of reaction (1) as the physical descriptor to evaluate the performance of each bridge nanocluster. We expect that sites with lower G_a should have better ORR performance. With such a disordered and irregular surface, we might have to sample all bridging surface sites to be sure to properly represent the activity of the full NW. DFT calculations on the transition state reaction barrier for the whole J-PtNW, would require far too much computational resources[40]. Instead we defined a physical descriptor, OO Distance (d-OO), the distance between the O of H_2O_{ads} and the O_{ads}. Then we showed that d-OO is highly correlated with the free energy barrier (G_a), $G_a = G_{TS} - G_{Reactants}$, but much faster to calculate.

To obtain d-OO, we need only to optimize the structure of the reactants, H2O and O. We show in Figure A-7 of Supporting Information three examples illustrating the correlation between d-OO and G_a at room temperature. By comparing to our reference case Pt (111), which has $G_a = 0.29$ eV and d-OO = 3.36 Å, we observed that shorter d-OO leads to much lower G_a (d-OO at 2.60 Å leads to $G_a = 0.00$ eV) and larger d-OO leads to higher G_a (d-OO at 3.98 Å leads to $G_a = 0.35$ eV). In addition, thermodynamic reaction energy ($\Delta G =$

$G_{Products} - G_{Reactants}$), doesn't correlate with G_a, as expected. Therefore, we used d-OO as the physical descriptor to evaluate performance of each bridge nanocluster. All our calculations include solvation effect using the VASPsol implicit solvation model[41]. As shown in Figure A-5 and A-6 in Supporting Information, solvation affects d-OO in a non-negligible manner. The free energy barriers (G_a) at room temperature (298.15 K) are obtained by adding to the DFT electronic energy (E), the zero-point energy (ZPE), enthalpy and entropy contribution from vibrational modes of surface species. More computational details of d-OO and G_a are listed in *A4 and A5 of Supporting Information.*
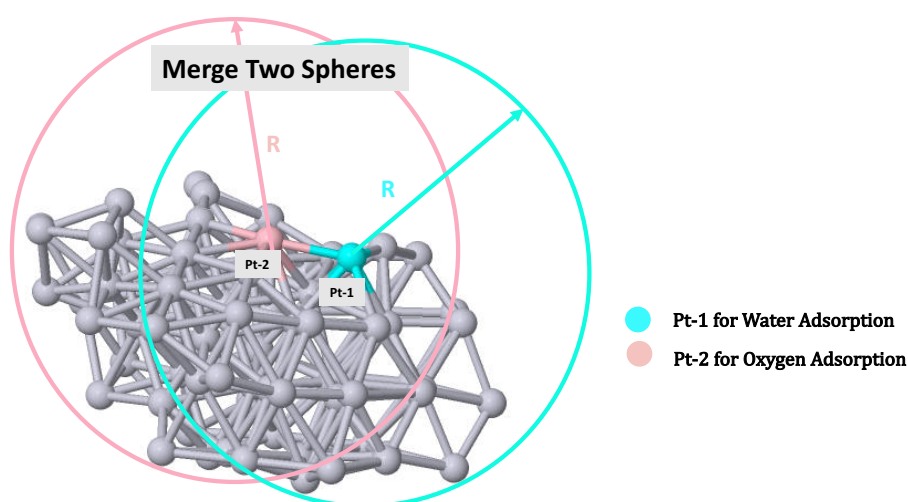
Figure 2-1. Bridge Nanocluster Model. We first cut two spheres of size R around Pt-1 (cyan atom) and Pt-2 (pink tom), where Pt-1 is specifically for water adsorption and Pt-2 is for oxygen adsorption. These two spheres are then merged to a single nanocluster. R here is optimized to 8 Å. This bridge nanocluster will later be used for DFT calculations.

2.2.4 Data Sampling for DFT calculations (d-OO)

To generate all possible bridge pairs from 3881 surface Pt atoms of the J-PtNW, we first examined Pt-1 for water adsorption of all surface Pt atoms. Then, for each Pt-1, we examined its first-neighbors on the surface to select Pt-2 for binding an O atom. This defines a bridge pair. The definition of Pt-1 and Pt-2 are the same as in Figure 2-1. Then, we cut the corresponding bridge nanoclusters from the NW. This generates the same nanocluster twice with Pt-1 and Pt-2 swapping the labels, but we consider them as different structures since Pt-

1 is specifically for water adsorption and Pt-2 is specifically for oxygen adsorption. The two Pts are not identical when binding adsorbates. An example of two nanoclusters of same coordinates but defined as different structures is shown in Figure A-8 of Supporting Information.

In this way, we generated 21,057 bridge pairs. Since H2O binds weakly to high-coordination sites, we expect that they would be inactive for ORR. To test this, we selected randomly 50 sites for which Pt-1 has a coordination larger than 9 and calculated water adsorption. We found water desorbed from all 50 sites. Therefore, we discarded the high-coordination bridge pairs (coordination of Pt-1 > 9), which leaves 12,400 bridge nanoclusters for further sampling. This procedure is Illustrated schematically in Figure 2-2.
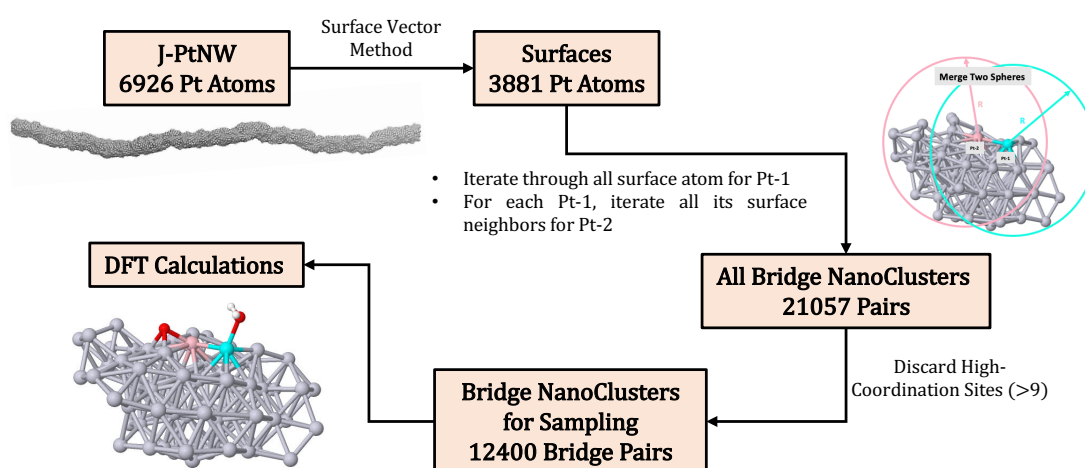
Figure 2-2. Generating All Bridge Pairs for Data Sampling. Starting from the J-PtNW with 6926 Pt atoms, we identified 3881 surface atoms using surface vector methodology. Then, we iterated first over the whole surface for Pt-1 and for each Pt-1 we iterated over its surface neighbors for Pt-2. In this way, we generated a total number of 21,057 bridge pairs. We showed that sites with coordination larger than 9, cannot adsorb water. Discarding these bridge pairs with coordination of Pt-1 larger than 9 leaves 12,400 bridge pairs for data sampling.

We then randomly sampled 500 bridge nanoclusters from these 12,400 pairs for DFT calculations. For each nanocluster, we put water on Pt-1 and oxygen on Pt-2, and then

optimized the structure to find the best conformation for the adsorbates. Solvation effect are included here using the VASPsol implicit solvation model. Additional DFT calculation details, including all benchmark calculations are listed in Section A.4, Table A-1~A-3 *and* Figure A-5~A-6 of Supporting Information. The sampled bridge centers are plotted back on the NW in Figure A-9 of Supporting Information. The bridge centers are distributed throughout the whole nanowire, indicating our sample is a good representation of the whole J-PtNW.

The distribution of d-OO among 500 nanoclusters is shown in Figure 2-3. We see that d-OO ranges from 2.50 Å to 6.01 Å. However, 35.2% of the sites have d-OO distance shorter than the d-OO (3.36 Å) for Pt (111). We expect these sites to have much lower free energy barrier for O_{ads} hydration and hence to contribute significantly to the dramatically improved performance of J-PtNW at ORR. To help provide a better understanding of how the geometry of different sites affects d-OO and free energy barrier, several representative structures with different d-OO are also shown at the bottom of Figure 2-3.
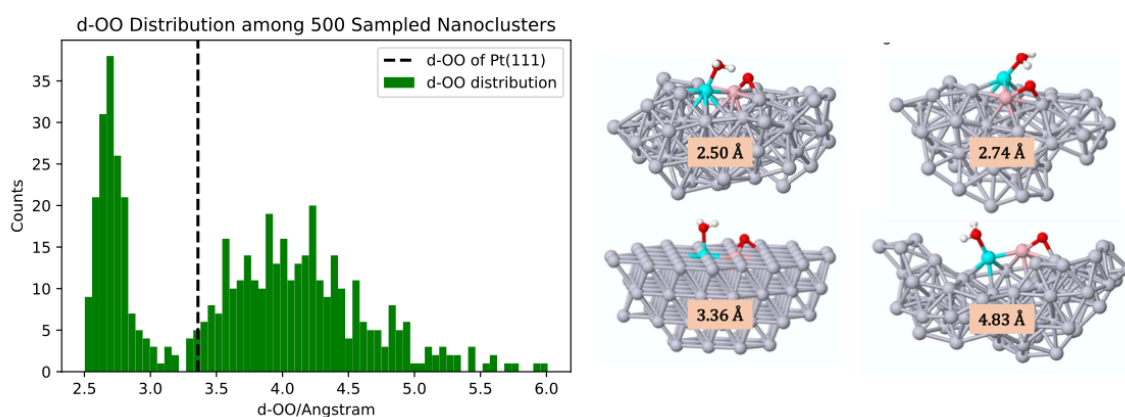
Figure 2-3. d-OO Distribution among 500 Sampled Bridge Nanoclusters. Our sample showed a broad range of d-OO, from 2.50 Å to 6.01 Å. The d-OO of Pt (111) is marked in the plot as the dashed line. We observed 35.2% of the sites lying to the left to Pt (111), showing much shorter d-OO. We expect these sites to have much lower energy barrier for O_{ads} hydration, thus leading to higher ORR performance. Four representative structures with different d-OO are attached here for understanding the correlation between structure and catalytic activities.

2.2.5 Correlation of d-OO with Catalytic Activity

To further understand the correlation between d-OO and the catalytic activity of each bridge site, we selected 18 structures with various d-OO and calculated the transition state and free energy barriers. The structures were selected randomly and independently but in such a way to ensure that we covered a broad range of d-OO. For each structure, we carried out the transition state search using the climbing image nudged elastic band (NEB) method with implicit solvation using VASPsol tool. The free energy barriers (G_a) for the O_{ads} hydration at room temperature (298.15 K) are then obtained by adding to the DFT electronic energy (E), the zero-point energy (ZPE), enthalpy and entropy contribution from vibrational modes of surface species. The data for the 18 structures, including d-OO and free energy barriers (G_a) at room temperature are listed in Table 2-1. More computation details toward the transition state search are included in A5 of Supporting Information.

Table 2-1. Correlation Between d-OO and Free Energy Barrier (G_a) at Room temperature 298.15K

d-OO/ Å	$G_a(298.15K, eV)$	d-OO/ Å	$G_a(298.15K, eV)$	d-OO/ Å	$G_a(298.15K, eV)$
2.50	0.00	2.76	0.01	3.50	0.20
2.56	0.00	2.80	0.06	3.57	0.19
2.60	0.00	2.93	0.12	3.70	0.14
2.64	0.00	2.99	0.10	3.75	0.40
2.68	0.00	3.12	0.16	3.98	0.35
2.74	0.01	<u>3.36</u>	<u>0.29</u>	4.22	0.28

We observed a strong correlation between d-OO and G_a, as shown in Table 2-1. The sites with small d-OO shows low free energy barriers, especially with d-OO <= 2.68 Å, O_{ads} hydration step becomes barrier-less. And with larger d-OO, G_a generally becomes higher, but in a non-linear manner. Pt (111) shows d-OO at 3.36 Å and G_a at 0.29 eV, underlined in Table 2-1. To better correlate d-OO with catalytic activity, we used transition state theory (TST) to estimate the reaction rate as $k = (k_B T/h) \, exp(- G_a/k_B T)$. The reaction rates are plotted versus d-OO of 18 structures in Figure 2-4. Here, we used the sigmoid function to fit the k(d-OO) curve at room temperature. The fitted curve is also shown in Figure 2-4 with R^2 at 0.9894.

Therefore, we found that a large portion of sites on the J-PtNW surface exhibit dramatically improved performance toward O_{ads} hydration, the RDS. We claim that this is the main

contributor to the dramatically improved ORR performance. In addition, we showed that d-OO is a good descriptor for evaluating catalytic activity of any specific bridge pair.
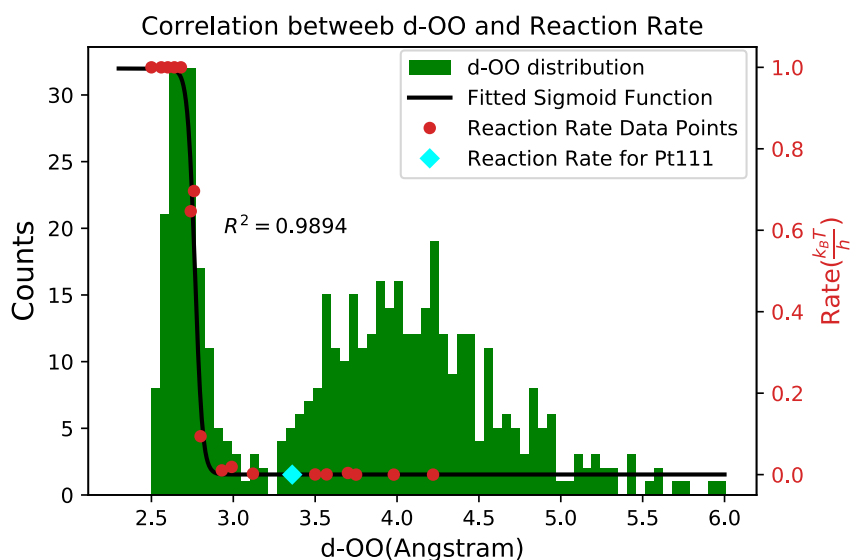
Figure 2-4. Correlation Between d-OO and Reaction Rate. we used transition state theory (TST) to estimate the reaction rate as $k = (k_BT/h)\,exp(-G_a/k_BT)$ of 18 selected structures listed in Table 2-1. The reaction rates are plotted in the unit of (k_BT/h) versus d-OO. We then used the sigmoid function to fit the k(d-OO) curve at room temperature, $k = L/(1 + exp(A \times (d\text{-}OO - x_0))) + b$. The parameters at ($A = 47.1056$, $x_0 = 2.7659$, $b = 0.0003$, $L = 0.9968$) gives the R^2=0.9894.

2.2.6 Performance Prediction of the Whole J-PtNW

Since our dataset is sampled randomly and independently, we consider it to be representative of the whole J-PtNW surface. Thus, we estimated the performance of the whole nanowire by mapping the statistics of our sample back to the full NW. The J-PtNW has 6926 Pt atoms with 3881 surface atoms, which leads to 21,057 bridge pairs. Among these 21,057 pairs, 8657 are high-coordination involved pairs, which we assume are inactive. The remaining 12,400 pairs should have the similar d-OO distribution as the 500 samples.

To estimate the performance improvement at different temperatures, we first calculated the free energy barriers at different temperature, and refit the sigmoid functions. In other words, k(d-OO) is dependent of T. Three examples of fitting k(d-OO) at different temperatures are shown in Figure A-10 of Supporting Information.

$$k(d\text{-}OO|T) = L / (1 + exp(A \times (d\text{-}OO - x_0))) + b \ (2)$$

Then, the total performance of J-PtNW is calculated by mapping the sample statistic to total 12400 pairs:

$$p_{NW}(T) = \left(\sum_{i=0}^{N_s} k(d\text{-}OO_i|T)\right) \times \left(\frac{N_t - N_h}{N_S}\right) (3)$$

Where:

1) the N_t is the total number of bridge pairs, N_h is the high coordination bridge pairs and N_s is the sampled bridge pairs. Here, $N_t = 21057, N_h = 8657, N_s = 500$;

2) $k(d\text{-}OO|T)$ is the fitted sigmoid function at temperature T.

The experiments showed that the J-PtNW performance is 50 times better than Pt/C at room temperature at mass activity. We considered that Pt/C is Pt (111) with 6926 surface Pt atoms, since the J-PtNW has 6926 Pt atoms in total with 3881 on the surface. In this way, we ensure the performance we are comparing is mass activity. This leads to 41,574 pairs. Therefore, the performance of Pt (111) can be estimated as following:

$$p_{pt(111)}(T) = k(d\text{-}OO_0|T) \times N_0 \ (4)$$

where N_0 = 41,574 is the total number of bridge pairs, and $k(d\text{-}OO_0|T)$ is the reaction rate for Pt (111) at temperature.

We then define the improvement of the performance as PI(T), which is dependent of temperature and calculated by formula (5):

$$PI(T) = p_{NW}(T)/p_{pt(111)}(T) \ (5)$$

Figure 2-5 shows the temperature dependence of the estimated performance improvement. At room temperature, our model leads to PI = 212.21 for the J-PtNW. This is a factor of 4 higher than the experimental PI=50[29]. We consider that this agreement validates our explanation. This model, allows us to predict the performance improvement of J-PtNW at increased temperatures. For example, low-temperature PEMFCs use a water-based acidic polymer membrane as the electrolyte, with platinum-based electrodes. Thus, the upper temperature limit is around 80 °C. Our model, estimates PI = 19.70 at 353.15 K (marked as red diamond in Figure 2-5). Correcting by the same factor 4, we predict the performance of

J-PtNW should be around 5 time better than Pt (111) at 80 ˚C. This may provide guidance in choosing optimal conditions for the real J-PtNW.
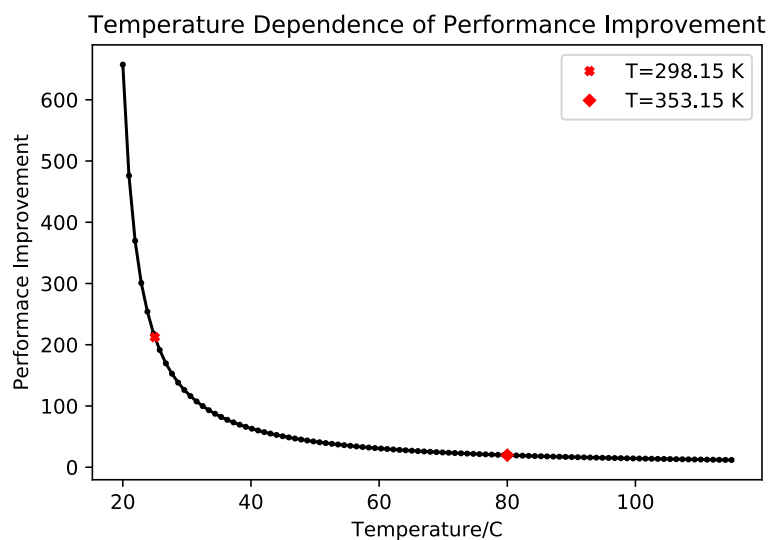
Figure 2-5. Temperature Dependence of Performance Improvement. With increasing temperature, the performance improvement decreases. The PI at 298.15 K is marked in red, is PI=212.21 is 4 times larger than experimental = 50. The temperature limit of low-temperature PEMFCs is also marked as red diamond, PI=19.70 at 353.15 K.

2.2.7 Active Sites Identification

To reveal the important features of the active sites and to provide insights for designing high-performance electrocatalysts, we characterized the structures of barrier-less sites (d-OO <= 2.68 Å). They account for 72 out of the 500 bridge nanoclusters sampled. Among these 72 structures, many share similar geometric features. Thus, we further partitioned them into three subgroups:

I1) Concave-up Rhombus (30.8%);

I2) Triangle (43.6%);

I3) Others (25.6%).

Figure 2-6, shows one representative structure from each group. We consider that the Triangle group and Concave-Up Rhombus group play an important role in the dramatically

improved performance. We summarized their geometry features and analyzed their statistics among the 500 structures in the following session.
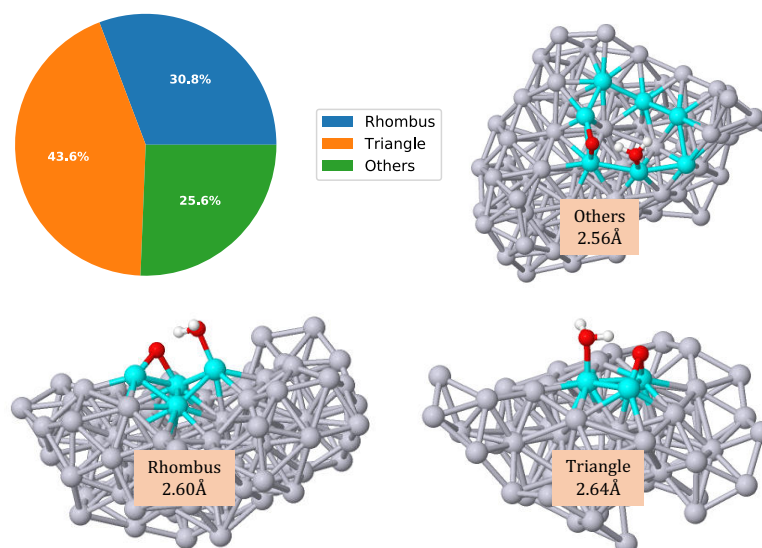
Figure 2-6. Identification Results of Barrier-Less Sites (d-OO <= 2.68 Å). Among the 72 barrier-less sites, 30.8% of them are in the Concave-up Rhombus group and 43.6% of them are in the Triangle group. One representative structure of each group is attached with their d-OO marked as well.

2.2.7.1 Triangle Group Statistics

As shown in Figure 2-6, Triangle group I2 is an important part of barrier-less sites (43.6%). We define a structure as a triangle structure if its three Pts, the one binding water, and the other two binding O, form a closed ring, marked as cyan in Figure 2-6. Based on this definition, we picked out all triangle structures from the 500 sampled bridge nanoclusters and plotted their distribution toward d-OO in Figure 2-7. There are 143 triangles in sample with the main peak located at ~2.75 Å. Although several triangles showed large d-OO (one representative structure of a bad triangle is shown in Figure 2-7), we see that major percentage the triangles lead to dramatically improved performance of the J-PtNW. Thus, a synthetic strategy might focus on generating triangle structures. Additional Triangle structures with various d-OO are shown in Figure A-11 in Supporting Information.
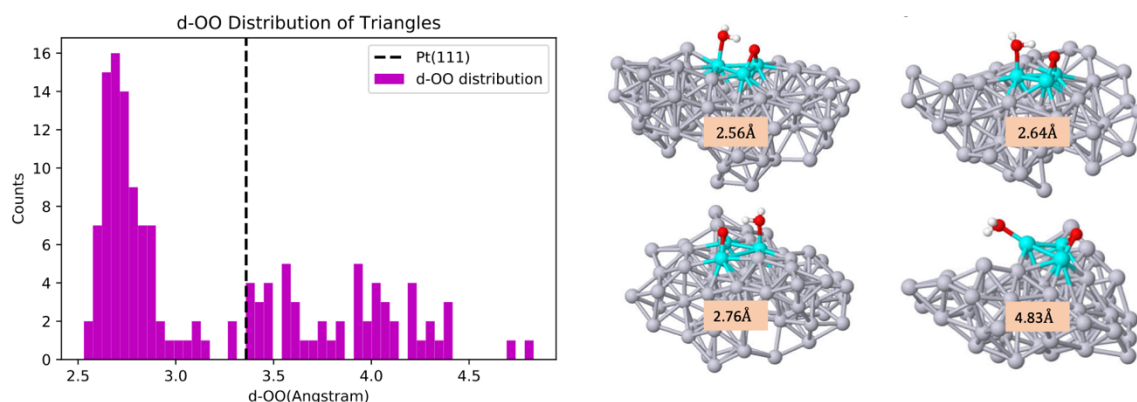
Figure 2-7. Statistics of Triangle Group among 143 out of 500 Sampled Bridge Nanoclusters. (a) There are 143 Triangles in total, and 87 of them show shorter d-OO than Pt (111). A small fraction of the triangles showed large d-OO, but the main peak is located way left from Pt (111), (dashed line in the plot). (b) Four representative structures of different d-OO. More structures are included in Figure A11 in Supporting Information.

2.2.7.2 Concave-Up Rhombus Group Statistics

We then examined all Concave-up Rhombus structures among the 500 sampled bridge nanoclusters. The Concave-Up Rhombus is defined as following: the three Pts, One Pt binding H2O, and the other two Pts binding O, cannot form a closed ring. Instead another surface Pt is required to close the ring, forming a concave-up rhombus. As shown in Figure 2-8, we then define the dihedral angle of a rhombus as the dihedral angle between two surfaces defined by (Pt1, Pt2, Pt4) and (Pt2, Pt3, Pt4). Larger the dihedral angle is, the more concave-up the rhombus is. There are a total number of 234 rhombi out of 500 with different dihedral angles. We plotted the correlation between the dihedral angle and d-OO in Figure 2-8(a), and we found the Concave-Up Rhombus with dihedral angle larger than 30° mostly show short d-OO.

Thus, if we cut off the dihedral angle to 30°, the population of active Concave-Up Rhombic becomes 57 out of 500. Therefore, we define our active Concave-Up Rhombic as those with dihedral angle > 30˚. These 57 active Concave-Up Rhombi are plotted in the Figure 2-8(b), along with several representative structures shown in Figure 2-8(c). More structures with different d-OO distances are available in Figure A-12 in Supporting Information.
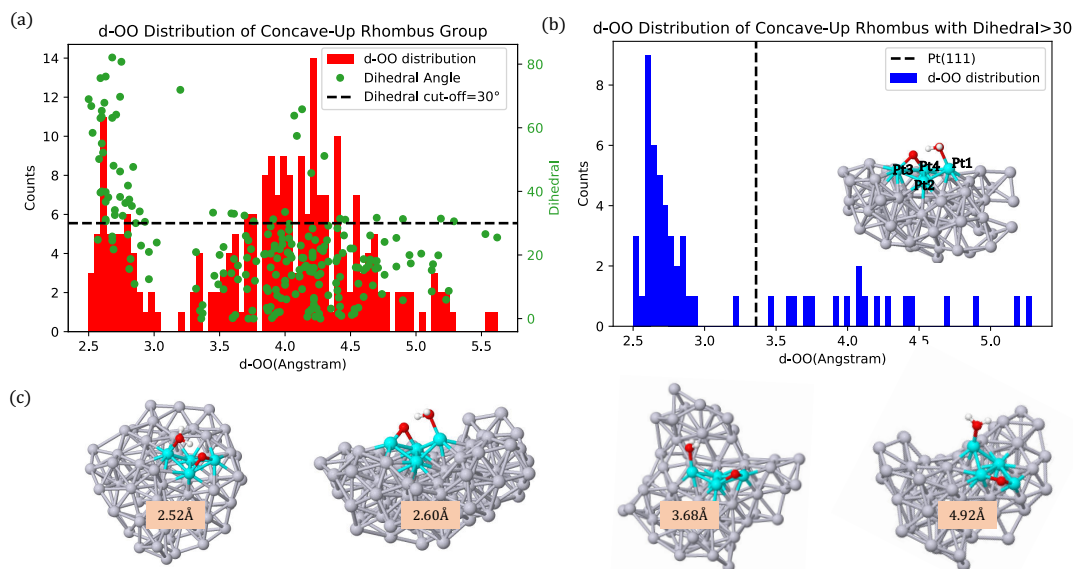
Figure 2-8. Statistics of Concave-Up Rhombus among 234 out of 500 Sampled Bridge Nanoclusters. (a) The correlation between dihedral angle and d-OO is shown in plot. Here dihedral angle is defined as the angle between two surfaces defined by (Pt1, Pt2, Pt4) and (Pt2, Pt3, Pt4). As we could see, the rhombus with dihedral angle larger than 30° mostly show short d-OO; (b) Statistics of Concave-up Rhombus with Dihedral Angle>30°. Most of structures in this group show the small d-OO with the main peak located at 2.6 Å; (c) Four representative structures with different d-OO are attached here and more structures are available in Figure A-12 in Supporting Information.

2.2.8 Comparison with Previous Literature

The above discussion, shows the atomistic explanation of the dramatically improved performance. Thus, the jagged NW has many sites with a concave nature that pushes the OH bond of the $H2O_{ads}$ toward the O_{ads}, leading to a dramatically reduced energy barrier for O_{ads} hydration. Earlier, Huang and coworkers suggested that mechanical strain, high ECSA, and under-coordinated surface Pt atoms may affect this remarkably accelerated ORR activity[29]. Consistent with these previous literature results, our analysis also finds numerous under-coordinated Pt surface atoms and a high 56.0% surface atom ratio (Section 2.2.1), which will affect the ECSA.

To correlate the mechanical strain with catalytic activity, we plotted the E_a versus the strain of the selected 18 structures from *Section 2.2.5*. Here we used the average Pt-Pt bond length

around the adsorption sites to represent the local strain. As shown in Figure A-13 of Supporting Information, there is a linear correlation between the catalytic activity and strain. In general, the sites with compressive strains show lower energy barriers and sites with tensile strains show higher energy barriers. The correlation is weak with small R^2 at 0.46, but we agree that mechanical strain plays a role in reduced energy barrier of O_{ads} hydration. Our work, with overall agreement with experiment in NW structure characterization and performance prediction, explains the dramatically improved ORR of J-PtNW from a very different atomistic perspective.

2.3 CONCLUSION

Starting from the J-PtNW synthesized using the ReaxFF reactive force field, we developed the bridge nanocluster model for DFT calculations. Using sites randomly selected from the surface, we observed a strong correlation between d-OO and the free energy barrier G_a of the RDS, O_{ads} hydration. This dramatically reduced the computational cost but accurately described the performance of each bridge pair. We found 14.4% of the sampled surface sites are barrier-less for the RDS. Identification of these active sites led to two groups sharing similar geometrical patterns, the Triangle group and Concave-up Rhombus. Using the model developed above, we could predict the performance improvement of the whole J-PtNW. We report the atomistic structure of the active sites, which provide some insights in designing high-performance electrocatalysts for ORR.

BIBLIOGRAPHY

(1) Peighambardoust, S. J.; Rowshanzamir, S.; Amjadi, M. Review of the Proton Exchange Membranes for Fuel Cell Applications. International Journal of Hydrogen Energy 2010, 35 (17), 9349–9384. https://doi.org/10.1016/j.ijhydene.2010.05.017.

(2) Steele, B. C. H.; Heinzel, A. Materials for Fuel-Cell Technologies. Nature 2001, 414 (6861), 345–352. https://doi.org/10.1038/35104620.

(3) Wang, S.; Jiang, S. P. Prospects of Fuel Cell Technologies. Natl Sci Rev 2017, 4 (2), 163–166. https://doi.org/10.1093/nsr/nww099.

(4) Shao, M.; Chang, Q.; Dodelet, J.-P.; Chenitz, R. Recent Advances in Electrocatalysts for Oxygen Reduction Reaction. Chem. Rev. 2016, 116 (6), 3594–3657. https://doi.org/10.1021/acs.chemrev.5b00462.

(5) Sui, S.; Wang, X.; Zhou, X.; Su, Y.; Riffat, S.; Liu, C. A Comprehensive Review of Pt Electrocatalysts for the Oxygen Reduction Reaction: Nanostructure, Activity, Mechanism and Carbon Support in PEM Fuel Cells. J. Mater. Chem. A 2017, 5 (5), 1808–1825. https://doi.org/10.1039/C6TA08580F.

(6) He, Q.; Cairns, E. J. Review—Recent Progress in Electrocatalysts for Oxygen Reduction Suitable for Alkaline Anion Exchange Membrane Fuel Cells. J. Electrochem. Soc. 2015, 162 (14), F1504–F1539. https://doi.org/10.1149/2.0551514jes.

(7) Huang, X.; Zhao, Z.; Chen, Y.; Zhu, E.; Li, M.; Duan, X.; Huang, Y. A Rational Design of Carbon-Supported Dispersive Pt-Based Octahedra as Efficient Oxygen Reduction Reaction Catalysts. Energy Environ. Sci. 2014, 7 (9), 2957–2962. https://doi.org/10.1039/C4EE01082E.

(8) Peng, Z.; Yang, H. Designer Platinum Nanoparticles: Control of Shape, Composition in Alloy, Nanostructure and Electrocatalytic Property. Nano Today 2009, 4 (2), 143–164. https://doi.org/10.1016/j.nantod.2008.10.010.

(9) Wu, J.; Yang, H. Platinum-Based Oxygen Reduction Electrocatalysts. Acc. Chem. Res. 2013, 46 (8), 1848–1857. https://doi.org/10.1021/ar300359w.

(10) Porter, N. S.; Wu, H.; Quan, Z.; Fang, J. Shape-Control and Electrocatalytic Activity-Enhancement of Pt-Based Bimetallic Nanocrystals. Acc. Chem. Res. 2013, 46 (8), 1867–1877. https://doi.org/10.1021/ar3002238.

(11) Wang, D.; Xin, H. L.; Hovden, R.; Wang, H.; Yu, Y.; Muller, D. A.; DiSalvo, F. J.; Abruña, H. D. Structurally Ordered Intermetallic Platinum-Cobalt Core-Shell Nanoparticles with Enhanced Activity and Stability as Oxygen Reduction Electrocatalysts. Nat Mater 2013, 12 (1), 81–87. https://doi.org/10.1038/nmat3458.

(12) Mazumder, V.; Chi, M.; More, K. L.; Sun, S. Core/Shell Pd/FePt Nanoparticles as an Active and Durable Catalyst for the Oxygen Reduction Reaction. J. Am. Chem. Soc. 2010, 132 (23), 7848–7849. https://doi.org/10.1021/ja1024436.

(13) Stamenkovic, V. R.; Fowler, B.; Mun, B. S.; Wang, G.; Ross, P. N.; Lucas, C. A.; Marković, N. M. Improved Oxygen Reduction Activity on Pt3Ni(111) via Increased Surface Site Availability. Science 2007, 315 (5811), 493–497. https://doi.org/10.1126/science.1135941.

(14) Choi, S.-I.; Xie, S.; Shao, M.; Odell, J. H.; Lu, N.; Peng, H.-C.; Protsailo, L.; Guerrero, S.; Park, J.; Xia, X.; Wang, J.; Kim, M. J.; Xia, Y. Synthesis and Characterization of 9 Nm Pt–Ni Octahedra with a Record High Activity of 3.3 A/MgPt for the Oxygen Reduction Reaction. Nano Lett. 2013, 13 (7), 3420–3425. https://doi.org/10.1021/nl401881z.

(15) Huang, X.; Zhao, Z.; Cao, L.; Chen, Y.; Zhu, E.; Lin, Z.; Li, M.; Yan, A.; Zettl, A.; Wang, Y. M.; Duan, X.; Mueller, T.; Huang, Y. High-Performance Transition Metal–Doped Pt3Ni Octahedra for Oxygen Reduction Reaction. Science 2015, 348 (6240), 1230–1234. https://doi.org/10.1126/science.aaa8765.

(16) Wang, Y.-J.; Zhao, N.; Fang, B.; Li, H.; Bi, X. T.; Wang, H. Carbon-Supported Pt-Based Alloy Electrocatalysts for the Oxygen Reduction Reaction in Polymer Electrolyte Membrane Fuel Cells: Particle Size, Shape, and Composition Manipulation and Their Impact to Activity. Chem. Rev. 2015, 115 (9), 3433–3467. https://doi.org/10.1021/cr500519c.

(17) Lu, Y.; Thia, L.; Fisher, A.; Jung, C.-Y.; Yi, S. C.; Wang, X. Octahedral PtNi Nanoparticles with Controlled Surface Structure and Composition for Oxygen Reduction

Reaction. Sci. China Mater. 2017, 60 (11), 1109–1120. https://doi.org/10.1007/s40843-017-9029-5.

(18) Hasché, F.; Oezaslan, M.; Strasser, P. Activity and Structure of Dealloyed PtNi3 Nanoparticle Electrocatalyst for Oxygen Reduction Reaction in PEMFC. ECS Trans. 2011, 41 (1), 1079–1088. https://doi.org/10.1149/1.3635640.

(19) Mani, P.; Srivastava, R.; Strasser, P. Dealloyed Binary PtM3 (M = Cu, Co, Ni) and Ternary PtNi3M (M = Cu, Co, Fe, Cr) Electrocatalysts for the Oxygen Reduction Reaction: Performance in Polymer Electrolyte Membrane Fuel Cells. Journal of Power Sources 2011, 196, 666. https://doi.org/10.1016/j.jpowsour.2010.07.047.

(20) Jia, Q.; Caldwell, K.; Strickland, K.; Ziegelbauer, J. M.; Liu, Z.; Yu, Z.; Ramaker, D. E.; Mukerjee, S. Improved Oxygen Reduction Activity and Durability of Dealloyed PtCox Catalysts for Proton Exchange Membrane Fuel Cells: Strain, Ligand, and Particle Size Effects. ACS Catal 2015, 5 (1), 176–186. https://doi.org/10.1021/cs501537n.

(21) Strasser, P.; Koh, S.; Yu, C. Voltammetric Surface Dealloying of Pt Bimetallic Nanoparticles: A Novel Synthetic Method Towards More Efficient ORR Electrocatalysts. ECS Trans. 2007, 11 (1), 167–180. https://doi.org/10.1149/1.2780928.

(22) Strasser, P.; Koh, S.; Anniyev, T.; Greeley, J.; More, K.; Yu, C.; Liu, Z.; Kaya, S.; Nordlund, D.; Ogasawara, H.; Toney, M. F.; Nilsson, A. Lattice-Strain Control of the Activity in Dealloyed Core-Shell Fuel Cell Catalysts. Nat Chem 2010, 2 (6), 454–460. https://doi.org/10.1038/nchem.623.

(23) Debe, M. K. Electrocatalyst Approaches and Challenges for Automotive Fuel Cells. Nature 2012, 486 (7401), 43–51. https://doi.org/10.1038/nature11115.

(24) van der Vliet, D.; Wang, C.; Debe, M.; Atanasoski, R.; Markovic, N. M.; Stamenkovic, V. R. Platinum-Alloy Nanostructured Thin Film Catalysts for the Oxygen Reduction Reaction. Electrochimica Acta 2011, 56 (24), 8695–8699. https://doi.org/10.1016/j.electacta.2011.07.063.

(25) Debe, M. K.; Steinbach, A. J.; Vernstrom, G. D.; Hendricks, S. M.; Kurkowski, M. J.; Atanasoski, R. T.; Kadera, P.; Stevens, D. A.; Sanderson, R. J.; Marvel, E.; Dahn, J. R.

Extraordinary Oxygen Reduction Activity of Pt3Ni7. J. Electrochem. Soc. 2011, 158 (8), B910–B918. https://doi.org/10.1149/1.3595748.

(26) Stevens, D. A.; Mehrotra, R.; Sanderson, R. J.; Vernstrom, G. D.; Atanasoski, R. T.; Debe, M. K.; Dahn, J. R. Dissolution of Ni from High Ni Content Pt1−xNix Alloys. J. Electrochem. Soc. 2011, 158 (8), B905–B909. https://doi.org/10.1149/1.3595747.

(27) van Duin, A. C. T.; Dasgupta, S.; Lorant, F.; Goddard, W. A. ReaxFF: A Reactive Force Field for Hydrocarbons. J. Phys. Chem. A 2001, 105 (41), 9396–9409. https://doi.org/10.1021/jp004368u.

(28) Fortunelli, A.; Goddard III, W. A.; Sementa, L.; Barcaro, G.; Negreiros, F. R.; Jaramillo-Botero, A. The Atomistic Origin of the Extraordinary Oxygen Reduction Activity of Pt3Ni7 Fuel Cell Catalysts. Chemical Science 2015, 6 (7), 3915–3925. https://doi.org/10.1039/C5SC00840A.

(29) Li, M.; Zhao, Z.; Cheng, T.; Fortunelli, A.; Chen, C.-Y.; Yu, R.; Zhang, Q.; Gu, L.; Merinov, B. V.; Lin, Z.; Zhu, E.; Yu, T.; Jia, Q.; Guo, J.; Zhang, L.; Goddard, W. A.; Huang, Y.; Duan, X. Ultrafine Jagged Platinum Nanowires Enable Ultrahigh Mass Activity for the Oxygen Reduction Reaction. Science 2016, 354 (6318), 1414–1419. https://doi.org/10.1126/science.aaf9050.

(30) Cheng, T.; Goddard, W. A.; An, Q.; Xiao, H.; Merinov, B.; Morozov, S. Mechanism and Kinetics of the Electrocatalytic Reaction Responsible for the High Cost of Hydrogen Fuel Cells. Physical Chemistry Chemical Physics 2017, 19 (4), 2666–2673. https://doi.org/10.1039/C6CP08055C.

(31) Noël, J.-M.; Latus, A.; Lagrost, C.; Volanschi, E.; Hapiot, P. Evidence for OH Radical Production during Electrocatalysis of Oxygen Reduction on Pt Surfaces: Consequences and Application. J. Am. Chem. Soc. 2012, 134 (5), 2835–2841. https://doi.org/10.1021/ja211663t.

(32) Anderson, A. B.; Albu, T. V. Catalytic Effect of Platinum on Oxygen Reduction An Ab Initio Model Including Electrode Potential Dependence. J. Electrochem. Soc. 2000, 147 (11), 4229–4238. https://doi.org/10.1149/1.1394046.

(33) Sha, Y.; Yu, T. H.; Merinov, B. V.; Shirvanian, P.; Goddard, W. A. Oxygen Hydration Mechanism for the Oxygen Reduction Reaction at Pt and Pd Fuel Cell Catalysts. J. Phys. Chem. Lett. 2011, 2 (6), 572–576. https://doi.org/10.1021/jz101753e.

(34) Sha, Y.; Yu, T. H.; Merinov, B. V.; Goddard, W. A. Prediction of the Dependence of the Fuel Cell Oxygen Reduction Reactions on Operating Voltage from DFT Calculations. J. Phys. Chem. C 2012, 116 (10), 6166–6173. https://doi.org/10.1021/jp207526u.

(35) Huang, Y.; Chen, Y.; Cheng, T.; Wang, L.-W.; Goddard, W. A. Identification of the Selective Sites for Electrochemical Reduction of CO to C $_{2+}$ Products on Copper Nanoparticles by Combining Reactive Force Fields, Density Functional Theory, and Machine Learning. ACS Energy Letters 2018, 2983–2988. https://doi.org/10.1021/acsenergylett.8b01933.

(36) Cheng, T.; Xiao, H.; Goddard, W. A. Nature of the Active Sites for CO Reduction on Copper Nanoparticles; Suggestions for Optimizing Performance. J. Am. Chem. Soc. 2017, 139 (34), 11642–11645. https://doi.org/10.1021/jacs.7b03300.

(37) Chen, Y.; Huang, Y.; Cheng, T.; Goddard, W. A. Identifying Active Sites for CO2 Reduction on Dealloyed Gold Surfaces by Combining Machine Learning with Multiscale Simulations. J. Am. Chem. Soc. 2019, 141 (29), 11651–11657. https://doi.org/10.1021/jacs.9b04956.

(38) Cheng, T.; Huang, Y.; Xiao, H.; Goddard, W. A. Predicted Structures of the Active Sites Responsible for the Improved Reduction of Carbon Dioxide by Gold Nanoparticles. The Journal of Physical Chemistry Letters 2017, 8 (14), 3317–3320. https://doi.org/10.1021/acs.jpclett.7b01335.

(39) Kresse, G.; Hafner, J. Ab Initio Molecular-Dynamics Simulation of the Liquid-Metal--Amorphous-Semiconductor Transition in Germanium. Phys. Rev. B 1994, 49 (20), 14251–14269. https://doi.org/10.1103/PhysRevB.49.14251.

(40) Henkelman, G.; Uberuaga, B. P.; Jónsson, H. A Climbing Image Nudged Elastic Band Method for Finding Saddle Points and Minimum Energy Paths. J. Chem. Phys. 2000, 113 (22), 9901–9904. https://doi.org/10.1063/1.1329672.

(41) Mathew, K.; Sundararaman, R.; Letchworth-Weaver, K.; Arias, T. A.; Hennig, R. G. Implicit Solvation Model for Density-Functional Study of Nanocrystal Surfaces and Reaction Pathways. J. Chem. Phys. 2014, 140 (8), 084106. https://doi.org/10.1063/1.4865107.

Chapter III

IDENTIFYING ACTIVE SITES FOR CO2 REDUCTION ON GOLD NANOPARTICLES AND DEALLOYED GOLD SURFACES

ABSTRACT

Gold nanoparticles (AuNPs) and dealloyed Au_3Fe core−shell NP surfaces have been shown to have dramatically improved performance in reducing CO2 to CO (CO2RR), but the surface features responsible for these improvements are not known. The active sites cannot be identified with surface science experiments, and quantum mechanics (QM) is not practical for the 10 000 surface sites of a 10 nm NP (200 000 bulk atoms). Here, we combine machine learning, multiscale simulations, and QM to predict the performance (a-value) of all 5000−10000 surface sites on AuNPs and dealloyed Au surfaces. We then identify the optimal active sites for CO2RR on dealloyed gold surfaces with dramatically reduced computational effort. This approach provides a powerful tool to visualize the catalytic activity of the whole surface. Comparing the a-value with descriptors from experiment, computation, or theory should provide new ways to guide the design of high-performance electrocatalysts for applications in clean energy conversion.

3.1 INTRODUCTION

The development of dramatically improved electrocatalysts is essential for economical renewable energy generation, energy storage, and utilization[1,2]. The search for new catalysts has motivated extraordinary efforts in experimental[3–8] and computational[9–12] combinatorial assays to discover new alloys or composites with some successes. Complementing this are new generations of Quantum Mechanics that have provided remarkable accuracy for simple low index surfaces: 0.05 eV for free energy reaction barriers at 298K for oxygen reduction reaction (ORR) on Pt(111)[13] and CO to ethane and ethanol on Cu(100)[14,15] and onset potentials to 0.05V at 10meV/cm2 for CORR on Cu(111)[16,17] and oxygen evolution reaction (OER) on Fe doped γ-NiOOOH[18] and IrO2(110)[19]. However, with remarkable improvement of computational tools for low index surfaces, experiments have shown dramatically improved performance for nanoparticles (NP)[20–25], and especially for dealloyed NP[26–28].

Unfortunately, there are no available experimental techniques to identify the specific active sites for nanoparticles. We have been able to predict the structure of 10 nm NPs (200,000 atoms) computationally using the ReaxFF reactive force field[29] in CVD simulations[30]. However, the accuracy of ReaxFF is not better than 0.25 eV, whereas we need the 0.05 eV accuracy of QM to properly identify the active sites. Additionally, it would be quite impractical to use QM with cluster models of the 5 to 10 thousand surface sites.

To solve this conundrum, we propose here a machine learning strategy that uses QM calculations with cluster models for hundreds of the 5 to 10 thousand surface sites of the ReaxFF grown NP, which we train iteratively to attain 0.05 eV accuracy. Then we use this ML predictive model to predict the performance of all 5 to 10 thousand surface sites. Then we analyze the sites with the highest predicted performance (a-value) to discover the specific sites responsible for the superior performance. These results can then be used as a guide for both experimental and computational attempts to maximize the number of sites having this performance. In addition, we can compare the predicted performance of all 5 to 10 thousand sites with other properties that might be measured experimentally (XPS, electronic density of states, local character of s,p,d orbitals, work function) in order to identify descriptors that might be used in monitoring attempts to synthesize materials with a high density of high-performing sites.

We illustrate this new methodology here for the case of Au NP. Our previous experimental studies of the dealloyed Au_3Fe core-shell NP led to spectacular results, a 100-fold increase in mass activity compared with AuNP , a 500 meV improvement in the overpotential for >80% faradaic efficiency (FE) of CO2 to CO^{27} compared with Au foils. Similar dramatic improvements from dealloying have also been observed in PtNi alloy catalysts that 2nm pure Pt NW formed by dealloying from 5nm Ni_7Pt_3 NW showing ORR performance 50 time better than Pt^{28}. We expect that this must be related to the nature of the dealloyed surface. In this paper, we predict the performance of the sites achieved by dealloying.

3.2 RESULTS AND DISCUSSION

3.2.1 Synthesis and Structure Analysis of AuNPs

We synthesized the 10nm gold nanoparticle on the carbon nanotube support using ReaxFF reactive molecular dynamics as described *in B1 of Supporting Information*. Surface atoms and bulk atoms are distinguished based on the surface vector method using an 8 Å nanocluster model. We showed that in our earlier work[30,31], such 8 Å clusters already include the geometric features that determine the adsorption energy (to an accuracy of 0.02 eV). More details are included in *B2 of Supporting Information*. The whole nanoparticle system has 211619 atoms with 43200 carbon atoms and 168419 gold atoms, from which we extracted 16919 surface atoms using our surface vector method. These 16919 surfaces sites are partitioned into six groups based on their coordination number, which range from six to eleven. Here, first-neighbor are defined as those lying within a distance of 3.3Å from center atom. We choose the cutoff distance according to the radial distribution functions in Figure B-3(a), where the first peak appears at the distance of 2.80 Å and second peak at 4.20 Å. The surface sites distribution toward coordination number is also shown in Figure B-3(b).

From the reaction mechanism revealed by our previous work[32] and works from others[33,34], we choose two physical descriptors for evaluating the activity of a given site:

- CO adsorption energy(ΔE_{CO})

$$\Delta E_{CO} = E_{*CO} - E_* - E_{CO}$$

- HOCO transition state formation energy (ΔE_{HOCO}):

$$\Delta E_{HOCO} = E_{*HOCO} - E_* - E_{CO2} - 0.5 * E_{H2}$$

These two descriptors have been proposed and used in other works[30] as well. We expect that sites with high coordination (10 and 11) should be inactive for CO2RR since there is insufficient space to bind reactants, intermediates, or products. Therefore, we investigated these high coordination sites first by randomly selecting 50 sites from the group of coordination 10 and 50 sites from the group of coordination 11. We then carried out DFT calculations (*B3 of Supporting Information*) for ΔE_{HOCO} on these 100 sites. Among these 100 sites, 96 sites cannot even adsorb the important intermediate of the reaction (HOCO) and the other 4 sites show very high ΔE_{HOCO}. This shows that such high coordination sites

are not active. Thus, we narrowed our search to sites with coordination smaller than 10. Even so, there remain 11537 surface sites on the surface to be explored.
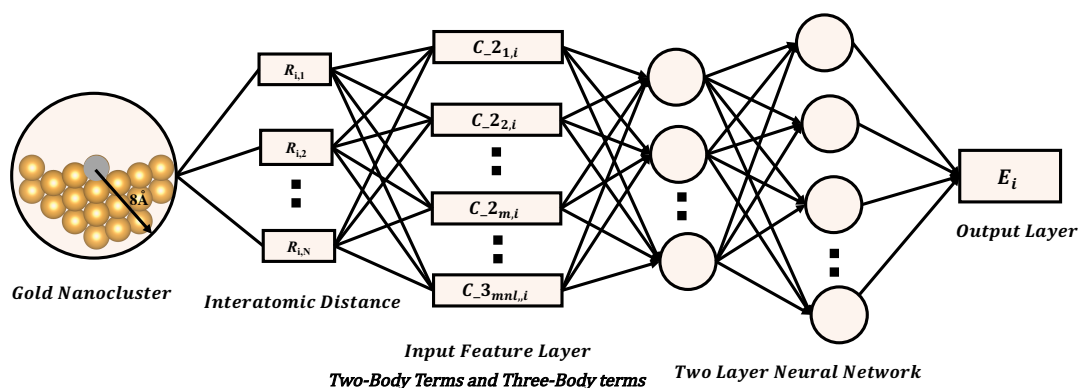

Figure 3-1. Overall Structure of Neural Network. We use two-body terms(C_2) and three-body terms(C_3) to represent the local geometric feature of the selected surface atom (gray atom) extracted from 8 Å nanocluster model. A fully connected two-layer neural network with 30 nodes in the first layer and 50 nodes in the second layer are following to fit the physical descriptor, with the total number of 2801 model parameters. The training targets E_i for two neural networks in this work are ΔE_{CO} and ΔE_{HOCO} with all training data generated from DFT calculations.

3.2.2 Training Data Generation and Neural Network Model Implementation

We trained two neural networks separately: CO adsorption energy (ΔE_{CO}) and HOCO transition state formation energy (ΔE_{OCOH}). The overall model topology is shown schematically in Figure 3-1. This type of feature representation method is derived from the work by Behler and Parrinello in 2007[35]. Instead of using Gaussian functions, we choose another type of symmetry function: localized piecewise cosine function. This representative method has earlier been proposed and used by others[36,37]. We used an 8 Å nanocluster from the surface atom to extract local geometric features of selected surface sites as the neural network input through symmetry functions. In our model, we use 12 symmetry functions for two-body terms and 3 symmetry functions for three-body terms, leading to 39 input features. We consider this to give the best balance between training dataset size and model complexity. Having defined a set of features, we used a fully connected two-layer neural network with 30 nodes in the first layer and 50 nodes in the

second layer for independently fitting two selected physical descriptors: ΔE_{CO} and ΔE_{HOCO}. The total number of parameters in the model is 2801. Mathematical representations and more details about neural networks are included in B5 of Supporting Information.

We first trained a neural network for ΔE_{CO} using 1384 data from DFT calculations. This data was partitioned into 1104 in the training set, 140 in the validation set, and 140 in the testing set. We constrained the ratio of sites from different coordination groups to be equal within each of the three data sets, but all three sets are totally independent. The validation set is used to prevent overfitting (early-stop). Distributions and partitions of the data are listed in Table B-1 and the training trajectory is shown in Figure B-4. The root mean squared error (RMSE) of the validation set reached the minimum at the training epoch of 19000 with the training set RMSE at 0.0563 eV and the validation set RMSE at 0.0591 eV. The prediction results for the independent testing set are shown in Figure 3-2(a) leading to RMSE = 0.0521 eV. Using the same approach, we trained our second neural network for ΔE_{HOCO} using 1059 data points from DFT calculations. Distribution and partition of the data are listed in Table B-2 and the training trajectory is shown in Figure B-4(b). The validation set RMSE reached the minimum at the training epoch of 11000 with the RMSE of training set at 0.0616 eV and the validation set RMSE is 0.0591 eV. Figure 3-2(b) shows the prediction results on the independent testing set of ΔE_{HOCO}, showing RMSE = 0.0614 eV. Our two machine learning models based on the neural network algorithm show RMSE of 0.0521 eV for CO adsorption energy and 0.0614 eV for HOCO formation energy on testing sets. To place our model accuracy in a more straightforward context, we compared our errors to a similar work in predicting CO adsorption energy in Thiolated Ag-alloyed Au nanoclusters[38], which finds a much higher RMSE at ~0.17eV using over 2000 data points for training. Another work using machine learning for predicting adsorption energies of CH4 related species (CH3, CH2, CH, C, and H) on the Cu-based alloys[39] reported the best performance of RMSEs around 0.3 eV after an extra tree regression algorithm. Our model complexity (determined by feature representation and neural network structure) and data set size have the best balance, giving much smaller errors compared to previous works.
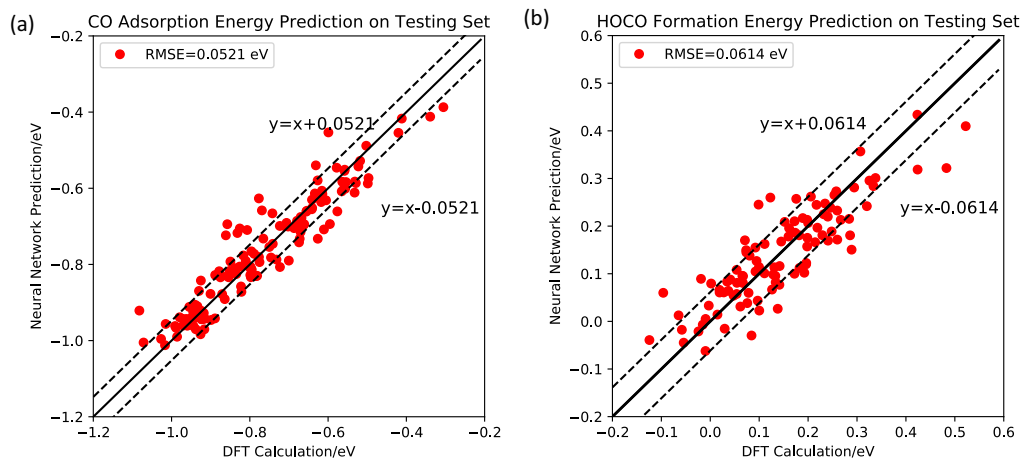
(a) CO Adsorption Energy Prediction on Testing Set — RMSE=0.0521 eV; y=x+0.0521; y=x-0.0521

(b) HOCO Formation Energy Prediction on Testing Set — RMSE=0.0614 eV; y=x+0.0614; y=x-0.0614

Figure 3-2. (a) Neural network predictions on the testing set for CO adsorption energy (ΔE_{CO}) shows an RMSE of 0.0521 eV; (b) Neural network predictions on the testing set for HOCO formation energy ΔE_{HOCO} shows an RMSE of 0.0614 eV.

3.2.3 Model Application

3.2.3.1 Identification of Active Sites on the AuNP Surface

We used the two neural networks trained above to predict ΔE_{CO} and ΔE_{HOCO} for all 11537 surface sites obtained as described in *Section 3.2.1*. The prediction results are shown in Figure 3-3, where ΔE_{HOCO} is along the x axis and ΔE_{CO} along the y axis. We show with different colors surface sites having different coordination. We observe a correlation between catalytic behavior and coordination. The group with coordination six shows both strongest CO binding and lowest HOCO formation energy while the group with coordination nine shows the weakest CO binding and highest HOCO formation energy. We see a general linear relationship between ΔE_{CO} and ΔE_{HOCO}, which is consistent with earlier studies[30,40].

We mark the characteristics for two low index surfaces (Au(111) and Au(110)) in Figure 3-3. The 111 surface is generally the most stable for Au while 110 Edge sites are proposed as the most active sites in earlier studies[41]. In general, the predicted performance of the other surface sites on AuNPs surround that of the low index surfaces since the nanoparticle surfaces are irregular and disordered.
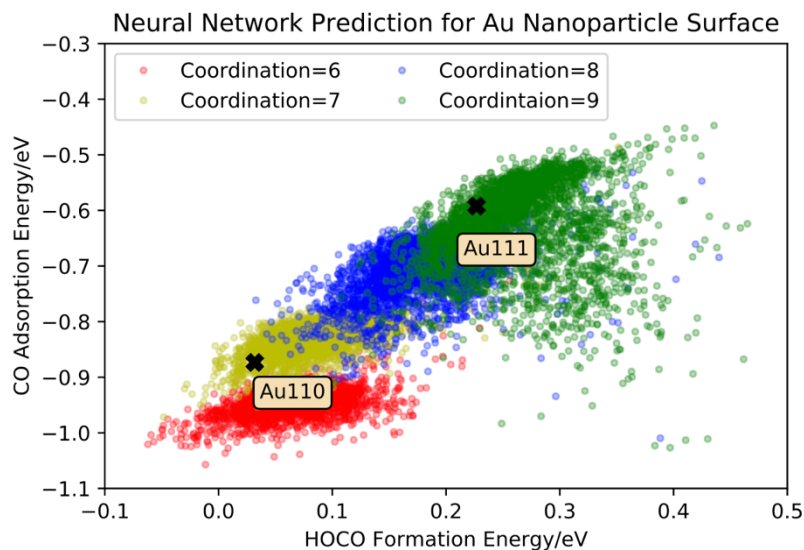
Figure 3-3. Neural network predictions for all 11537 lower coordination surface sites of AuNPs. ΔE_{CO} is placed along the y-axis and ΔE_{HOCO} along the x-axis. All sites are colored based on their coordination number, with Au(111) and Au(110) marked for reference. The general linear relationship between ΔE_{CO} and ΔE_{HOCO} remains and we observe a correlation between coordination and catalytic activity.

To provide a quantitative measure of performance, we used the straight line connecting Au111 to Au110, which is $\Delta E_{CO}=1.4423*\Delta E_{HOCO}-0.9194$. By moving this line upwards and downwards, we get a family of lines with the same slope (1.4423) but different intercepts: $\Delta E_{CO}=1.4423*\Delta E_{HOCO}+a$. For each single surface site, with the neural network predicted ΔE_{CO} and ΔE_{HOCO}, the a-value can be calculated by: $a=\Delta E_{CO}-1.4423*\Delta E_{HOCO}$. According to the reaction mechanism of CO2RR on Cu100 surface[32], the active sites we are looking for should have: low ΔE_{HOCO}, as this is the potential-determining step (PDS), lower ΔE_{HOCO} indicates higher CO2RR; high ΔE_{CO}, as higher ΔE_{CO} indicates that more sites will be released after the reaction. Thus, we expect that the a-value (defined by ΔE_{CO} and ΔE_{HOCO}) will indicate the overall performance of a given surface site. Larger a-value means higher CO2RR while smaller a-value indicates poor performance. The top 300 sites ranked by their a-value are marked in the Figure 3-4. We found that top 300 sites (out of 11537) can be classified into seven groups, each with distinctive characteristics. We show in Figure 3-4 one representative structure of each group (more structures are attached in Figure B-9~B-15 *of*

the SI). We could not find a simple quantitative definition of each group, but we summarize the structure of each group as following:

o **Step111**: Center atom has Au111 features but with steps around the center atom;

o **StepUnder111**: Center atom has under-coordinated Au111 features but with steps around the center atom;

o **Step110**: Center atom has 110 features but with steps around the center atom;

o **Step311**: Center atom has 311 features but with steps around the center atom;

o **StepTB**: Center atom has twin boundary features but with steps around the center atom;

o **StepUnderTB**: Center atom has the under-coordinated twin boundary feature but with steps around the center atom;

o **SurfaceDefect**: Au111 surface but with one or two missing atoms around the center atom.
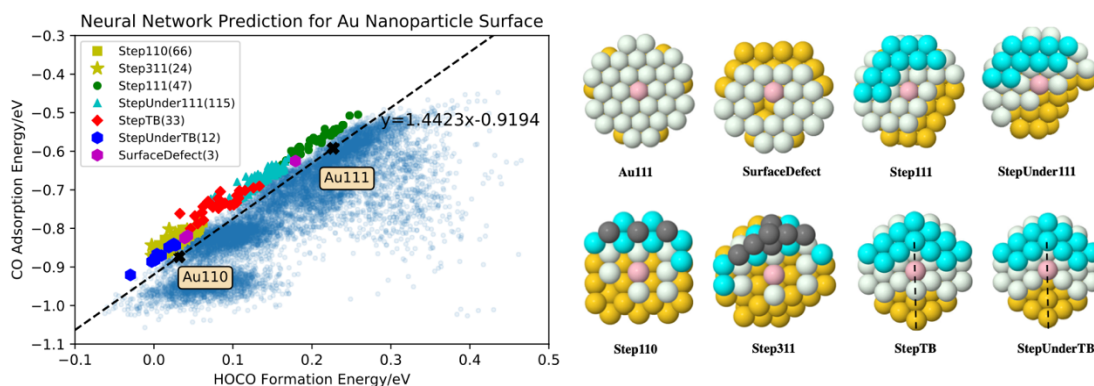
Figure 3-4. Active sites identification for AuNPs surfaces. We ranked the activity of all 11537 surface sites based on their a-values and identified the top 300 sites. We classified these 300 sites into seven groups, as marked in the figure. The number of sites in each group is indicated in brackets next to the marker. A representative structure for each of the 7 Active Groups are shown. The center atom is pink, while atoms at the same layer are white. Atoms in the layer below white atoms are gold, while atoms one layer above center atom are cyan. Atoms above cyan atoms are gray and twin boundaries are dashed line.

For better comparison, we randomly selected 300 sites from whole surface with the identification results showing in Figure B-6. The comparison between top 300 sites (Figure 3-4) and randomly selected 300 sites are shown on Table B-3. Among 300 randomly selected sites, the majority do not belong to the seven active groups as defined above. Thus, only the seven active groups are concentrated above and around straight line with a-value = 0.9194.

3.2.3.2 Dealloyed Gold Surface Modeling and Active Sites Identification

Compared to AuNPs and Au foils, dealloyed Au surfaces have been shown experimentally to have dramatically improved performance in reducing CO2 to CO. Thus, starting with a Au_3Fe NP and exposing to electrochemical conditions suitable for CO2 reduction, Wang, Goddard, and coworkers showed that a core-shell NP is formed in which Fe is depleted from the top layers. Remarkably this Au_3Fe core-shell nanoparticle (CSNP) showed a 100-fold increase in mass activity compared with AuNP. Moreover it leads to >80% FE at - 0.2 V, which is 500 meV lower than for Au foils[27]! Using QM studies on the 111 surface of Au_3M for 20 different M, Fe had been selected as best. But these calculations did not suggest such dramatically improved performance. It must be that the nature of this dealloyed surface somehow dramatically improves the reduction of CO2 to CO, but the type of site that can do this remains completely mysterious.

However, Similar dramatic improvements from dealloying have been observed previously in PtNi alloy catalysts for ORR. Here Debe and coworkers discovered that Ni_7Pt_3 NP leads to 4 times improved activity over Pt[26], but their XPS studies could not find that any Ni remained, suggesting that it was fully dealloyed. Fortunelli and Goddard followed up using ReaxFF to show that the dealloyed 5nm Ni_7Pt_3 NP leads to a porous surface with a preponderance of low coordination sites[42]. They found that the surface area was doubled over a NP (in agreement with experiment) and that one important step in the reaction, $O^* + H2O^* \rightarrow 2\ OH^*$, is dramatically accelerated on these sites. Later Huang, Duan, Goddard, and coworkers showed that 5nm Ni_7Pt_3 nanowires (NW) after dealloying under ORR conditions lead to 2nm pure Pt NW with ORR performance 50 time better than Pt[28]! The sites responsible for this dramatic improvement have not yet been identified.

To search for sites on the dealloyed Au NP surfaces responsible for the dramatic improvement in activity, we modelled the de-alloyed Au surface by cutting a 10 nm Au sphere from the single crystal and randomly removing 25% of the surface Au and then allowing the structure to relax using ReaxFF. More detailed description of the model and structure equilibration are included in B4 of Supporting Information. We assume in our calculations the extreme hypothesis that the catalytic activity is not affected by the Fe in the core, nor from electronic effects or strain effect caused by lattice mismatch. This assumption may be valid since the Fe may be too far from the surface in the experiments. Thus, we leached out Au just at the top layer of the system. We show below that this simplifying assumption may be sufficient because we do predict dramatically improved CO2RR based on this hypothesis. If follow-up studies using QM on the structures we identify here turn out not to predict the dramatic 500 mV decrease in the onset potential for >80% FE, we will consider dealloying multiple layers using ReaxFF to relax the structures. If this does not explain the improvements, then we will add in ¼ Fe in the core. We expect that this sequence of studies combining QM, ReaxFF, and machine learning will eventually identify the mechanism. We show below that this simple model provides insights and reasonable hypotheses to explain the dramatically improved performance.

Using the same methodology as in *Section 3.2.3.1*, we predicted the performance of this dealloyed Au surface using our neural networks. To have a more quantitative comparison, we define the active ratio(AR) as following first:

$$AR = \frac{Number\ of\ Sites\ with\ a > 0.9194}{Total\ Number\ of\ Surface\ Sites}$$

where 0.9194 is the a value of Au(111) and Au(110).

Figure 3-5 shows a normalized distribution of a-value comparisons, where the dashed line is the a-value for low index Au surfaces, Au(111) and Au(110). The red histogram is the distribution for AuNPs while the blue histogram is the distribution for dealloyed Au surfaces. AR is then the area lying at the right of the dashed line, since the total area of each plot is normalized to 1. Comparing to low index Au surfaces (dashed line), AuNPs and de-alloyed Au surfaces both have increased numbers of active sites, with AR = 0.0836 for AuNPs and

AR= 0.1307 for the dealloyed surface. This is consistent with experimental studies showing that dealloyed surface exhibits much better performance than AuNPs, which in turn are better than Au foils.
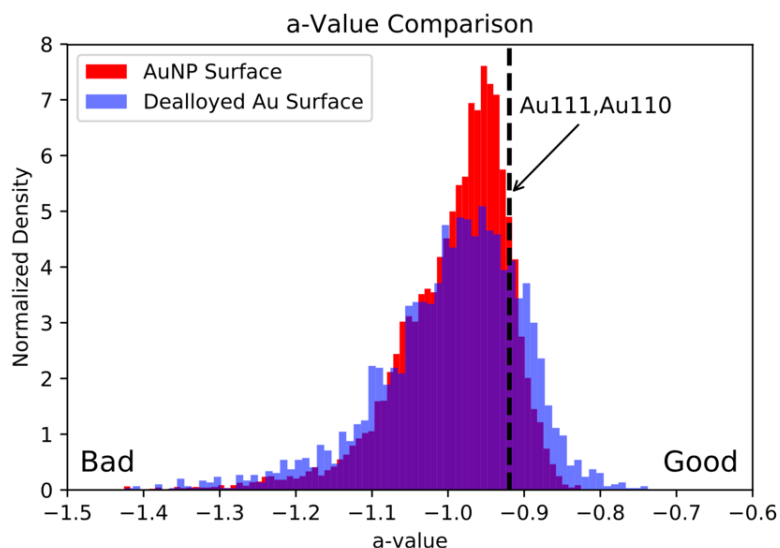

Figure 3-5. Normalized a-Value Distribution. The total area of each histogram is normalized to 1. As defined, AR (active ratio) is the area at the right of the dashed line for each plot. Both AuNPs and dealloyed surface have a number of active sites with a-value larger than 0.9194, which is the a-value of Au(111) and Au(110). The Dealloyed surface shows even better performance with AR at 0.1307 compared to the AR for AuNPs at 0.0836.

Active site identification for the dealloyed Au surface is shown in Figure 3-6. Among the Top 100 sites out of 3095 ranked by a-value,

- 43 of them arise from the StepUnder111 group;

- 23 of them are from the SurfaceDefect group.

which we consider as the most promising. there are also 23 sites from Step111 group and small numbers of sites from the Step110 and Step311 groups, but we consider them as less likely contributors to the dramatically improved performance, partly because these kinds of sites may already be present before dealloying. We expect dealloying will naturally

create such structure defects as under-coordinated sites. Therefore, we expect the increased fraction of SurfaceDefect and StepUnder111 groups to be responsible for the improved performance.

In this example, we illustrate how to apply machine learning model to analyze and understand extremely irregular and disordered systems. This leads to new structures that can be tested with realistic QM based studies to validate the predictions, the ultimate goal is to validate the success for our ML-QM-ReaxFF strategy. Here we eschew the exact modeling of the de-alloying process, which requires complicated and expensive calculations. To further verify neural network prediction results, we randomly selected 5 sites from each of the 7 groups and carried out DFT cluster calculations (no solvation). Figure B-7 *and* Figure B-8 show that our predicted energy for both ΔE_{CO} and for ΔE_{HOCO} are mostly within the RMSE of the neural network predictions (0.0521eV for ΔE_{CO} and 0.0614 eV for ΔE_{HOCO}). This validates the accuracy of our ML model. It also validates that these seven groups are those sites with higher CO2RR.
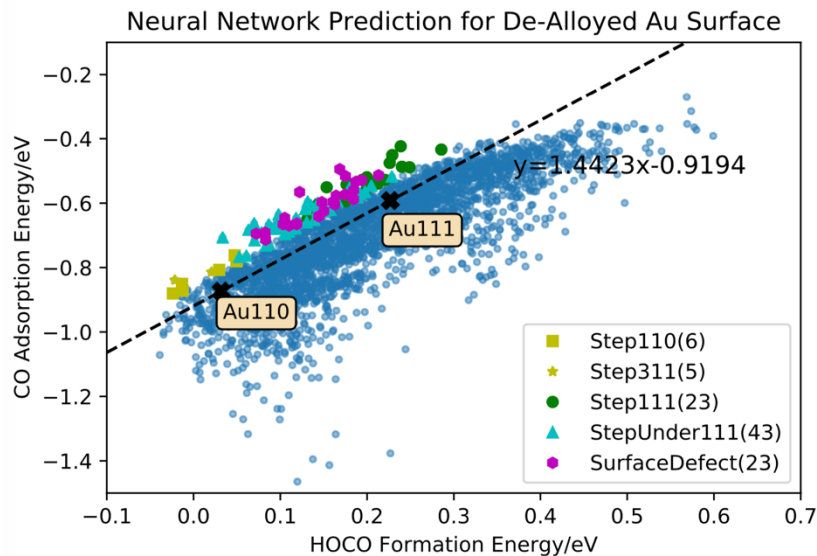

Figure 3-6. Active Sites Identification for Dealloyed Au Surfaces. The Top 100 sites out of 3095 are marked with the number in each group shown in brackets next to the marker. As Step110, Step 311 and Step111 may already be present before dealloying, we expect that the creation of increased StepUnder111 and SurfaceDefect sites by the dealloying

process is likely the main contributor to the dramatically improved performance of the dealloyed Au$_3$Fe CSNP.

3.2.3.3 a-Value Mapping and Catalytic Activity Visualization

One important application of our machine learning model is to evaluate the performance of each single site even on a highly disordered and irregular surface. The catalytic activity can be visualized by mapping the a-value back on the particle. As shown in Figure 3-7, all the sites are colored based on its predicted a-value. The red sites are poor sites with small a-values and the blue sites are active sites showing larger a-values. Three common surfaces of Au(111), Au(110), Au 100) are marked in Figure 3-7(a), showing that Au(111) and Au(110) with the color blue have better performance at CO2RR than Au(100) with the color green, which is consistent with earlier experimental and computational studies[23,41]. Two main contributors for the dramatically improved performance of dealloyed Au surfaces, SurfaceDefect and StepUnder111 sites, are also marked in Figure 3-7(b), with the color of blue to indicate they have high-performance. Our a-value mapping provides a powerful tool for catalytic activity visualization.

We can also map descriptors from experiment, computation, or theory onto a companion diagram in order to provide guidance toward physical descriptors to design high-performance electrocatalysts for applications in electrocatalysis.
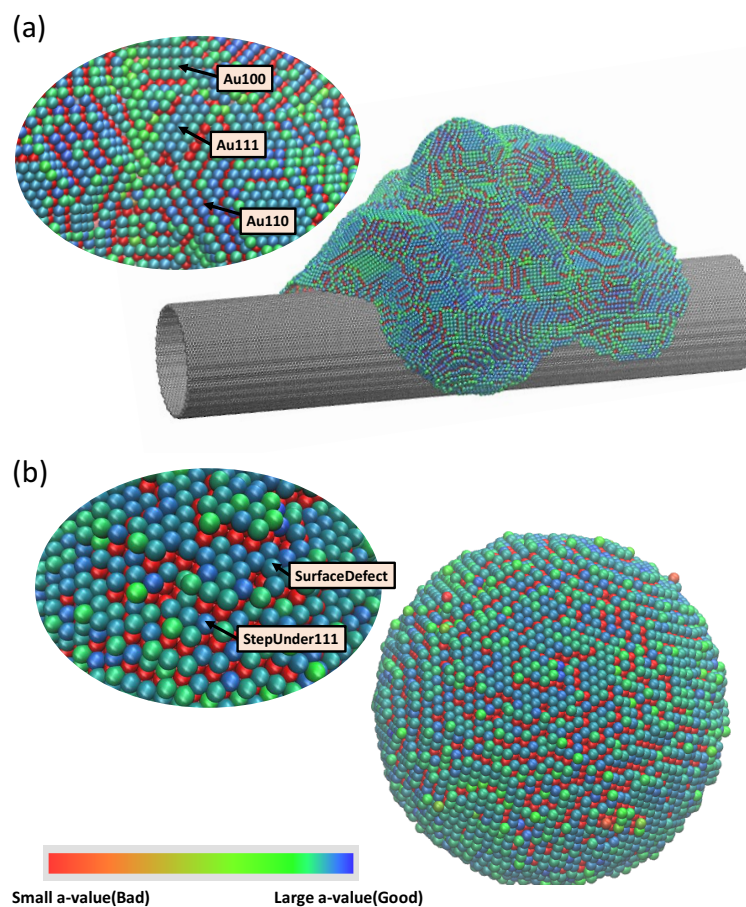
Figure 3-7. a-Value Mapping and Catalytic Activity Visualization. Each single site is given a a-value based on NN prediction. These a-values are then mapped back on the particle to visualize the catalytic activity of the whole surface. As indicated in the color bar, the red sites are inactive sites and the blue sites are active ones. (a) Catalytic Visualization for AuNPs. Au (111), Au (110) and Au(100) are marked; (b) Catalytic Visualization for Dealloyed Au surface. SurfaceDefect and StepUnder111 sites are marked with the color of blue, indicating they have high-performance at CO2RR.

3.3 CONCLUSION

In summary, we developed two neural network based machine learning models for accurate prediction of CO adsorption energy and HOCO formation energy on extremely irregular and disordered Au surfaces, showing the accuracy of 0.05 eV needed for catalyst development.

The model applications to Au nanoparticles and dealloyed Au surfaces allow us to identify the feature of active sites responsible for the dramatically improved CO2RR performance of such disordered and irregular surfaces. We also develop an a-value mapping methodology to construct and visualize the catalytic activity of whole surface. We expect that this can help guide the design of high-performance electrocatalysts for CO2RR to enable storing of solar generated energy and for CO2 free transportation. This provides an example of how to combine multiscale simulations, QM, and artificial intelligence to drive the discovery of new catalysts for clean energy conversion.

ACKNOWLEDGMENT

BIBLIOGRAPHY

(1) Goeppert, A.; Czaun, M.; Jones, J.-P.; Surya Prakash, G. K.; Olah, G. A. Recycling of Carbon Dioxide to Methanol and Derived Products – Closing the Loop. Chem. Soc. Rev. 2014, 43 (23), 7995–8048. https://doi.org/10.1039/C4CS00122B.

(2) Whipple, D. T.; Kenis, P. J. A. Prospects of CO2 Utilization via Direct Heterogeneous Electrochemical Reduction. The Journal of Physical Chemistry Letters 2010, 1 (24), 3451–3458. https://doi.org/10.1021/jz1012627.

(3) Greeley, J.; Stephens, I. E. L.; Bondarenko, A. S.; Johansson, T. P.; Hansen, H. A.; Jaramillo, T. F.; Rossmeisl, J.; Chorkendorff, I.; Nørskov, J. K. Alloys of Platinum and Early Transition Metals as Oxygen Reduction Electrocatalysts. Nature Chem 2009, 1 (7), 552–556. https://doi.org/10.1038/nchem.367.

(4) Hatsukade, T.; Kuhl, K. P.; Cave, E. R.; Abram, D. N.; Feaster, J. T.; Jongerius, A. L.; Hahn, C.; Jaramillo, T. F. Carbon Dioxide Electroreduction Using a Silver-Zinc Alloy. Energy Technol. 2017, 5 (6), 955–961. https://doi.org/10.1002/ente.201700087.

(5) Clark, E. L.; Hahn, C.; Jaramillo, T. F.; Bell, A. T. Electrochemical CO 2 Reduction over Compressively Strained CuAg Surface Alloys with Enhanced Multi-Carbon Oxygenate Selectivity. J. Am. Chem. Soc. 2017, 139 (44), 15848–15857. https://doi.org/10.1021/jacs.7b08607.

(6) Tang, M. H.; Hahn, C.; Klobuchar, A. J.; Ng, J. W. D.; Wellendorff, J.; Bligaard, T.; Jaramillo, T. F. Nickel–Silver Alloy Electrocatalysts for Hydrogen Evolution and Oxidation in an Alkaline Electrolyte. Phys. Chem. Chem. Phys. 2014, 16 (36), 19250. https://doi.org/10.1039/C4CP01385A.

(7) Mendes, L. V. P.; Snider, J. L.; Fleischman, S. D.; Kibsgaard, J.; McEnaney, J. M.; Aranda, D. A. G.; Jaramillo, T. F. Polyol Synthesis of Cobalt–Copper Alloy Catalysts for Higher Alcohol Synthesis from Syngas. Catal Lett 2017, 147 (9), 2352–2359. https://doi.org/10.1007/s10562-017-2130-5.

(8) Hahn, C.; Abram, D. N.; Hansen, H. A.; Hatsukade, T.; Jackson, A.; Johnson, N. C.; Hellstern, T. R.; Kuhl, K. P.; Cave, E. R.; Feaster, J. T.; et al. Synthesis of Thin Film AuPd Alloys and Their Investigation for Electrocatalytic CO 2 Reduction. J. Mater. Chem. A 2015, 3 (40), 20185–20194. https://doi.org/10.1039/C5TA04863J.

(9) Zheng, X.; Ji, Y.; Tang, J.; Wang, J.; Liu, B.; Steinrück, H.-G.; Lim, K.; Li, Y.; Toney, M. F.; Chan, K.; et al. Theory-Guided Sn/Cu Alloying for Efficient CO2 Electroreduction at Low Overpotentials. Nat Catal 2019, 2 (1), 55–61. https://doi.org/10.1038/s41929-018-0200-8.

(10) Hansen, H. A.; Shi, C.; Lausche, A. C.; Peterson, A. A.; Nørskov, J. K. Bifunctional Alloys for the Electroreduction of CO 2 and CO. Phys. Chem. Chem. Phys. 2016, 18 (13), 9194–9201. https://doi.org/10.1039/C5CP07717F.

(11) Qian, J.; Fortunelli, A.; Goddard, W. A. Effect of Co Doping on Mechanism and Kinetics of Ammonia Synthesis on Fe(1 1 1) Surface. Journal of Catalysis 2019, 370, 364–371. https://doi.org/10.1016/j.jcat.2019.01.001.

(12) Cheng, M.-J.; Clark, E. L.; Pham, H. H.; Bell, A. T.; Head-Gordon, M. Quantum Mechanical Screening of Single-Atom Bimetallic Alloys for the Selective Reduction of CO 2 to C 1 Hydrocarbons. ACS Catal. 2016, 6 (11), 7769–7777. https://doi.org/10.1021/acscatal.6b01393.

(13) Cheng, T.; Goddard, W. A.; An, Q.; Xiao, H.; Merinov, B.; Morozov, S. Mechanism and Kinetics of the Electrocatalytic Reaction Responsible for the High Cost of Hydrogen Fuel Cells. Physical Chemistry Chemical Physics 2017, 19 (4), 2666–2673. https://doi.org/10.1039/C6CP08055C.

(14) Cheng, T.; Xiao, H.; Goddard, W. A. Full Atomistic Reaction Mechanism with Kinetics for CO Reduction on Cu(100) from Ab Initio Molecular Dynamics Free-Energy Calculations at 298 K. Proc Natl Acad Sci USA 2017, 114 (8), 1795–1800. https://doi.org/10.1073/pnas.1612106114.

(15) Cheng, T.; Xiao, H.; Goddard, W. A. Free-Energy Barriers and Reaction Mechanisms for the Electrochemical Reduction of CO on the Cu(100) Surface, Including Multiple Layers

of Explicit Solvent at PH 0. J. Phys. Chem. Lett. 2015, 6 (23), 4767–4773. https://doi.org/10.1021/acs.jpclett.5b02247.

(16) Xiao, H.; Cheng, T.; Goddard, W. A.; Sundararaman, R. Mechanistic Explanation of the PH Dependence and Onset Potentials for Hydrocarbon Products from Electrochemical Reduction of CO on Cu (111). J. Am. Chem. Soc. 2016, 138 (2), 483–486. https://doi.org/10.1021/jacs.5b11390.

(17) Xiao, H.; Cheng, T.; Goddard, W. A. Atomistic Mechanisms Underlying Selectivities in C 1 and C 2 Products from Electrochemical Reduction of CO on Cu(111). J. Am. Chem. Soc. 2017, 139 (1), 130–136. https://doi.org/10.1021/jacs.6b06846.

(18) Shin, H.; Xiao, H.; Goddard, W. A. In Silico Discovery of New Dopants for Fe-Doped Ni Oxyhydroxide (Ni 1– x Fe x OOH) Catalysts for Oxygen Evolution Reaction. J. Am. Chem. Soc. 2018, 140 (22), 6745–6748. https://doi.org/10.1021/jacs.8b02225.

(19) Ping, Y.; Nielsen, R. J.; Goddard, W. A. The Reaction Mechanism with Free Energy Barriers at Constant Potentials for the Oxygen Evolution Reaction at the IrO 2 (110) Surface. J. Am. Chem. Soc. 2017, 139 (1), 149–155. https://doi.org/10.1021/jacs.6b07557.

(20) Kim, D.; Kley, C. S.; Li, Y.; Yang, P. Copper Nanoparticle Ensembles for Selective Electroreduction of CO 2 to C 2 –C 3 Products. Proc Natl Acad Sci USA 2017, 114 (40), 10560–10565. https://doi.org/10.1073/pnas.1711493114.

(21) Chen, Y.; Li, C. W.; Kanan, M. W. Aqueous CO2 Reduction at Very Low Overpotential on Oxide-Derived Au Nanoparticles. Journal of the American Chemical Society 2012, 134 (49), 19969–19972. https://doi.org/10.1021/ja309317u.

(22) Li, C. W.; Ciston, J.; Kanan, M. W. Electroreduction of Carbon Monoxide to Liquid Fuel on Oxide-Derived Nanocrystalline Copper. Nature 2014, 508 (7497), 504–507. https://doi.org/10.1038/nature13249.

(23) Back, S.; Yeom, M. S.; Jung, Y. Active Sites of Au and Ag Nanoparticle Catalysts for CO2 Electroreduction to CO. ACS Catalysis 2015, 5 (9), 5089–5096. https://doi.org/10.1021/acscatal.5b00462.

(24) Zhu, W.; Michalsky, R.; Metin, Ö.; Lv, H.; Guo, S.; Wright, C. J.; Sun, X.; Peterson, A. A.; Sun, S. Monodisperse Au Nanoparticles for Selective Electrocatalytic Reduction of CO 2 to CO. Journal of the American Chemical Society 2013, 135 (45), 16833–16836. https://doi.org/10.1021/ja409445p.

(25) Zhao, S.; Jin, R.; Jin, R. Opportunities and Challenges in CO2 Reduction by Gold- and Silver-Based Electrocatalysts: From Bulk Metals to Nanoparticles and Atomically Precise Nanoclusters. ACS Energy Letters 2018, 3 (2), 452–462. https://doi.org/10.1021/acsenergylett.7b01104.

(26) Stevens, D. A.; Mehrotra, R.; Sanderson, R. J.; Vernstrom, G. D.; Atanasoski, R. T.; Debe, M. K.; Dahn, J. R. Dissolution of Ni from High Ni Content Pt1−xNix Alloys. J. Electrochem. Soc. 2011, 158 (8), B905. https://doi.org/10.1149/1.3595747.

(27) Sun, K.; Cheng, T.; Wu, L.; Hu, Y.; Zhou, J.; Maclennan, A.; Jiang, Z.; Gao, Y.; Goddard, W. A.; Wang, Z. Ultrahigh Mass Activity for Carbon Dioxide Reduction Enabled by Gold–Iron Core–Shell Nanoparticles. Journal of the American Chemical Society 2017, 139 (44), 15608–15611. https://doi.org/10.1021/jacs.7b09251.

(28) Li, M.; Zhao, Z.; Cheng, T.; Fortunelli, A.; Chen, C.-Y.; Yu, R.; Zhang, Q.; Gu, L.; Merinov, B. V.; Lin, Z.; et al. Ultrafine Jagged Platinum Nanowires Enable Ultrahigh Mass Activity for the Oxygen Reduction Reaction. Science 2016, 354 (6318), 1414–1419. https://doi.org/10.1126/science.aaf9050.

(29) van Duin, A. C. T.; Dasgupta, S.; Lorant, F.; Goddard, W. A. ReaxFF: A Reactive Force Field for Hydrocarbons. The Journal of Physical Chemistry A 2001, 105 (41), 9396–9409. https://doi.org/10.1021/jp004368u.

(30) Cheng, T.; Huang, Y.; Xiao, H.; Goddard, W. A. Predicted Structures of the Active Sites Responsible for the Improved Reduction of Carbon Dioxide by Gold Nanoparticles. The Journal of Physical Chemistry Letters 2017, 8 (14), 3317–3320. https://doi.org/10.1021/acs.jpclett.7b01335.

(31) Cheng, T.; Xiao, H.; Goddard, W. A. Nature of the Active Sites for CO Reduction on Copper Nanoparticles; Suggestions for Optimizing Performance. J. Am. Chem. Soc. 2017, 139 (34), 11642–11645. https://doi.org/10.1021/jacs.7b03300.

(32) Cheng, T.; Xiao, H.; Goddard, W. A. Reaction Mechanisms for the Electrochemical Reduction of CO 2 to CO and Formate on the Cu(100) Surface at 298 K from Quantum Mechanics Free Energy Calculations with Explicit Water. Journal of the American Chemical Society 2016, 138 (42), 13802–13805. https://doi.org/10.1021/jacs.6b08534.

(33) Nie, X.; Esopi, M. R.; Janik, M. J.; Asthagiri, A. Selectivity of CO 2 Reduction on Copper Electrodes: The Role of the Kinetics of Elementary Steps. Angewandte Chemie International Edition 2013, 52 (9), 2459–2462. https://doi.org/10.1002/anie.201208320.

(34) Luo, W.; Nie, X.; Janik, M. J.; Asthagiri, A. Facet Dependence of CO 2 Reduction Paths on Cu Electrodes. ACS Catalysis 2016, 6 (1), 219–229. https://doi.org/10.1021/acscatal.5b01967.

(35) Behler, J.; Parrinello, M. Generalized Neural-Network Representation of High-Dimensional Potential-Energy Surfaces. Physical Review Letters 2007, 98 (14). https://doi.org/10.1103/PhysRevLett.98.146401.

(36) Huang, Y.; Chen, Y.; Cheng, T.; Wang, L.-W.; Goddard, W. A. Identification of the Selective Sites for Electrochemical Reduction of CO to C 2+ Products on Copper Nanoparticles by Combining Reactive Force Fields, Density Functional Theory, and Machine Learning. ACS Energy Letters 2018, 2983–2988. https://doi.org/10.1021/acsenergylett.8b01933.

(37) Huang, Y.; Kang, J.; Goddard, W. A.; Wang, L.-W. Density Functional Theory Based Neural Network Force Fields from Energy Decompositions. Physical Review B 2019, 99 (6), 064103. https://doi.org/10.1103/PhysRevB.99.064103.

(38) Panapitiya, G.; Avendaño-Franco, G.; Ren, P.; Wen, X.; Li, Y.; Lewis, J. P. Machine-Learning Prediction of CO Adsorption in Thiolated, Ag-Alloyed Au Nanoclusters. Journal of the American Chemical Society 2018, 140 (50), 17508–17514. https://doi.org/10.1021/jacs.8b08800.

(39) Chowdhury, A. J.; Yang, W.; Walker, E.; Mamun, O.; Heyden, A.; Terejanu, G. A. Prediction of Adsorption Energies for Chemical Species on Metal Catalyst Surfaces Using Machine Learning. The Journal of Physical Chemistry C 2018, 122 (49), 28142–28150. https://doi.org/10.1021/acs.jpcc.8b09284.

(40) Peterson, A. A.; Nørskov, J. K. Activity Descriptors for CO 2 Electroreduction to Methane on Transition-Metal Catalysts. The Journal of Physical Chemistry Letters 2012, 3 (2), 251–258. https://doi.org/10.1021/jz201461p.

(41) Zhu, W.; Zhang, Y.-J.; Zhang, H.; Lv, H.; Li, Q.; Michalsky, R.; Peterson, A. A.; Sun, S. Active and Selective Conversion of CO2 to CO on Ultrathin Au Nanowires. Journal of the American Chemical Society 2014, 136 (46), 16132–16135. https://doi.org/10.1021/ja5095099.

(42) Fortunelli, A.; Goddard III, W. A.; Sementa, L.; Barcaro, G.; Negreiros, F. R.; Jaramillo-Botero, A. The Atomistic Origin of the Extraordinary Oxygen Reduction Activity of Pt3Ni7 Fuel Cell Catalysts. Chemical Science 2015, 6 (7), 3915–3925. https://doi.org/10.1039/C5SC00840A.

Chapter IV

IDENTIFICATION OF THE SELECTIVE SITES FOR ELECTROCHEMICAL REDUCTION OF CO TO C2+ PRODUCTS ON COPPER NANOPARTICLES

ABSTRACT

Recent experiments have shown that CO reduction on oxide derived Cu nanoparticles (NP) are highly selective toward C2+ products. However, understanding of the active sites on such NPs is limited, because the NPs have ~200 000 atoms with more than 10 000 surface sites, far too many for direct quantum mechanical calculations and experimental identifications. We show here how to overcome the computational limitation by combining multiple levels of theoretical computations with machine learning. This approach allows us to map the machine learned CO adsorption energies on the surface of the copper nanoparticle to construct the active site visualization (ASV). Furthermore, we identify the structural criteria for optimizing selective reduction by predicting the reaction energies of the potential determining step, ΔE_{OCCOH}, for the C2+ product. Based on this structural criterion, we design a new periodic copper structure for CO reduction with a theoretical faradaic efficiency of 97%.

4.1 INTRODUCTION

Rapid progress is being made in developing new catalysts that are highly active and selective to electrochemically reduce CO or CO2 to specific chemical fuels and feedstocks[1-2]. Improved selectivity and activity in reducing CO2 and CO to valuable hydrocarbons and alcohols will enable the conversion of intermittent or remote renewable energies into complex chemical forms for storage and delivery[3]. At the same time, using sequestrated CO2 as the feedstock would reduce the amount of excess atmospheric CO2 by completing the carbon cycle with carbon fixation via artificial photosynthesis or other forms of renewable energy sources[4-5].

However, CO_2 is quite stable, making it very challenging to optimize catalytic efficiency due to the difficulty in activating CO_2[6]. After decades of development, copper remains the only catalyst that can reduce CO or CO_2 by more than two electrons to generate valuable products in nontrivial amounts. Recently, oxide derived copper nanoparticles (NP) have been shown to greatly improve both the activity and selectivity of CO and CO_2 reduction towards C2+ products[7]. Based on early temperature programmed desorption (TPD) experiments, the improved performance of the oxide derived metal NP was hypothesized to arise from strong CO adsorption sites[8]. However, later experiments have found that selectivity correlated linearly with the grain boundary (GB) density[9-10]. In this work, we focus on elucidating which local Cu structures lead to the optimum properties for CO reduction to C2+ products.

4.2 RESULTS AND DISCUSSION

4.2.1 CO Adsorption

We previously used Density functional theory (DFT) with full solvent and Grand Canonical techniques to determine the reaction mechanisms for CO reduction to C1 and C2 products on Cu (100) and Cu (111) surfaces, leading to an excellent agreement with experiments (over potentials within 0.05 V)[11-12]. However, the experimental 10nm NP involves ~200,000 atoms with ~10,000 possible surface sites, well beyond the capabilities of DFT. To circumvent the limitation of the direct application of DFT, we subsequently utilized the reactive force field (ReaxFF)[13-14] to computationally grow the 10nm nanoparticles and then used DFT to sample only 84 surface sites for ΔE_{CO} and 4 surface sites for ΔE_{OCCOH}[15-16]. In order to extract a quantitative understanding of the variations of the chemistry over the whole nanoparticle, we propose here a methodology to combine limited numbers of DFT calculations with machine learning to train a machine learning model that accurately predicts the binding energies for all sites.
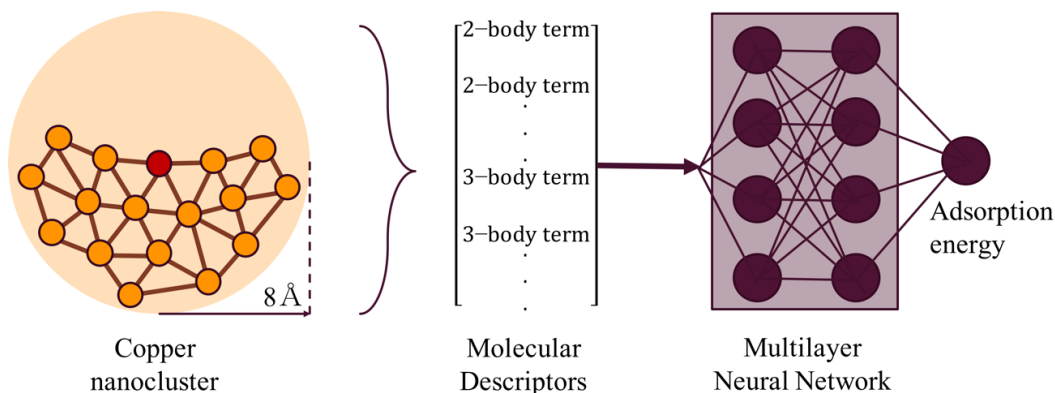
Figure 4-1. Schematics of the machine learning model. For each surface site (red), we extract a copper cluster including all the atoms within $8\,\text{Å}$ from a copper NP. The adsorption energy is calculated using DFT and is used as the target property for training. We use Behler-Parrinello[17] type neural network model. In this study, we describe the copper cluster by a set of 2-body and 3-body molecular descriptors about the surface atom. We then used these descriptors as input to a multilayer neural network for fitting.

First, we used ReaxFF to computationally synthesize a 10 nm copper nanoparticle (NP) that closely resembles the experimental NP [*C1.1 in SI*]. The predicted structure leads to XRD spectra and TEM images that match those of the experimental NP structures. Next, we selected 400 random surface sites and calculated their CO adsorption energies using DFT *[C1.2 in SI]*. We previously found that including atoms up to $8\,\text{Å}$ from the surface site is sufficient to represent the local environment[15]. We integrated this local environment into a neural network in which the surrounding atoms are transformed into 12 two-body and 18 three-body molecular descriptors as inputs to a 2-layer neural network with 50 nodes in each layer, as shown in Figure 4-1. Further details of the descriptor definition are in Section C1.3 of the Supporting Information. We partitioned the 400 surface sites into training set, validation set, and test set with an 8:1:1 ratio. Here the validation set is used to terminate the training sufficiently early to avoid overfitting. Section C2 of the Supporting Information shows that the root mean squared error (RMSE) of the CO binding energy (ΔECO) on the training set is 0.111eV while for the validation set RMSE= 0.117eV, and for the test set RMSE= 0.123eV. We refer to this as the ReaxQM-Machine Learning

strategy, or RxQM-ML. This is much lower than the RMSE=0.2eV for a similar study of the crystalline surface of the NiGa binary alloy.[18]

After training this accurate neural network model, we used RxQM-ML to predict the CO adsorption energies for all 10,000 surface sites. The statistical distribution of the CO adsorption energies is shown in Figure 4-2(a). Overall, the CO adsorptions range from -0.55 to -1.43 eV, showing the wide variety of surface sites on the copper NP. As expected, most energies are clustered around the values for such low index surfaces, as (111), (100), and (211)15. However, we find a significant number of surface sites with much stronger CO adsorption energies. This is shown by the distribution to the left of the (211) line. These results are consistent with the TPD experiments, which show a broad peak centered at 275K only for the copper NP, indicating that ~7-15% of the surface leads to stronger CO adsorptions than low index copper surfaces[8].

Furthermore, the low-cost of RxQM-ML model makes it possible to establish the quantitative structure-activity relationship (QSAR) such that the machine-learned CO adsorption energies can be remapped back to the copper nanoparticle, as shown in Figure 4-2(b). Here, red indicates low ΔECO, white indicates moderate ΔECO, and blue indicates unfavorable ΔECO. The (100), (111), and (110) surfaces are all colored light blue, indicating that they are near the mean values of the adsorption energy distributions as in Figure 4-2(a). The sites in solid blue are not fully exposed, making them difficult for CO to bind. The sites in red are of most interest because they correspond to more favorable adsorptions of CO than the low-index surfaces. As shown in light red in the figure, the moderately strong CO adsorption sites are typically along the step edges, and as shown in solid red, the strong CO adsorption sites are mostly isolated surface sites or kink sites.

The ASV in Figure 4-2 shows clearly that favorable CO adsorption sites are scattered across the whole nanoparticle surface. This is consistent with experimental observations that the surface areas corresponding to GBs are not sufficiently large to account for the number of strong CO adsorption sites[8]. Using RxQM-ML, we now can directly show that the strong CO adsorption energies are not just at GBs.
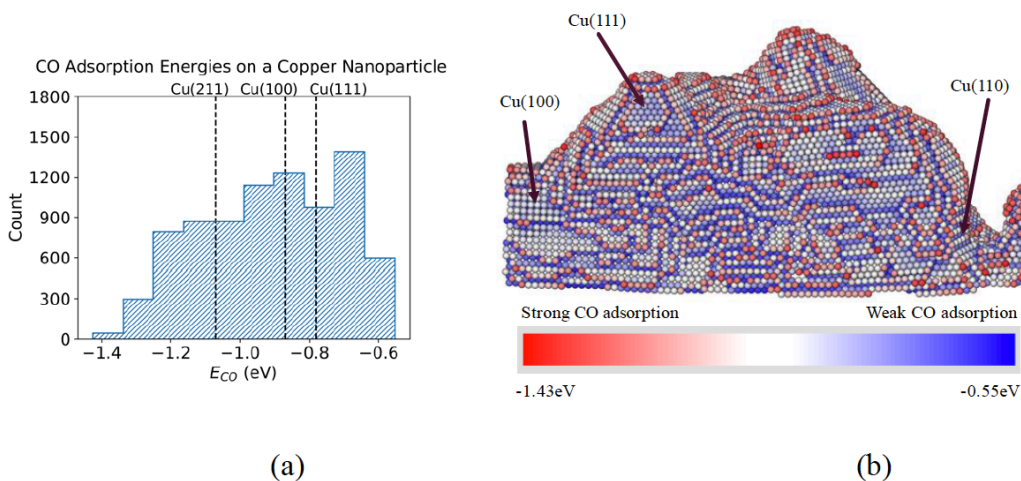
Figure 4-2. CO Binding Energy Analysis. (a) Distribution of CO binding energies (ΔECO) on the 10nm copper nanoparticle. The three vertical dashed lines correspond to the CO adsorption energies of single crystal surfaces of (211), (100) and (111)[15]. (b) Active site visualization (ASV) of the predicted CO adsorption energies on the nanoparticle. As indicated by the colored bar, the red sites correspond to strong CO adsorption, the white sites correspond to moderate CO adsorption, and the blue sites correspond to weak CO adsorption. The common surfaces of (100), (111), and (110) are indicated in the figure.

4.2.2 From CO to C2 Products

Although we have demonstrated that the CO binding energy is not necessary to correlate with GBs, there is a great deal of experimental evidence suggesting that increasing the GB density can significantly improve the C2+ selectivity. Another descriptor is needed to describe selectivity of these nanoparticles. As shown experimentally[19] and theoretically[20-22], the selective step towards C2+ products involves C-C coupling in which *OCCOH is formed. Thus, the most plausible descriptor is the reaction energy for forming *OCCOH,

$$\Delta E_{OCCOH} = E[*OCCOH] - E[*CO, *CO] - 0.5 \times E[H_2],$$

which we have shown previously to be the potential determining step for ethanol production. Then, we started with ~180 randomly sampled surface site and calculated the formation energy for *OCCOH, ΔE_{OCCOH}. The distribution is shown in the blue histograms

in Figure 4-3(a). As shown in the figure, the range of ΔE_{OCCOH} spans by more than 1eV, implying that some sites are much more selective than others. We could sample additional sites to develop a similar machine learning model for ΔE_{OCCOH}. However, we examined the sites with the lowest ΔE_{OCCOH}, and found that all of them are involved square sites, similar to those of the (100) surface. To test this hypothesis, we further sampled 100 square sites, leading to the distribution for ΔE_{OCCOH} shown in orange in Figure 4-3(a). Comparing to the random sites on the surface of the copper nanoparticle, we found that the square sites were indeed more favorable, as shown by the shift in the distribution in ΔE_{OCCOH} in Figure 4-3(a).
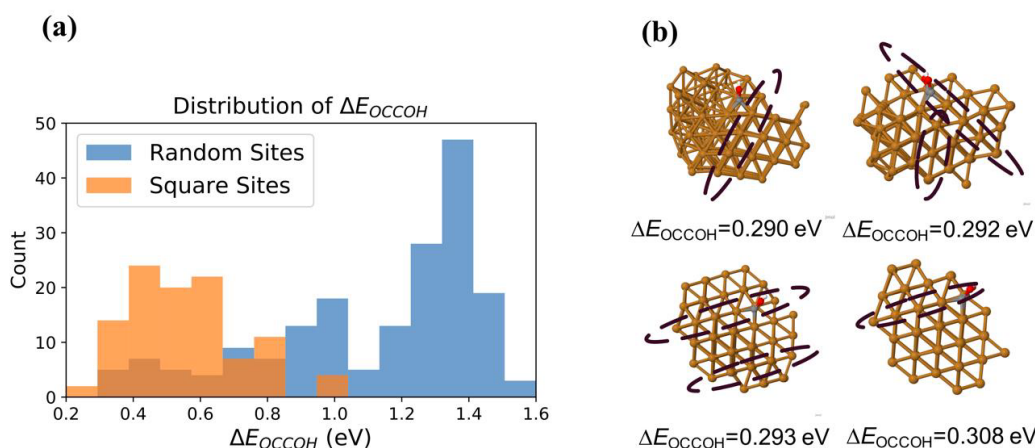
(a)

(b)

ΔE_{OCCOH}=0.290 eV ΔE_{OCCOH}=0.292 eV

ΔE_{OCCOH}=0.293 eV ΔE_{OCCOH}=0.308 eV

Figure 4-3. ΔE_{OCCOH} Analysis. (a) Distributions of ΔE_{OCCOH} on the surface of the copper nanoparticle. Blue: 180 *random* surface sites; orange: 100 random *square* sites. (b) The four squared structures with the lowest ΔE_{OCCOH} sampled randomly from the copper nanoparticle. The dashed ellipses indicate the locations of the twin boundaries.

With the new distribution of just the *square* sites, we extracted the common features of the most selective sites by further examining the square sites with the lowest ΔE_{OCCOH}. We found that a step (111) surface is always next to these favorable square sites, as shown in Figure 4-3(b). These sites are similar to the Cu(S)[n(100) × (111)] edge step sites where the (111) surface and the (100) surface intersect. In fact, experiments[23-24] showed that these step sites have higher selectivity than either the (100) and (111) surface. To confirm this theoretically, we calculated E_{OCCOH} on (100), (111), (311), and (511) surfaces to be

0.44eV, 0.64eV, 0.52eV, and 0.41eV. The calculated trend agrees very well the experimental selectivity trend in which (511) > (100) > (311) > (111) [*Section C3 in SI*]. This comparison with experimental findings on the Cu(S)[n(100) × (111)] surfaces confirms the validity of using EOCCOH as the descriptor for the selectivity towards C2+ products. It is also consistent with our finding from sampling the NP that favorable sites for EOCCOH or C2+ selectivity must involve a (111) step surface next to a (100) site where *OCCOH is formed.

In addition, twin boundaries are associated with the square surface sites having the lowest ΔEOCCOH. Figure 4-3(b) shows that these twin boundaries are all next to the site where *OCCOH is formed. This implies that the selectivity towards C2+ products is directly related to twin boundaries which are a special type of GBs.

Building on the idea that the above common features lead to the best *OCCOH sites, we constructed the smallest periodic structure possessing these features. This is shown in Figure 4-4. We expect that this periodic surface will behave chemically in the same way as these selective sites. Because it is a smallest periodic structure containing these sites, the density of active sites will be much higher than the randomly and sparsely distributed active sites on a nanoparticle.

This minimal periodic structure is shown in Figure 4-4(a). From the ABC stacking of the FCC copper, the smallest grain size must contain at least 6-layer, corresponding to ABCACB stacking, where the A layers are twin boundaries. Since the step surfaces involving the (100) and (111) are of interest, they are shown by double lines and dash lines in the figure.

Based on the configurations of the adsorbed *OCCOH on the copper clusters, there are 4 ways of placing the intermediate on this surface, as shown in Figure 4-4(b). The first two structures, (a) and (b), with the *OCCOH adsorbed in the cross sectional plane show unfavorable energies. Thus, the in-plane *OCCOH adsorption is not responsible for the increased in C2+ selectivity. On the other hand, *OCCOH adsorbed perpendicular to the page (or out-of-plane) are much more favorable, with only 0.41 eV for the convex site and

0.35 eV for the concave site, which is better than all the single crystal surface sites considered here. In fact, the same configuration is also found for the copper nanoparticle. As shown again in Figure 4-3(b), *OCCOH are all adsorbed perpendicular to the page. Thus, we predict that the (100)-like square sites next to a (111)-like step surface and on-top of a twin boundary that binds *OCCOH parallel to the twin boundary will have the most favorable E_{OCCOH}, which corresponds to the most selective sites.

(a):
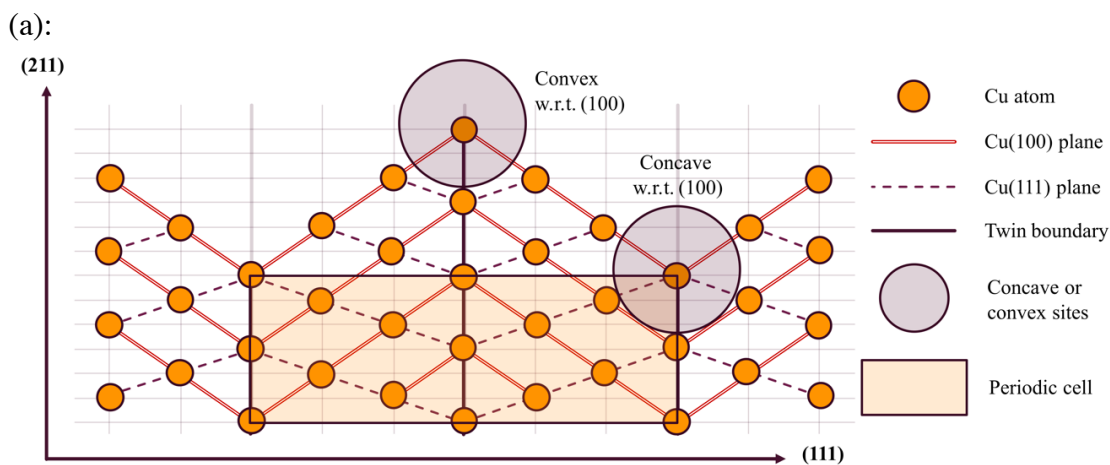
(b):

	Concave	Convex	Structure of the best site
In-plane binding	(a) $\Delta E_{OCCOH} = 0.55$ eV	(b) $\Delta E_{OCCOH} = 0.57$ eV	Side View:
Out-of-plane binding	(c) $\Delta E_{OCCOH} = 0.35$ eV	(d) $\Delta E_{OCCOH} = 0.41$ eV	Top View:

Figure 4-4. Schematic of Designed Structure. (a) The shaded area is the minimal periodic structure of FCC copper containing the (100) planes, (111) planes, and twin boundaries. Terminating this structure to expose the (100) and (111) surfaces leads to sites that are concave or convex with respect to the (100) planes. (b) The four types of sites for adsorbed *OCCOH on the surface of the minimal periodic structure. The structure that is concave with respect to the (100) planes has the most favorable ΔE_{OCCOH} for C2+ selectivity. The top and side views of this structure are shown on the right column of (b). More details on these sites are shown in Section C4 of the supporting information. Note, for structures (c) and (d), the other carbon and oxygen atoms are not shown since they overlap with the foreground atoms in the side view. The full *OCCOH structure for (c) is revealed in the top view, as shown on the right column.

For the most favorable structure, the faradaic efficiency towards C2+ product is predicted to be 97% using experimental data in which the current density for C2+ production increases linearly as the density of GBs, and the current for hydrogen production remains the same[10]. The prediction is shown in Figure 4-5, which also includes a prediction for an experimental copper structure in which a high density of twin boundaries is synthesized[25], assuming that the structure exposes the twin boundaries in the preferable configuration. Details of this prediction are summarized in section C4 of Supporting Information.
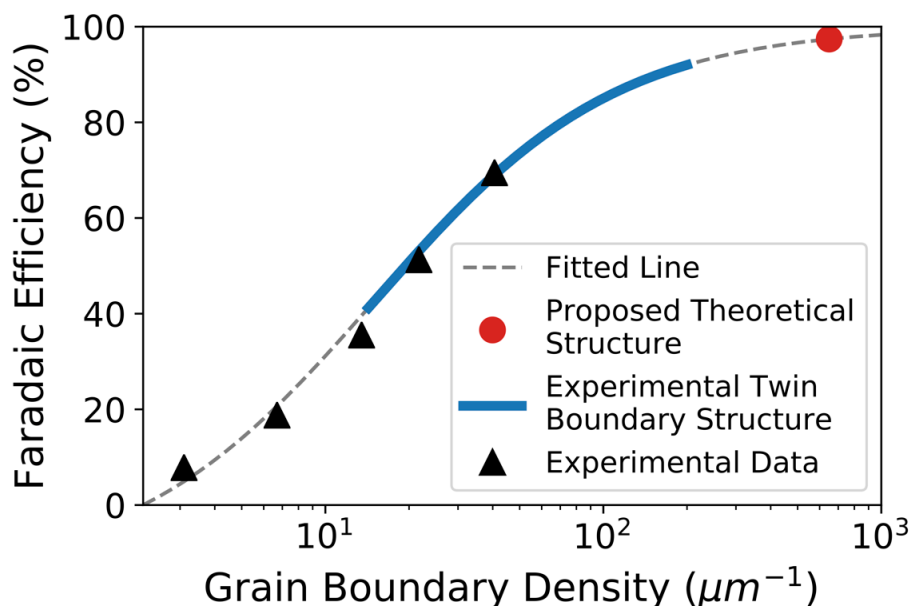
Figure 4-5. Predicted faradaic efficiency (FE) of the concave site on the minimal periodic structure compared to experimental data. An experimental copper structure with abundant twin boundaries[25] is also extrapolated based on the densities of the boundaries.

4.3 CONCLUSION

In conclusion, we used machine learning to fit the structure-activity relationship between the local structures of the copper nanoparticle and the theoretical CO adsorption energies. By extrapolating the energies back to the nanoparticle, we found that strong CO adsorption energies are not just on GBs, implying that CO adsorption energies are not an appropriate descriptor for C2+ selectivity. Rather, we show that ΔEOCCOH, the transition state for forming ethanol of C2+ products in C-C coupling, is the appropriate descriptor. This explains the selectivity on Cu(S)[n(100) × (111)] surfaces and the twin-related step square sites on the nanoparticle. To illustrate how to use this information, we designed the minimal periodic structure. This minimal periodic structure has a super high density of selective sites that we expect will lead to near unity selectivity based on extrapolations of theoretical and experimental data.

ACKNOWLEDGMENT

BIBLIOGRAPHY

(1) Recent Zhang, W.; Hu, Y.; Ma, L.; Zhu, G.; Wang, Y.; Xue, X.; Chen, R.;Yang, S.; Jin, Z. Progress and Perspective of Electrocatalytic CO2 Reduction for Renewable Carbonaceous Fuels and Chemicals. *Adv. Sci.* 2018, *5*(1), 1700275.

(2) Zhao, G.; Huang, X.; Wang, X.; Wang, X. Progress in Catalyst Exploration for Heterogeneous CO2 Reduction and Utilization: A Critical Review. *J. Mater. Chem. A.* 2017, *5*(41), 21625–21649.

(3) Detz, R. J.; Reek, J. N. H.; Van Der Zwaan, B. C. C. The Future of Solar Fuels: When Could They Become Competitive? *Energy Enviro. Sci.* 2018, *11*(7), 1653–1669.

(4) Van Der Giesen, C.; Kleijn, R.; Kramer, G. J. Energy and Climate Impacts of Producing Synthetic Hydrocarbon Fuels from CO2. *Environ. Sci. Technol.* 2014, *48*(12), 7111–7121.

(5) Artz, J.; Müller, T. E.; Thenert, K.; Kleinekorte, J.; Meys, R.; Sternberg, A.; Bardow, A.; Leitner, W. Sustainable Conversion of Carbon Dioxide: An Integrated Review of Catalysis and Life Cycle Assessment. *Chem. Rev.* 2018, *118*(2), 434–504.

(6) Kumar, B.; Llorente, M.; Froehlich, J.; Dang, T.; Sathrum, A.; Kubiak, C. P. Photochemical and Photoelectrochemical Reduction of CO2. *Annu. Rev. Phys. Chem.* 2012, *63*, 541–569.

(7) Li, C. W.; Kanan, M. W. CO2 Reduction at low Overpotential on Cu Electrodes Resulting from the Reduction of Thick Cu2O Films. *J. Am. Chem. Soc.* 2015, *134*(17), 7231-7234.

(8) Verdaguer-Casadevall, A.; Li, C. W.; Johansson, T. P.; Scott, S. B.; McKeown, J. T.; Kumar, M.; Stephens, I. E. L.; Kanan, M. W.; Chorkendorff, I. Probing the Active Surface Sites for CO Reduction on Oxide-Derived Copper Electrocatalysts. *J. Am. Chem. Soc.* 2015, *137*(31), 9808–9811.

(9) Feng, X.; Jiang, K.; Fan, S.; Kanan, M. W. Grain-Boundary-Dependent CO2 Electroreduction Activity. *J. Am. Chem. Soc.* 2015, *137*(14), 4606–4609.

(10) Feng, X.; Jiang, K.; Fan, S.; Kanan, M. W. A Direct Grain-Boundary-Activity Correlation for CO Electroreduction on Cu Nanoparticles. *ACS Cent. Sci.* 2016, *2*(3), 169–174.

(11) Nørskov, J. K.; Bligaard, T.; Rossmeisl, J.; Christensen, C. H. (2009). Towards the Computational Design of Solid Catalysts. *Nature Chemistry*. 2009, *1*(1), 37–46.

(12) Becke, A. D. Perspective: Fifty Years of Density-Functional Theory in Chemical Physics. *J. Che. Phys.* 2014, *140*(18), 18A301.

(13) van Duin, A. C. T.; Dasgupta, S.; Lorant, F.; Goddard, W. A. (2001). ReaxFF: A Reactive Force Field for Hydrocarbons. *J. Phys. Chem. A*. 2001, *105*(41),

(14) Chenoweth, K.; van Duin, A. C. T.; Goddard, W. A. ReaxFF Reactive Force Field for Molecular Dynamics Simulations of Hydrocarbon Oxidation. *J. Phys. Chem. A*. 2008, *112*(5), 1040–1053.

(15) Cheng, T.; Xiao, H.; Goddard, W. A. Nature of the Active Sites for CO Reduction on Copper Nanoparticles; Suggestions for Optimizing Performance. *J. Am. Chem. Soc.* 2017, *139*(34), 11642–11645.

(16) Cheng, T.; Huang, Y.; Xiao, H.; Goddard, W. A. Predicted Structures of the Active Sites Responsible for the Improved Reduction of Carbon Dioxide by Gold Nanoparticles. *J. Phys. Chem. Lett.* 2017, *8*(14), 3317–3320.

(17) Behler, J.; Parrinello, M. Generalized Neural-Network Representation of High-Dimensional Potential-Energy Surfaces. *Phys. Rev. Lett.* 2007, *98*(14), 1–4.

(18) Ulissi, Z. W.; Tang, M. T.; Xiao, J.; Liu, X., Torelli, D. A.; Karamad, M.; Cummins, K.; Hahn, C.; Lewis, N. S.; Jaramillo, T. F.; Chan, K.; Nørskov, J. K. Machine-Learning Methods Enable Exhaustive Searches for Active Bimetallic Facets and Reveal Active Site Motifs for CO2 Reduction. *ACS Catal.* 2017, *7*(10), 6600–6608.

(19) Pérez-Gallent, E.; Figueiredo, M. C.; Calle-Vallejo, F.; Koper, M. T. M.

Spectroscopic Observation of a Hydrogenated CO Dimer Intermediate During CO Reduction on Cu(100) Electrodes. *Angew. Chem. Int. Ed.* 2017, *56*(13), 3621–3624.

(20) Calle-Vallejo, F.; Koper, M. T. M. Theoretical Considerations on the Electroreduction of CO to C2 Species on Cu(100) Electrodes. *Angew. Chem. Int. Ed.* 2013, *125*(28), 7423–7426.

(21) Cheng, T.; Xiao, H.; Goddard, W. A. Full Atomistic Reaction Mechanism with Kinetics for CO Reduction on Cu(100) from ab initio Molecular Dynamics Free-Energy Calculations at 298 K. *Proc. Natl.Acad. Sci.* 2017, *114*(8), 1795-1800.

(22) Xiao, H.; Cheng, T.; Goddard, W. A. Atomistic Mechanisms Underlying Selectivities in C1 and C2 Products from Electrochemical Reduction of CO on Cu(111). *J. Am. Chem. Soc.* 2017, *139*(1), 130–136.

(23) Hori, Y.; Takahashi, I.; Koga, O.; Hoshi, N. Selective Formation of C2 Compounds from Electrochemical Reduction of CO2 at A Series of Copper Single Crystal Electrodes. *J. Phys. Chem. B.* 2002, *106*(1), 15–17.

(24) Kim, Y. G.; Javier, A.; Baricuatro, J. H.; Torelli, D.; Cummins, K. D.; Tsang C. F.; Hemminger, J. C.; Soriaga, M. P. Surface Reconstruction of Pure-Cu Single-Crystal Electrodes under CO-Reduction Potentials in Alkaline Solutions: A Study by Seriatim ECSTM-DEMS. *Journal of Electroanalytical Chemistry.* 2017, *793*, 113–118.

(25) Morris Wang, Y.; Sansoz, F.; Lagrange, T.; Ott, R. T.; Marian, J.; Barbee, T. W.; Hamza, A. V. Defective Twin Boundaries in Nanotwinned Metals. *Nature Materials.* 2013, *12*(8), 697–702.

A p p e n d i x   A

SUPPORTING INFORMATION FOR CHAPTER II

A1. J-PtNW Synthesis using ReaxFF Reactive Molecular Dynamics

We used ReaxFF reactive molecular dynamics, to simulate the formation of dealloyed NiPt nanowire, J-PtNW. We mimicked the process of de-alloying in electrochemical condition by removing Ni atoms from initial FCC nanostructure, followed by local relaxation and equilibration. A similar approach was used in our previous work simulating Ni de-alloying of Pt_3Ni_7 nanoparticles[1].

1) First, we built an infinite 1D NW from the FCC Pt crystal structures, placing the z axis of the NW along the (111) direction, and 13 Pt atoms along the x axis and 9 Pt atoms along the y axis. The periodic system is then made by replicating 220 individual unit cells along the axis of the NW. To ensure the Ni composition is consistent with experiment, we randomly replaced 85% of the Pt atoms with Ni atoms and minimized the structure;

2) Then, we erased all the Ni atoms and performed a fixed-cell conjugate-gradient local relaxation using the ReaxFF force field. The convergence threshold criteria are 4×10^{-6} eV on the energy and 4×10^{-8} eV /Å on the gradient. A second local relaxation was performed to equilibrate the cell dimensions in the chain direction at a pressure of 1 atm. The 500 ps NPT MD simulation was carried out at 343 K, followed by 20 ps equilibration;

3) Then we removed the least coordinated Pt atoms expected to be further leached away during ORR cycling, and performed an additional NPT Molecular Dynamics (MD) simulation for 520 ns (500 ps NPT at 343 K, followed by 20 ps equilibration) to re-equilibrate the system;

4) Finally, another round of local relaxation was performed to obtain the final structure.

The ReaxFF parameters we used in this work to describe the interactions in Pt clusters were fitted to reproduce DFT-derived structural and energetic quantities: the equation-of-state for various bulk structures (FCC, BCC, SC, and A-15), the stability of various surface

orientations, as well as finite Pt clusters (up to 35 atoms), with more details listed in the previous work[2]. And the full set of ReaxFF parameters are available in the Supporting Information of the referenced work[2].

The structural comparisons with experiments was illustrated in Figure 3 and Figure S11 of the supplementary material in our previous work[3], showing the final predicted structures consistent with the experimental structure and stable under electrochemical conditions.

The J-PtNW has a total number of 7165 Pt atoms per periodic unit cell. Since we need to extract the bridge nanocluster for DFT calculations, the Pt atoms close to the NW cell boundary were not considered. We considered various cutoffs and found that Rcut-off = 8 Å, led to convergence. The final J-PtNW investigated in this work has a total number of 6926 Pt atoms, obtained by excluding the Pt atoms within 8 Å from the NW cell boundaries.

A2. Surface Vector Based Methodology for Surface Extraction

Here we extracted Pt surface from Jagged Platinum Nanowires (J-PtNW) using a surface vector based methodology. Similar approach has been used in our earlier works for Copper and Gold Nanoparticles[4,5]. The procedure is shown in Figure A-1 and can be illustrated as following:

i) Cut a sphere of 8 Å radius around selected Pt atom (cPt) from the whole nanowire;

ii) Sum up all cPt-rPt vectors pointing from the center atom (cPt) to other atoms (rPt) in the nanocluster. Take the negative norm of this summed vector as surface vector;

iii) If all the angles between cPt-rPt vectors and surface vector are smaller than the given cut-off angle, the selected atom is defined as a surface atom, else a bulk atom. The angle cut-off is optimized to 30° in our system.

A3. Benchmark Calculations for Bridge Nanocluster Model

We showed in Figure A-4 the benchmark calculations toward bridge nanocluster model parameter, R. We randomly selected a nanocluster cut from the J-PtNW, and calculated the adsorption energy of the reactants (H2O and O) and products (OH and OH) of O_{ads} hydration. With the largest cut-off radius at 13 Å, our results showed that 8.0 Å is already sufficient to provide the accuracy of adsorption energy at 0.02 eV. Therefore, we consider

that 8.0 Å provides the best balance of accuracy and efficiency and used this cut-off throughout this work. The calculation details are illustrated in A4 of Supporting Information.

A4. DFT Calculations using VASP

We used VASP package[6] for density functional theory (DFT) calculations, using the PBE functional including the D3 London Dispersion correction with the projector augmented wave (PAW) method[7]. We used the Methfessel-Paxton smearing of second order with the width of 0.2 eV. We took the bridge nanocluster from Pt (111) surface for the benchmark of kinetic energy cut-off and found 400 eV provides an accuracy of 0.01 eV in the adsorption energy and 0.01 Å in d-OO (Table A-1). Thus, we set the kinetic energy cut-off to 400 eV. Calculations including spin –polarization were performed for three bridge nanoclusters, Pt (111) and two randomly selected from J-PtNW. The results are compared to those without spin-polarization in Table A-2. The consistence of the results ensures our systems are nonmagnetic systems. Therefore, the calculations in this work do not include spin-polarization. All geometries were optimized until the force converged to 10^{-2} eV/Å, and the convergence criterion are 10^{-5} eV differences for electronic energy. For cluster calculations, a 22 Å box is used and all Pt atoms are fixed. The benchmark calculations toward the choice of box size are shown in Table A-3. We only considered gamma point in these calculations.

We showed in Figure A-5 and A-6 the comparison of d-OO with and without solvation. As we could see, solvation affects d-OO in a non-negligible manner, especially for the structures showing larger d-OO in range [2.70 Å, 3.50 Å]. Therefore, all our calculations in this work include solvation effect using the VASPsol implicit solvation model[8].

A5. Transition State Search and Free Energy Barrier Calculation

We used the climbing image nudged elastic band (NEB) method in the VASP-VTST code[9] for the transition state (TS) search. We first optimized the initial and final states geometries, then we inserted eight intermediate images along the reaction path and carried out search by constrained optimization. A climbing-image calculation was performed to get to the real saddle point. Then, Dimer[10,11] calculations were performed to further search the conformations around the saddle point. Finally, we verified the vibrational frequency of the transition state generated by the climbing NEB method, showing a single negative curvature

in the Hessian. The solvation effect is included with implicit solvation using VASPsol tool. The free energy barriers (G_a) for the O_{ads} hydration at room temperature (298.15 K) are then obtained by adding to the DFT electronic energy (E), the zero-point energy (ZPE), enthalpy and entropy contribution from vibrational modes of surface species.
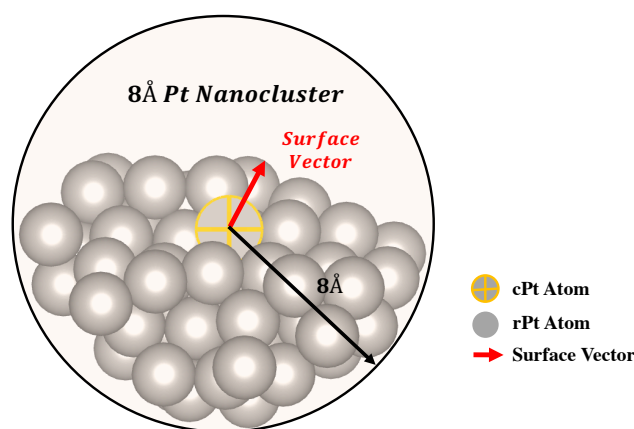

Figure A-1. Surface Extraction using Surface Vector Based Methodology. The angle threshold is optimized to 30° here. cPt Atom: selected center Pt atom; rPt Atom: other atoms in the nanocluster; red vector: surface vector.
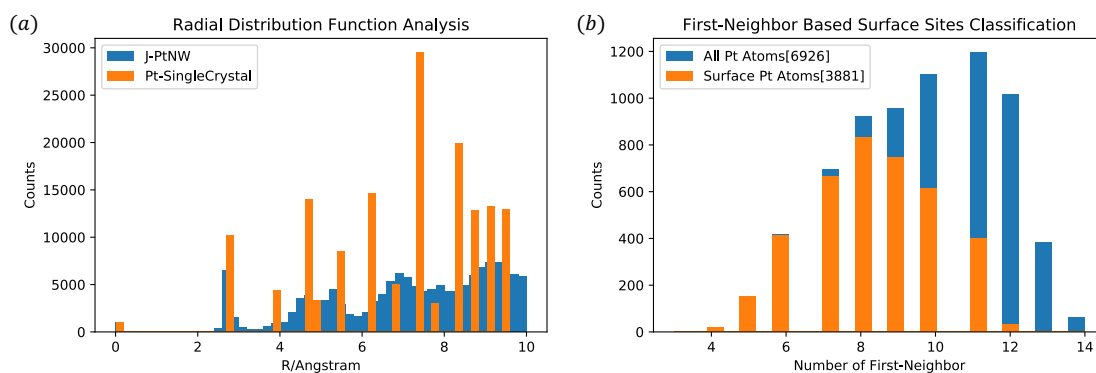
Figure A-2. (a) Pt-Pt radial distribution function (RDF) for J-PtNW. The RDF of Pt single crystal is also plotted for better comparison. As we could see, J-PtNW show broader peaks with the first peak located very close to Pt single crystal; (b) Surface sites classification based on number of first-neighbors. Here the cut-off of first-neighbor is chosen at 3.50 Å based on the RDF of J-PtNW. We could see there are many under-coordinated and over-coordinated sites both on the surface and in the bulk, indicating that the J-PtNW is extremely disordered and irregular.
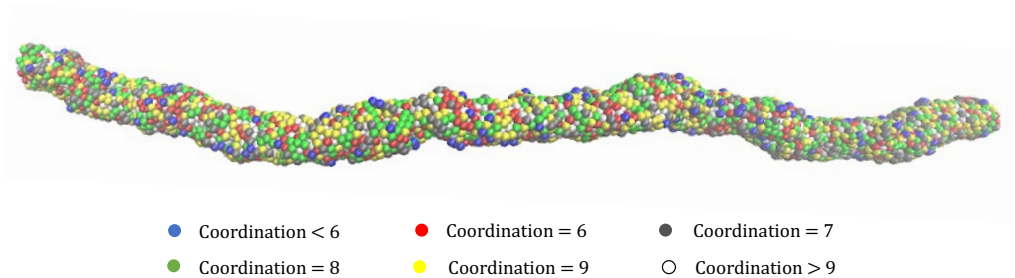
Coordination < 6   Coordination = 6   Coordination = 7
Coordination = 8   Coordination = 9   Coordination > 9

Figure A-3. Surface Sites Visualization by Coordination. We colored all surface sites by their number of first-neighbor (coordination). The surface is extremely disordered and irregular with the coordination raging from 3 (under-coordinated) to 12 (over-coordinated).
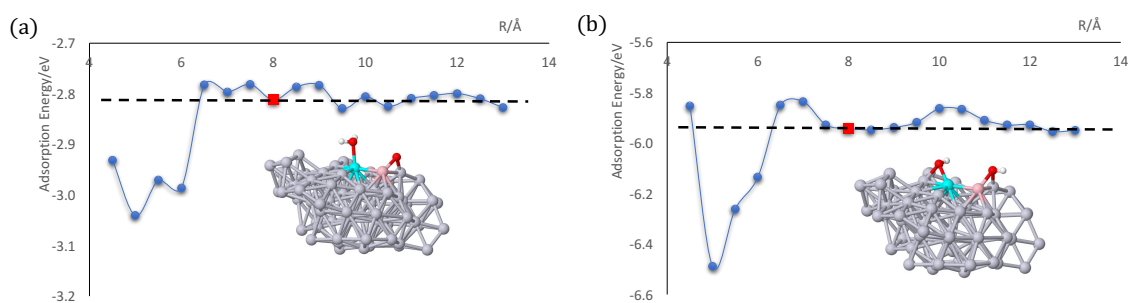

Figure A-4. Benchmark Calculations for Bridge Nanocluster Model Parameter, R. (a) The adsorption energy convergence benchmark as a function of cut-off radius for reactants, $H2O$ and O; (b) The adsorption energy convergence benchmark as a function of cut-off radius for products, OH and OH. As we could see, for both reactants and products, the adsorption energy already converged at 8 Å (marked as red rectangular). Therefore, we consider 8 Å gives the best balance between efficiency and accuracy and we used it throughout this work.

Table A-1. Benchmark calculations for the choice of kinetic energy cut-off. The bridge nanocluster from Pt (111) surfaces with $H2O_{ads}$ and O_{ads} is used to calculate the d-OO and adsorption energy with different kinetic energy cut-off. We found the kinetic energy cut-off at 400 eV already gave the accuracy of d-OO at 0.01 Å and adsorption energy at 0.01 eV. Therefore, we used 400 eV as the kinetic energy cut-off for all the calculation presented in this work. Here, d-OO is defined as the distance between the O of H_2O_{ads} and the O_{ads}, and adsorption energy is defined as $E_{ads} = E_{*H2O+O} - E_* - E_{H2O} - 0.5*E_{O2}$.

Kinetic Energy Cut-off (eV)	400	450	500	550	600
d-OO (Å)	3.15	3.15	3.14	3.15	3.15
Adsorption Energy (eV)	-2.03	-2.01	-2.01	-2.02	-2.02

Table A-2. Benchmark calculations for the choice of spin-polarization. We performed calculations including spin polarization for three bridge nanoclusters, Pt (111) and two randomly chosen from J-PtNW. The results are compared to those without spin-polarization. The consistence of the results shows our systems are nonmagnetic systems. Thus, all the calculations presented in this work don't include spin-polarization. d-OO and adsorption energy are defined in the same way as in Table A-1.
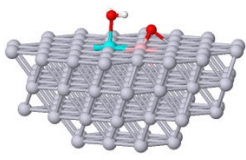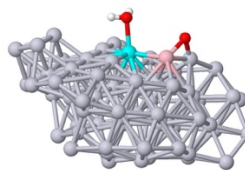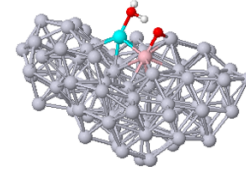
	Pt (111)		Bridge Nanocluster 1		Bridge Nanocluster 2	
Spin Polarization	Yes	No	Yes	No	Yes	No
d-OO (Å)	3.16	3.15	4.03	4.03	2.49	2.49
Adsorption Energy (eV)	-2.02	-2.03	-2.81	-2.81	-2.82	-2.82
Structure						

Table A-3. Benchmark calculations for the choice of simulation box size. We put Pt (111) and Bridge Nanocluster 1 in the cubic simulation box of different size and found 22 Å already reached the convergence of both d-OO and adsorption energy. Therefore, all the calculations presented in this work used the cubic simulation box of size 22 Å. Here, d-OO and adsorption energy are defined in the same way as in Table A-1 and A-2. And Pt (111) and Bridge Nanocluster 1 are the same as in Table A-2.

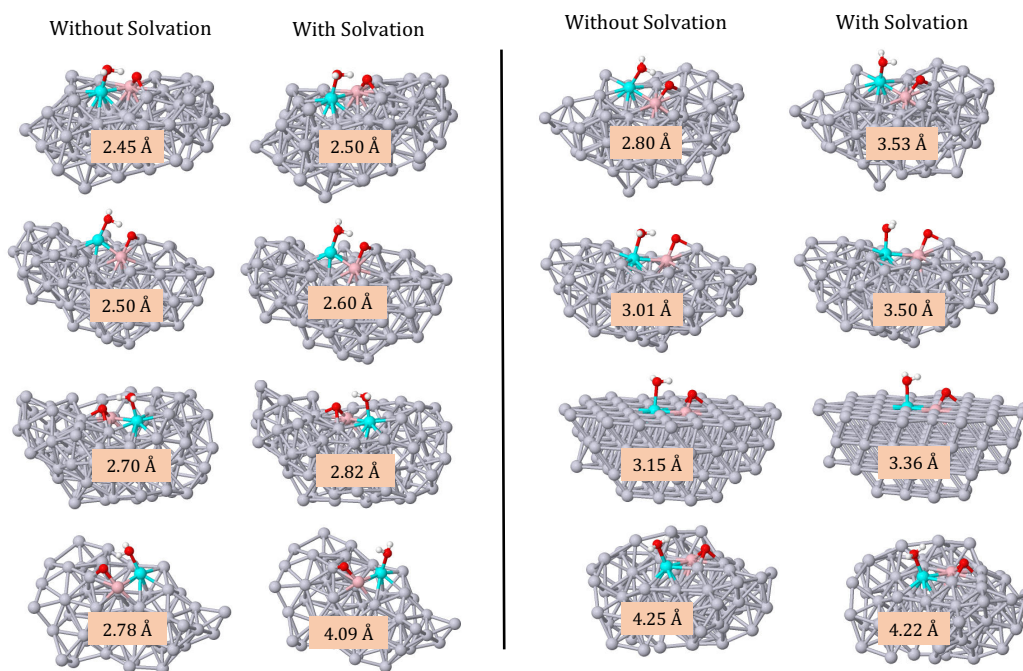| Box Size a/ Å	Pt (111)		Bridge Nanocluster 1	
	d-OO (Å)	Adsorption Energy (eV)	d-OO (Å)	Adsorption Energy (eV)
22	3.15	-2.03	4.03	-2.82
23	3.15	-2.02	4.03	-2.81
24	3.15	-2.03	4.03	-2.81
25	3.15	-2.03	4.03	-2.81
26	3.15	-2.03	4.03	-2.81
27	3.15	-2.02	4.03	-2.81
28	3.15	-2.03	4.03	-2.81
29	3.15	-2.03	4.03	-2.81

Figure A-5. Solvation effect on d-OO. We showed here eight examples about how solvation affects d-OO. Here, d-OO defined in the same way as above and is marked in figure as well. The d-OO for Pt (111) is 3.15 Å without solvation and 3.36 Å with solvation. We could conclude here that solvation effect cannot be ignored. Therefore, all our calculations in this work include solvation effect by using the VASPsol implicit solvation model.
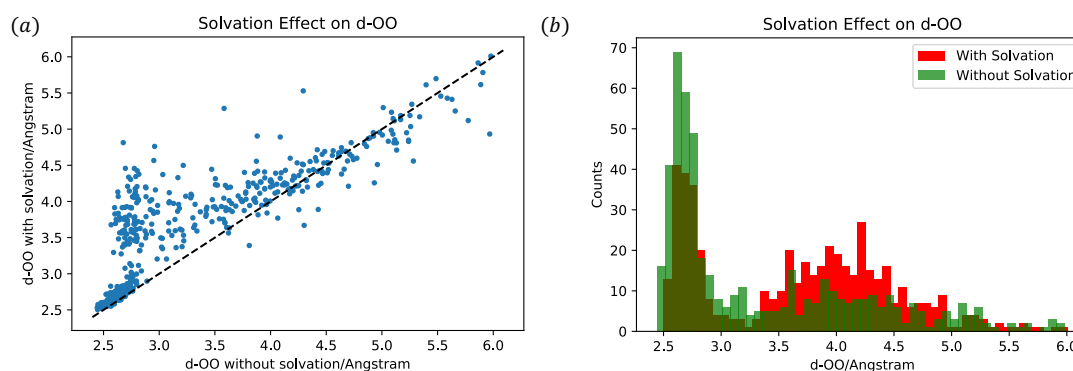

Figure A-6. Solvation effect on d-OO. We compared d-OO of all sampled 500 nanoclusters with and without solvation. Here, d-OO defined in the same way as above. As shown in above plot, we could conclude here that solvation effect cannot be ignored, especially for the

larger d-OO in range [2.70 Å, 3.50 Å]. Therefore, all our calculations in this work include solvation effect by using the VASPsol implicit solvation model.
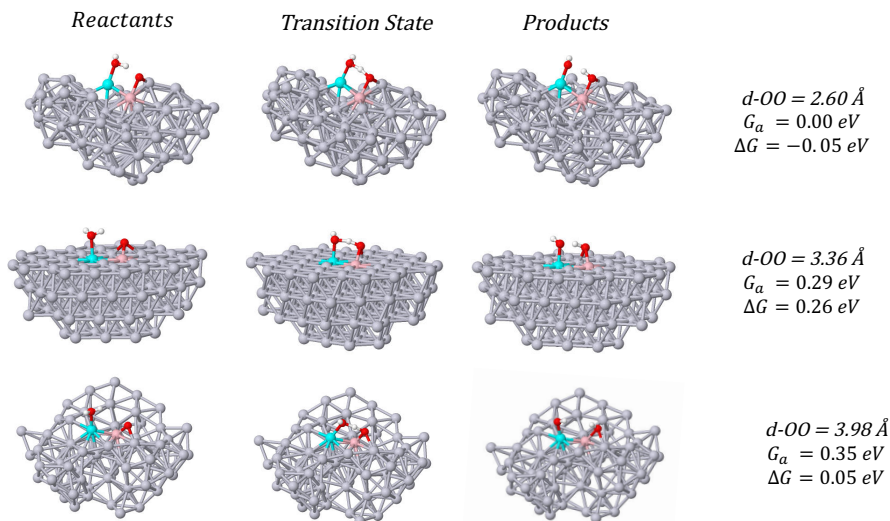
Reactants   Transition State   Products

$d\text{-}OO = 2.60\ \text{Å}$
$G_a\ = 0.00\ eV$
$\Delta G = -0.05\ eV$

$d\text{-}OO = 3.36\ \text{Å}$
$G_a\ = 0.29\ eV$
$\Delta G = 0.26\ eV$

$d\text{-}OO = 3.98\ \text{Å}$
$G_a\ = 0.35\ eV$
$\Delta G = 0.05\ eV$

Figure A-7. d-OO and Free Energy Barrier (G_a). We showed here three examples with Pt (111) as reference case. We found the nanocluster with shorter d-OO showing lower G_a, while ΔG doesn't correlate with the free energy barrier. Thus, we choose d-OO as our physical descriptor for performance evaluation throughout this work. The free energy barrier is defined by: $G_a = G_{TS} - G_{Reactants}$, and the thermodynamic reaction energy is defined by: $\Delta G = G_{Products} - G_{Reactants}$
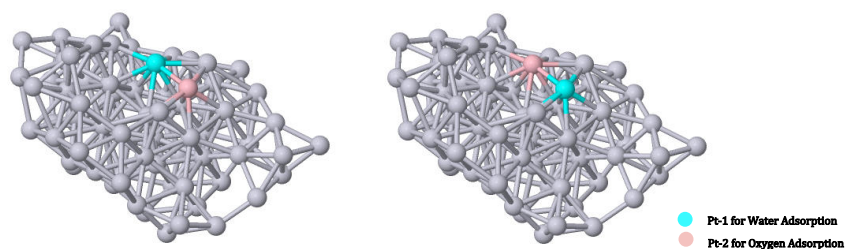
● Pt-1 for Water Adsorption
● Pt-2 for Oxygen Adsorption

Figure A-8. Same nanocluster with Pt-1 and Pt-2 swapping labels. Using the iteration procedure, we might generate the same nanocluster twice, but they are considered to be different in our definition because when binding $H2O$ or O, Pt-1 and Pt-2 are not identical anymore.
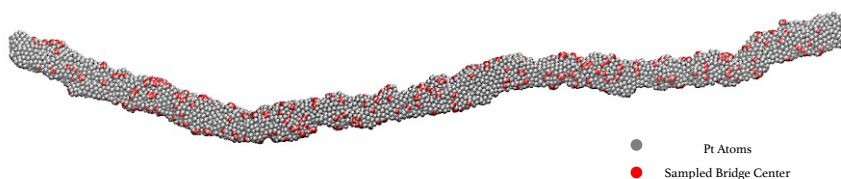
Figure A-9. Plotting Sampled Bridge Center Back on J-PtNW. We plotted back the center of sampled 500 bridge pairs on J-PtNW (shown as red). As we could see, bridge centers are distributed throughout all nanowires, indicating that our sample is a good representation of the whole J-PtNW.
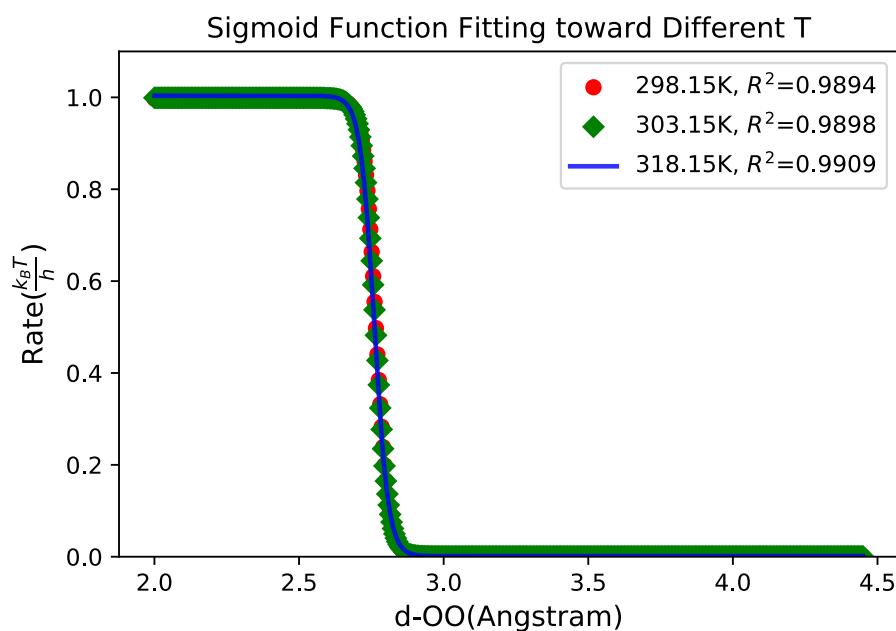

Figure A-10. We calculated the free energy barriers at different temperature, and refitted the sigmoid function, $k(d\text{-}OO|T) = L/(1 + exp(A \times (d\text{-}OO - x_0))) + b$. The curves at different temperature (298.15 K, 303.15 K and 318.15 K) are showed above, all with high R^2.
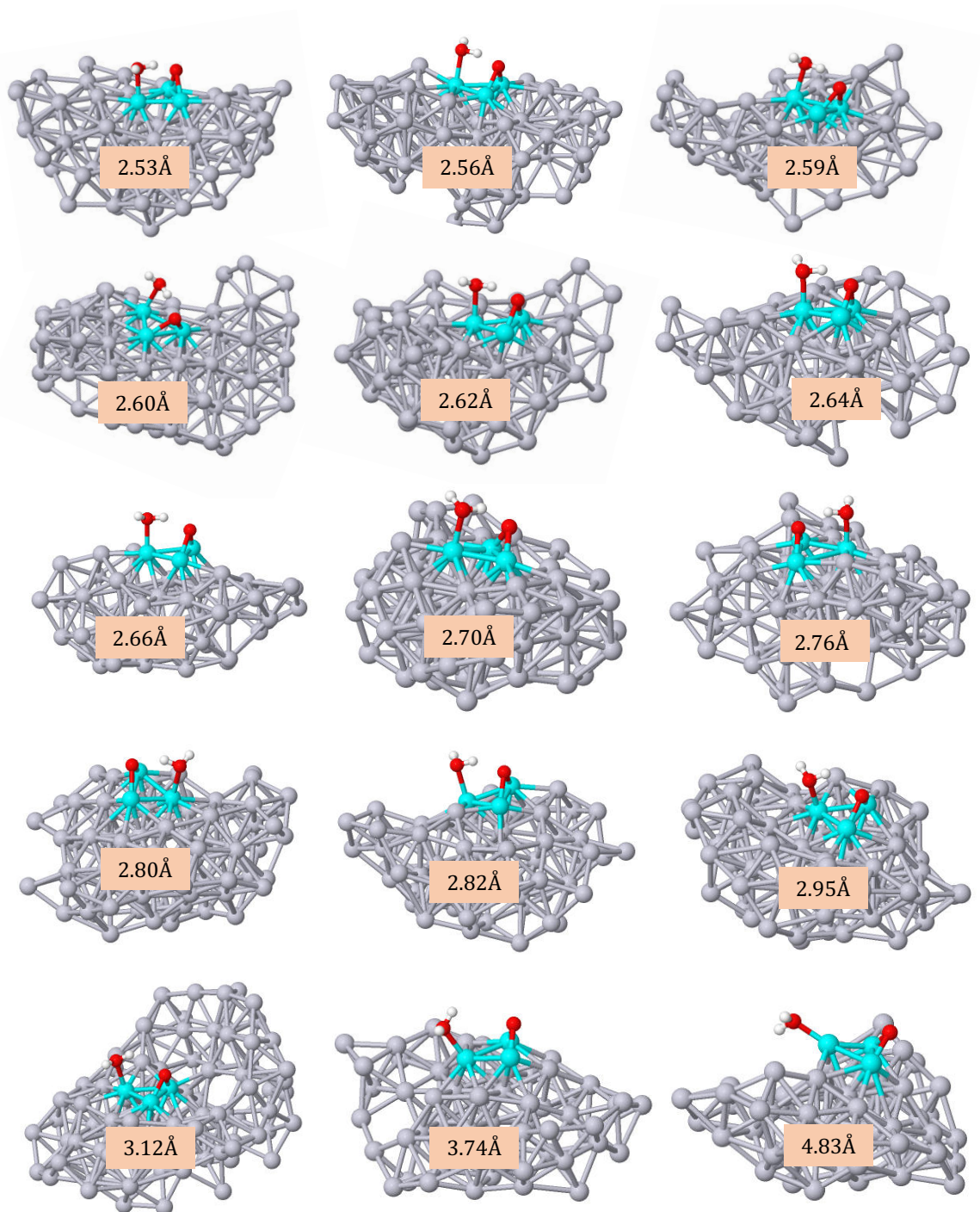
Figure A-11. 15 Representative Structures of Triangle Group with different d-OO.
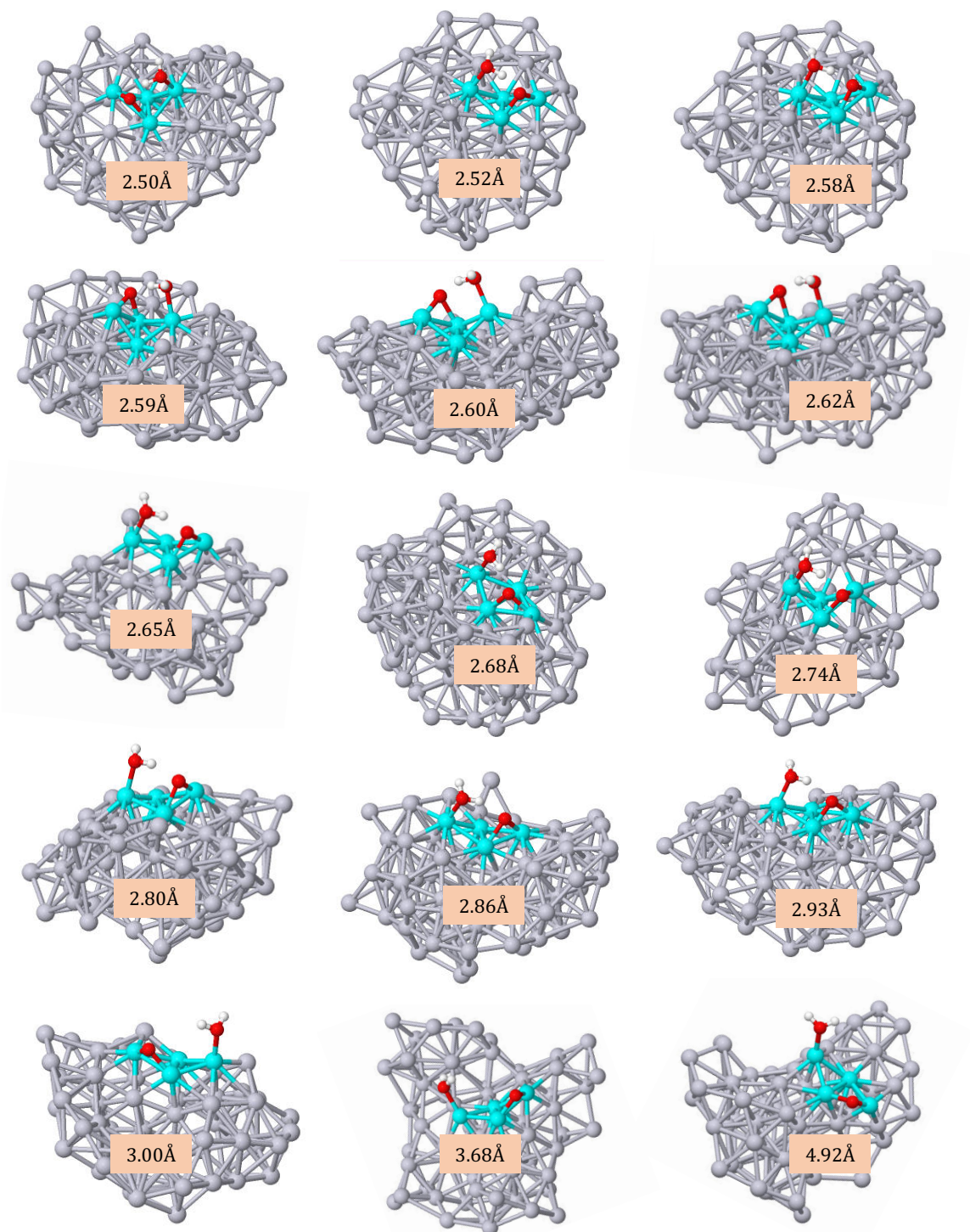
Figure A-12. 15 Representative Structures of Concave-Up Rhombus Group (dihedral > 30°) with different d-OO.

Free Energy Barrier vs Pt-Pt Bond Length

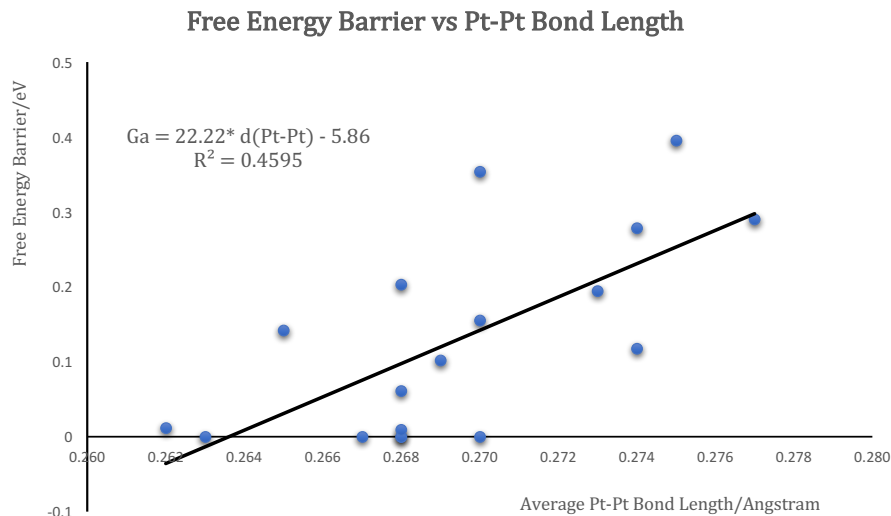$Ga = 22.22 \cdot d(Pt-Pt) - 5.86$
$R^2 = 0.4595$

Figure A-13. Correlation between strain and free energy barrier. To correlate the mechanical strain with catalytic activity, we plotted the G_a toward strains of the selected 18 structures from *Section 2.2.5.* We used the average Pt-Pt bond length around the adsorption sites to represent the strain. Here for Triangle structures, we took the average bond length of the three Pt atoms forming the triangle. And for Concave-Up Rhombi, we took the average bond length of the four rhombi vertices. And for others, we took the average bond length of Pt atoms which are directly interacting with H2O and O. In general, there is a linear correlation between the catalytic activity and strain. The sites with compressive strains show lower energy barriers and sites with tensile strain show higher energy barriers. The correlation is weak under our definition with small R^2 at 0.4595, but mechanical strain does plays a role in reduced energy barrier of O_{ads} hydration.

BIBLIOGRAPHY

(1) Fortunelli, A.; Goddard III, W. A.; Sementa, L.; Barcaro, G.; Negreiros, F. R.; Jaramillo-Botero, A. The Atomistic Origin of the Extraordinary Oxygen Reduction Activity of Pt3Ni7 Fuel Cell Catalysts. Chemical Science 2015, 6 (7), 3915–3925. https://doi.org/10.1039/C5SC00840A.

(2) Sanz-Navarro, C. F.; Åstrand, P.-O.; Chen, D.; Rønning, M.; van Duin, A. C. T.; Jacob, T.; Goddard, W. A. Molecular Dynamics Simulations of the Interactions between Platinum Clusters and Carbon Platelets. J. Phys. Chem. A 2008, 112 (7), 1392–1402. https://doi.org/10.1021/jp074806y.

(3) Li, M.; Zhao, Z.; Cheng, T.; Fortunelli, A.; Chen, C.-Y.; Yu, R.; Zhang, Q.; Gu, L.; Merinov, B. V.; Lin, Z.; Zhu, E.; Yu, T.; Jia, Q.; Guo, J.; Zhang, L.; Goddard, W. A.; Huang, Y.; Duan, X. Ultrafine Jagged Platinum Nanowires Enable Ultrahigh Mass Activity for the Oxygen Reduction Reaction. Science 2016, 354 (6318), 1414–1419. https://doi.org/10.1126/science.aaf9050.

(4) Chen, Y.; Huang, Y.; Cheng, T.; Goddard, W. A. Identifying Active Sites for CO2 Reduction on Dealloyed Gold Surfaces by Combining Machine Learning with Multiscale Simulations. J. Am. Chem. Soc. 2019, 141 (29), 11651–11657. https://doi.org/10.1021/jacs.9b04956.

(5) Huang, Y.; Chen, Y.; Cheng, T.; Wang, L.-W.; Goddard, W. A. Identification of the Selective Sites for Electrochemical Reduction of CO to C 2+ Products on Copper Nanoparticles by Combining Reactive Force Fields, Density Functional Theory, and Machine Learning. ACS Energy Letters 2018, 2983–2988. https://doi.org/10.1021/acsenergylett.8b01933.

(6) Kresse, G.; Hafner, J. Ab Initio Molecular-Dynamics Simulation of the Liquid-Metal--Amorphous-Semiconductor Transition in Germanium. Phys. Rev. B 1994, 49 (20), 14251–14269. https://doi.org/10.1103/PhysRevB.49.14251.

(7) Kresse, G.; Joubert, D. From Ultrasoft Pseudopotentials to the Projector Augmented-Wave Method. Phys. Rev. B 1999, 59 (3), 1758–1775. https://doi.org/10.1103/PhysRevB.59.1758.

(8) Mathew, K.; Sundararaman, R.; Letchworth-Weaver, K.; Arias, T. A.; Hennig, R. G. Implicit Solvation Model for Density-Functional Study of Nanocrystal Surfaces and Reaction Pathways. J. Chem. Phys. 2014, 140 (8), 084106. https://doi.org/10.1063/1.4865107.

(9) Henkelman, G.; Uberuaga, B. P.; Jónsson, H. A Climbing Image Nudged Elastic Band Method for Finding Saddle Points and Minimum Energy Paths. J. Chem. Phys. 2000, 113 (22), 9901–9904. https://doi.org/10.1063/1.1329672.

(10) Jia, Q.; Caldwell, K.; Strickland, K.; Ziegelbauer, J. M.; Liu, Z.; Yu, Z.; Ramaker, D. E.; Mukerjee, S. Improved Oxygen Reduction Activity and Durability of Dealloyed PtCox Catalysts for Proton Exchange Membrane Fuel Cells: Strain, Ligand, and Particle Size Effects. ACS Catal 2015, 5 (1), 176–186. https://doi.org/10.1021/cs501537n.

(11) Heyden, A.; Bell, A. T.; Keil, F. J. Efficient Methods for Finding Transition States in Chemical Reactions: Comparison of Improved Dimer Method and Partitioned Rational Function Optimization Method. J. Chem. Phys. 2005, 123 (22), 224101. https://doi.org/10.1063/1.2104507.

A p p e n d i x   B

SUPPORTING INFORMATION FOR CHAPTER III

B1. Gold Nanoparticle Synthesis using ReaxFF Reactive Molecular Dynamics

Using the same approach as in our earlier work[1], the 10nm gold nanoparticle investigated here is computationally synthesized by carrying out ReaxFF reactive molecular dynamics, where a multiwall carbon nanotube (CNT) is used as the catalysis support. We use the Embedded-atom-model (EAM)[2] to describe the interactions between gold atoms, and the Lennard-Jones (LJ) potential to model the interaction between gold atoms and CNT. To best mimic experimental chemical vapor deposition (CVD), gold atoms are added to the simulation box with the deposition rate of 3.0 Å/ns for 35 ns (the CVD experiment deposition rate is 2 Å/s for 50 s) and simulated annealing with the peak temperature at 1164K is carried out to heal the defect afterwards. 20 ps reactive molecular dynamics[3] at 300K is then carried out to refine the final structure after 63 annealing cycles. The predicted XRD spectra and TEM images show that the simulated structure agrees with experiment. All the simulations are carried out in LAMMPS. The predicted TEM image and atomic structure of synthesized AuNP on CNT are also shown in the earlier work[1].

B2. Surface Atoms Extraction using the Surface Vector Method

Surface and bulk atoms are distinguished by the following procedure: for each gold atom, we first cut a sphere of 8 Å radius around the selected atom(cAu) from whole nanoparticle, as shown in Figure B-1. Then we sum up all the cAu-nAu vectors pointing from the center atom(cAu) to other atoms(nAu) in the nanoclusters and take the negative norm of this summed vector as surface vector (red vector in Figure B-1). This selected Au atom is defined as a surface atom if all the angles between cAu-nAu vector and surface vector are larger than the given threshold, which is optimized to 30 degree in our system, otherwise it's defined as a bulk atom. The same 8 Å nanocluster model will be used later for DFT calculations and feature extraction for neural network(NN) inputs.

B3. Datasets Generation from DFT Calculations

All datasets presented in this work are generated from density functional theory(DFT) calculations in VASP package[4], using the PBE functional including the D3 London

Dispersion correction and the projector augmented wave (PAW) method[5]. We set the kinetic energy cutoff at 400 eV and the Methfessel-Paxton smearing of second order is used with the width of 0.2 eV. The convergence criteria are 10^{-5} eV differences for electronic energy and all geometries are relaxed until the force converged to 10^{-2} eV/Å. Only gamma point is considered in these calculations. We use the 8 Å nanocluster as described above for DFT calculations. The cluster with different adsorbates (CO or HOCO) is put into a 20 Å cubic box with all Au atoms fixed. The two physical descriptors we use here for evaluating the activity of a site are ΔE_{CO} and ΔE_{HOCO} as described in *Section 3.2.1.*

B4. Modeling Dealloyed Gold Surfaces

To model the dealloyed gold surfaces as in earlier work[6], we first cut an 10nm gold sphere from gold single crystal and randomly remove 25% of Au atoms on the surface. Simulated annealing with the peak temperature at 1164K is carried out to equilibrate the structure afterwards. 100 ps ReaxFF reactive molecular dynamics at 300K is then carried out to refine the final structure after 10 annealing cycles. All calculations are carried out in LAMMPS.

B5. Neural Network Based Machine Learning Model

We use the neural network based machine learning algorithm in this work. The overall structure of model topology is shown schematically in Figure 3-2. For a nanocluster with N atoms taking the cAu atom as center, the Cartesian coordinates of all atoms in the cluster are given. We first calculate the N-1 interatomic distances (R_{ij}), and transform them to a set of symmetry function values, which we call input features. Two main parts of features are two-body terms(C_2) and three-body terms(C_3). As shown in Figure B-2(B), two-body terms are constructed by summing over all nAu atoms in the systems and three-body terms are iterated through all triangles taking cAu atom in one corner. The mathematical representation of two-body terms and three-body terms are also shown in Equation 1 and 2, where f is the symmetry function. This type of feature representation method is derived from the work by Behler and Parrinello in 2007[7]. We use localized piecewise cosine function as symmetry functions instead of Gaussian functions, as in Equation 3. These piecewise cosine functions are more localized than Gaussian functions with the value of zero outside their cutoff distance[8,9]. For the three-body term, we no longer need the angle of dependence with three

sides treated equally, which is also one of the reasons why we are using this simplified version of Gaussian functions. In our model, we use 12 symmetry functions for two-body terms and 3 symmetry functions for three-body terms, leading to a total number of 39 input features. We consider this gives the best balance of dataset size and model complexity. Having defined a set of features, a fully connected two-layer neural network with 30 nodes in the first layer and 50 nodes in the second layer are followed to fit two selected physical descriptors: ΔE_{CO} and ΔE_{HOCO} . The total number of model parameters is 2801. The main idea is to represent the physical descriptors as a function of two-body terms and three-body terms with the weight parameters w and bias parameters b, as in *Equation 4*.

Two-Body Term: $C\_2_{m,i} = \sum_j f_m(R_{ij})$, (1)

Three-Body Term: $C\_3_{mnl,i} = \sum_{jk} f_m(R_{ij})f_n(R_{ik})f_l(R_{jk})$, (2)

Basis Function (Localized Cosine Piecewise Function):

$$f_m(R_{ij}) = \begin{cases} \frac{1}{2}\cos(\frac{R_{ij}-d_m}{r}\pi) + \frac{1}{2}, & |R_{ij} - d_m| < r; \\ 0, & Otherwise \end{cases}, (3)$$

$$E_i = F_{NN}(C\_2_{m,i}, C\_3_{mnl,i}\}; w, b), (4)$$

Where,

C_2, C_3 are the symmetry functions of two-body terms and three-body terms, and m, n, l are indices of these symmetry functions;

i is the index of surface atom, and j and k are the indices of nAu atom (Figure B-1);

d_m and r is the center and width of symmetry function as shown in Figure B-2(A);

F_{NN} is the neural network function taking the two-body terms and three-body terms as variables and in parameter of weights and bias.
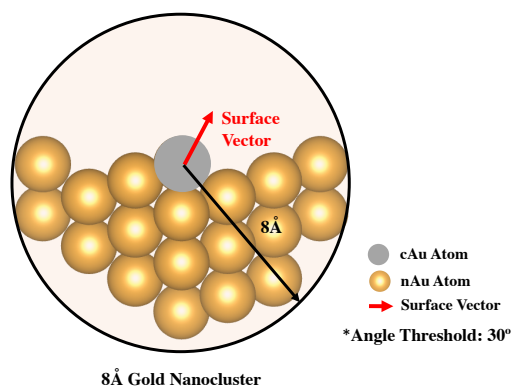
Figure B-1. 8 Å nanocluster model, where we use surface vector method to distinguish whether the cAu atom is a surface atom or a bulk atom. Same model will be used later for DFT calculations and feature extraction for neural network inputs. cAu Atom: center atom; nAu Atom: other atoms in the nanocluster.
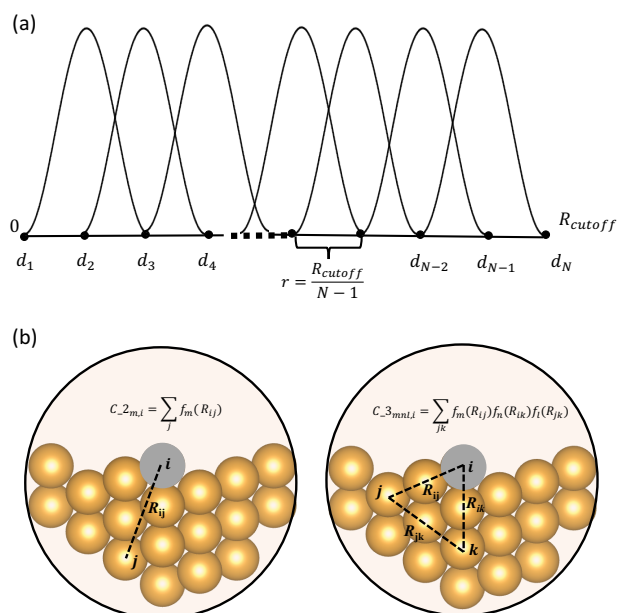

Figure B-2. Mapping geometric features to symmetry functions. (a) Localized piecewise cosine symmetry functions. d_m and r are the center and width of symmetry function. In our model, R_{cutoff} is set to 8 Å;(b) Illustration of Two-Body Term and Three-Body Term. Two-body terms are constructed by summing over all nAu atoms and three-body terms are

iterated through all triangles taking cAu atom in one corner. We use 12 symmetry functions for two-body terms and 3 symmetry functions for three-body terms, which leads to a total number of 39 input features to neural network.
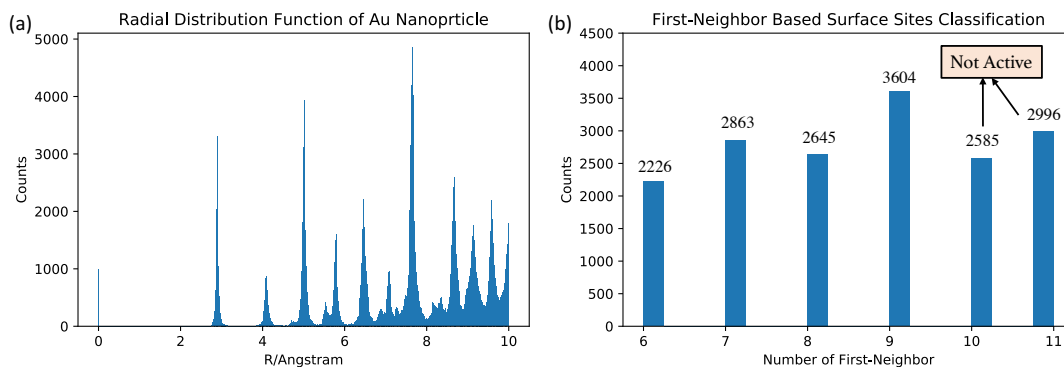

Figure B-3. (a) Au-Au radial distribution function for Au nanoparticles synthesized by reactive molecular dynamics. The first peak appears at 2.80 Å and the second peak appears at 4.20 Å. We choose first-neighbor cutoff at 3.30 Å here; (b) Surface sites classification based on first-neighbor. We classify all 16919 surface sites into six groups based on their number of first-neighbor (coordination). Sites with 10 or 11 first-neighbor are not active for CO2RR since they cannot adsorb HOCO or show very high HOCO formation energy.
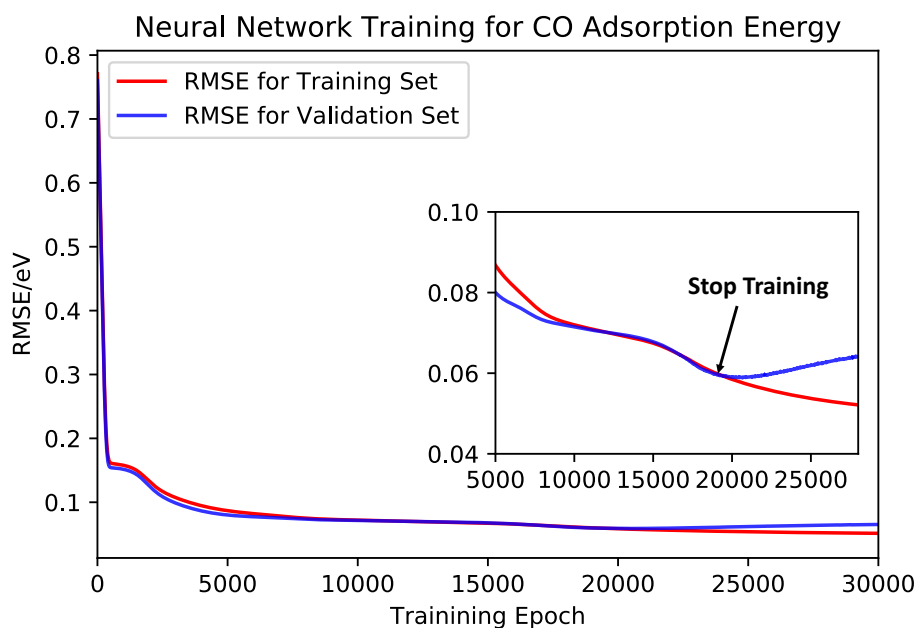
Figure B-4. Training log for CO adsorption energy, ΔE_{CO}. Validation set is used for preventing overfitting (early-stop). At epoch 19000, the RMSE of validation set reached minimum at 0.0591 eV with the RMSE of training set at 0.0563 eV, where we stop the training.
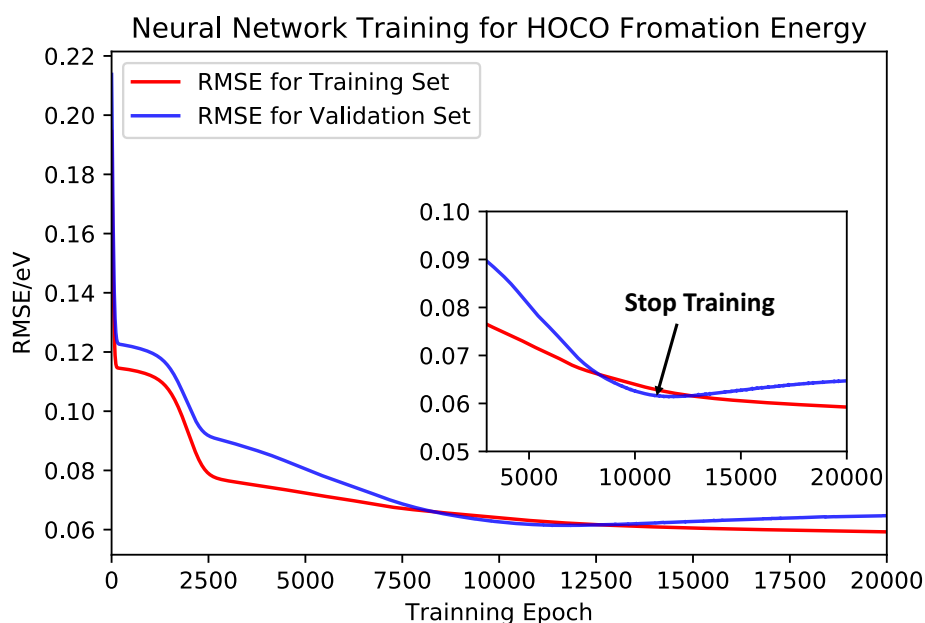

Figure B-5. Training log for COOH formation energy, ΔE_{HOCO}. Validation set is used for early-stop and prevent overfitting. At epoch 11000, the RMSE of validation set reaches minimum at 0.0593 eV with the RMSE of training set at 0.0616 eV, where we stop the training.

Data Sets	Coordination				Data Set Size	Final RMSE/eV
	6	7	8	9		
Training Set	276	276	276	276	1104	0.0563
Validation Set	35	35	35	35	140	0.0591
Testing Set	35	35	35	35	140	0.0521

Table B-1. Partition of data sets and final RMSE for CO adsorption energy training, ΔE_{CO}. To have a complete training set, we constrain the ratio of sites from each coordination group to be equal within each set. All surface sites within each group are selected randomly and all three sets are totally independent.

0	Coordination				Data Set Size	Final RMSE/eV
	6	7	8	9		
Training Set	224	214	209	212	859	0.0616
Validation Set	25	25	25	25	100	0.0593
Testing Set	25	25	25	25	100	0.0614

Table B-2. Partition of data sets and final RMSE for HOCO formation energy, ΔE_{HOCO}. To have a complete training set, we constrain the ratio of sites from each coordination group to be equal within each group. All surface sites within each group are selected randomly and all three sets are totally independent.
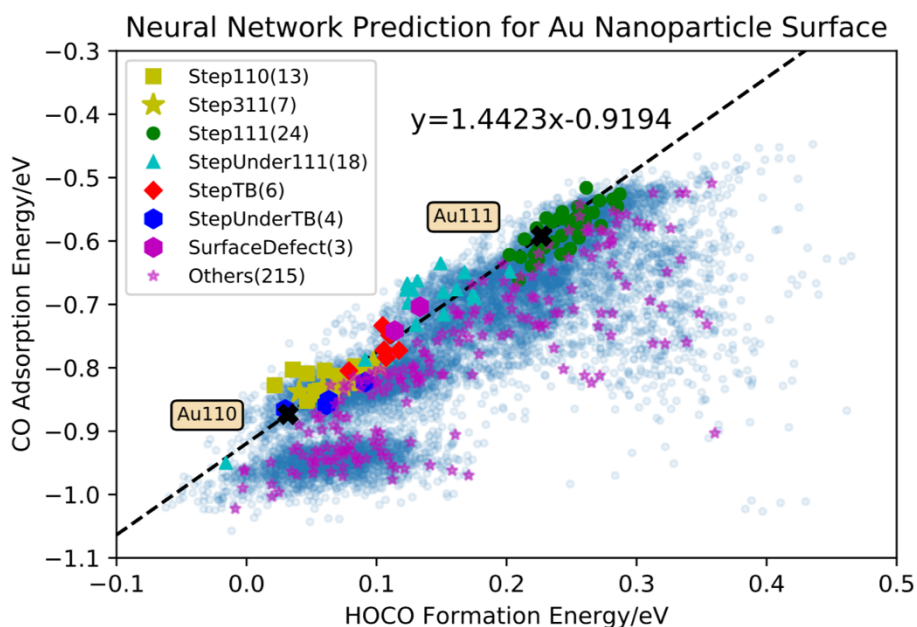

Figure B-6. Identification results of 300 sites randomly selected from all surface sites with the number of sites shown in the bracket next to the markers. The majority of randomly selected 300 sites are not from seven active groups, indicating that the seven groups are only concentrated above the straight line with a-value at 0.9194.

Type of Sites	Top 300 Sites	Random 300 Sites
Step110	66	13
Step311	24	7
Step111	47	24
StepUnder111	115	18
StepTB	34	6
StepUnderTB	11	4
SurfaceDefect	3	3
Others	0	215

Table B-3. Comparison of top 300 sites and random 300 sites. The majority of random 300 sites are not from seven active groups (as marked as star in *Figure B-6*), which implies that seven active groups mainly concentrate above and around the straight line.
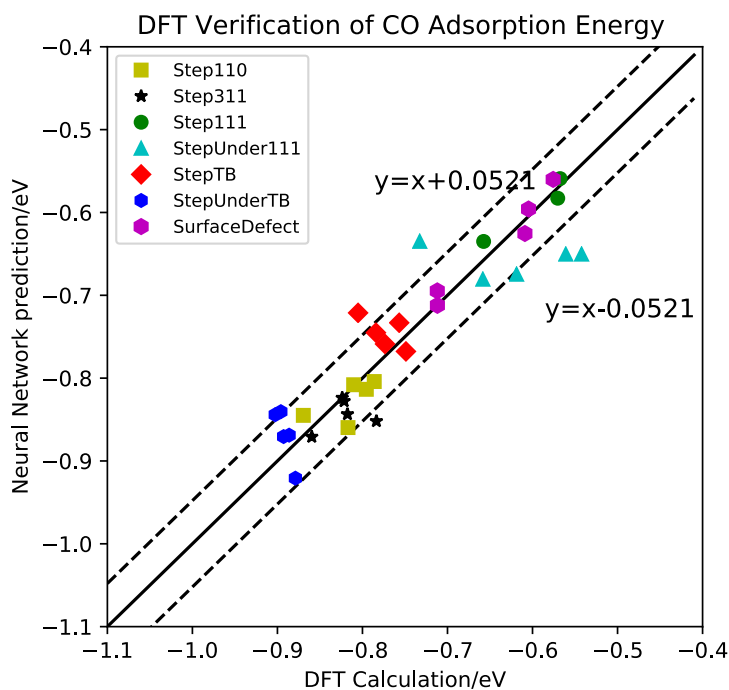

Figure B-7. DFT verification of CO adsorption energy for seven active groups. RMSE of machine learning model for CO adsorption energy is 0.0521 eV (dashed line is the error bound). We randomly selected 5 sites from each group and as we could see most sites lie

within the error bound, which support our model is accurate and on the other hand validate the seven groups are the sites with better CO2RR performance.
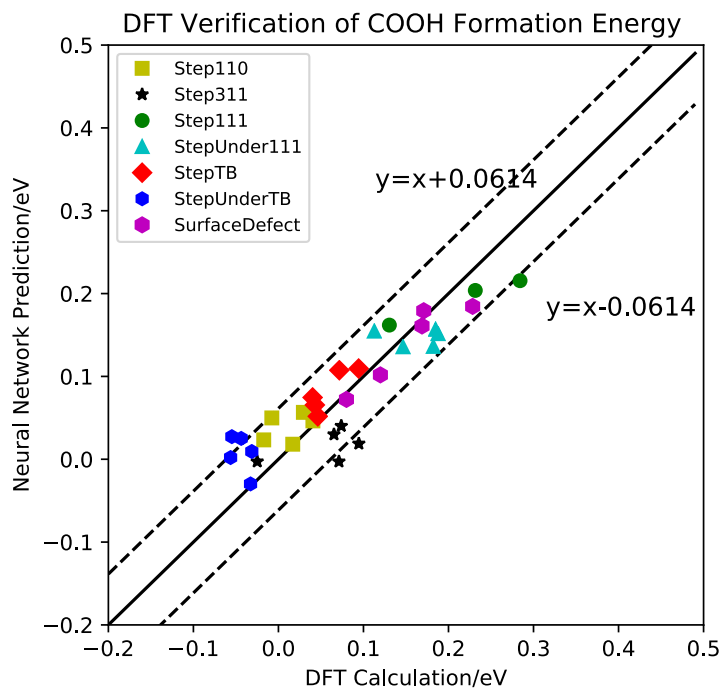

Figure B-8. DFT verification of HOCO formation energy for seven active groups. RMSE of machine learning model for HOCO formation energy is 0.0614 eV (dashed line is the error bound). We randomly selected 5 sites from each group and as we could see most sites lie within the error bound, which support that our model is accurate and on the other hand validates that the seven groups are the sites with better CO2RR performance.
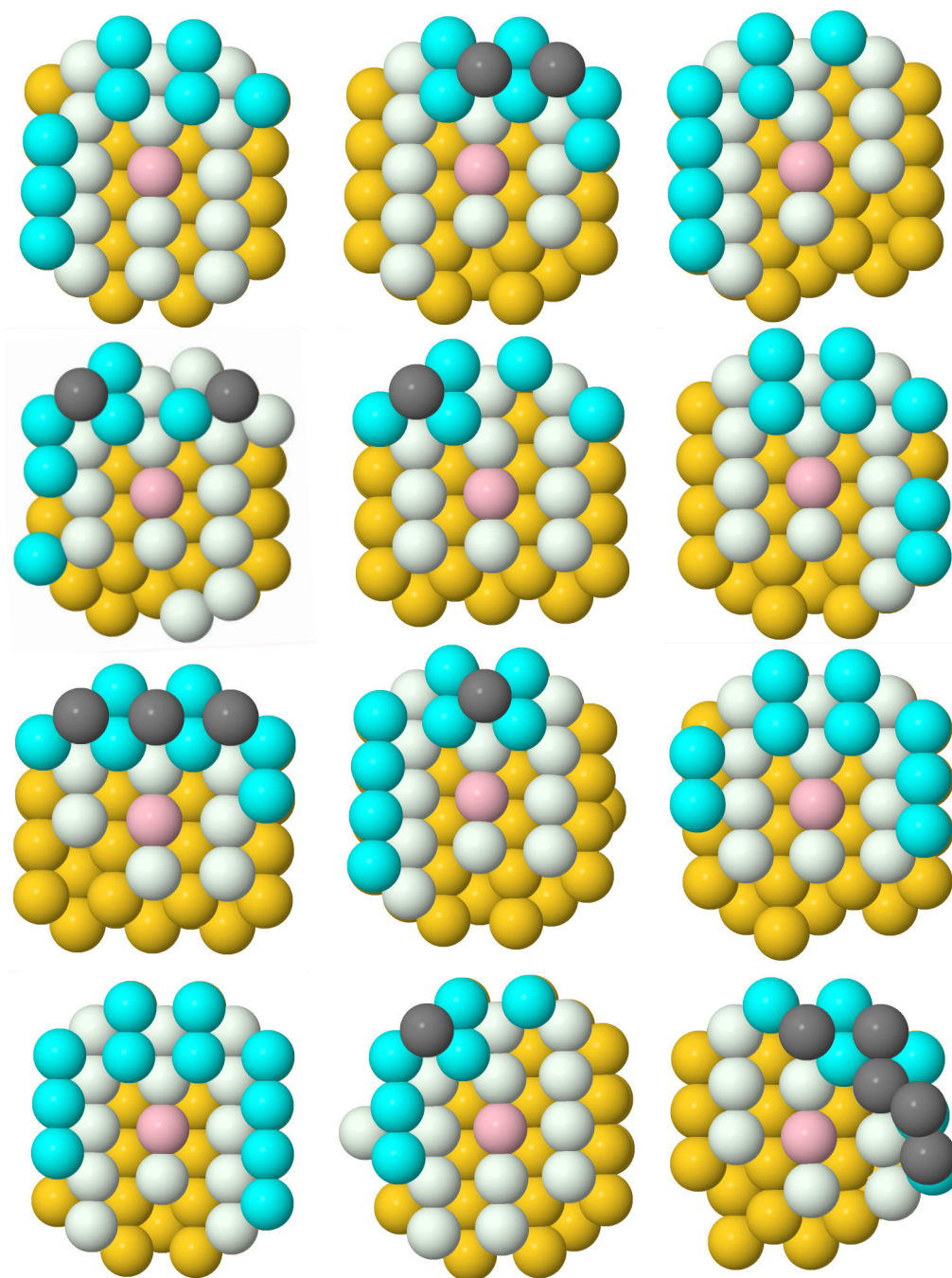
Figure B-9. 12 structures from Group of Step110. The center atom is pink, while atoms at the same layer are white. Atoms in the layer below white atoms are gold, while atoms one layer above center atom are cyan. Atoms above cyan atoms are gray and twin boundaries are dashed line.

Figure B-10. 12 Structures from Group of Step311. The center atom is pink, while atoms at the same layer are white. Atoms in the layer below white atoms are gold, while atoms one layer above center atom are cyan. Atoms above cyan atoms are gray and twin boundaries are dashed line.
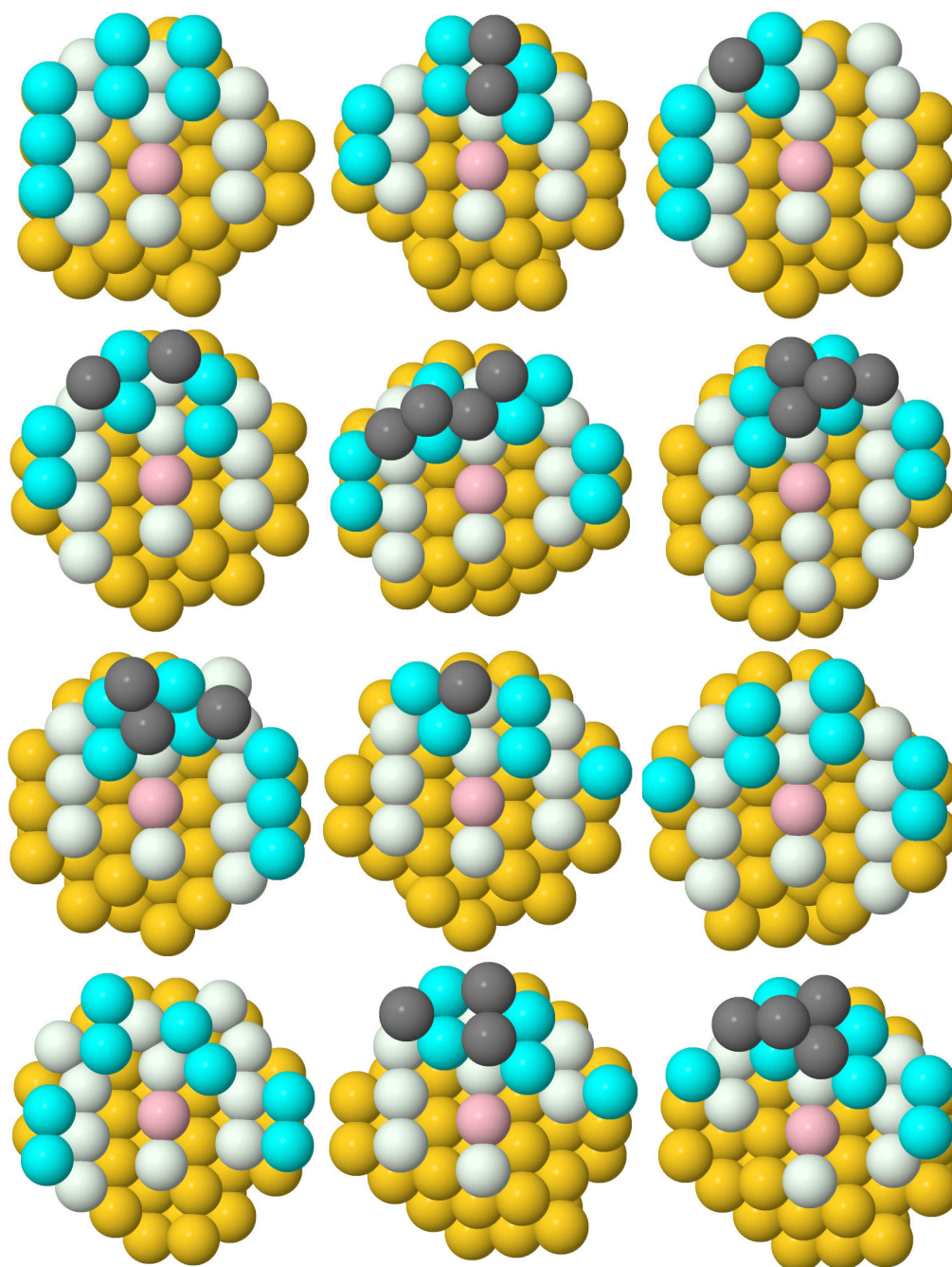
Figure B-11. 12 Structures from Group of Step111. The center atom is pink, while atoms at the same layer are white. Atoms in the layer below white atoms are gold, while atoms one layer above center atom are cyan. Atoms above cyan atoms are gray and twin boundaries are dashed line.

Figure B-12. 12 Structures from Group of StepUnder111. The center atom is pink, while atoms at the same layer are white. Atoms in the layer below white atoms are gold, while atoms one layer above center atom are cyan. Atoms above cyan atoms are gray and twin boundaries are dashed line.
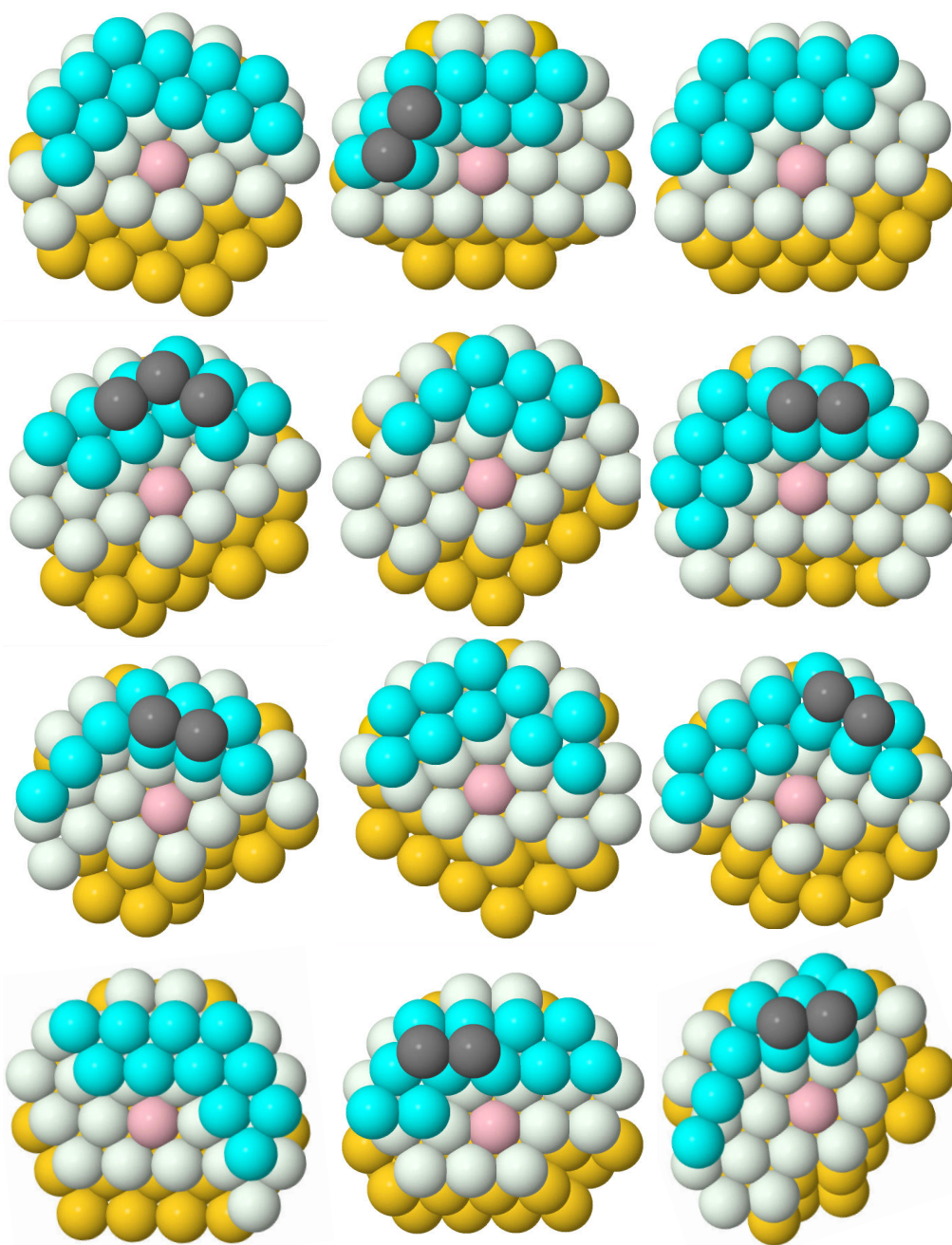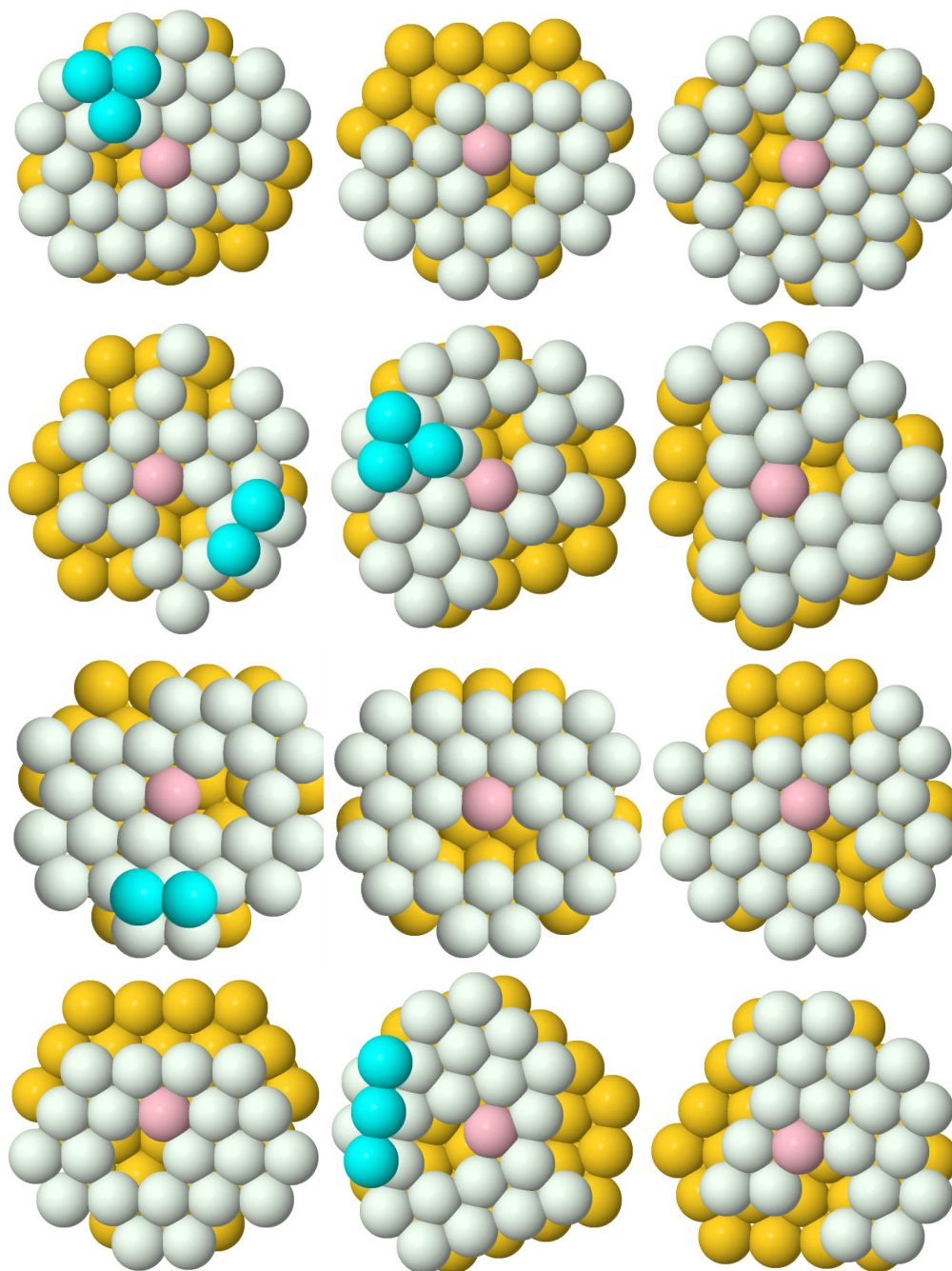
Figure B-13. 12 Structures from Group of SurfaceDefect. The center atom is pink, while atoms at the same layer are white. Atoms in the layer below white atoms are gold, while atoms one layer above center atom are cyan. Atoms above cyan atoms are gray and twin boundaries are dashed line.
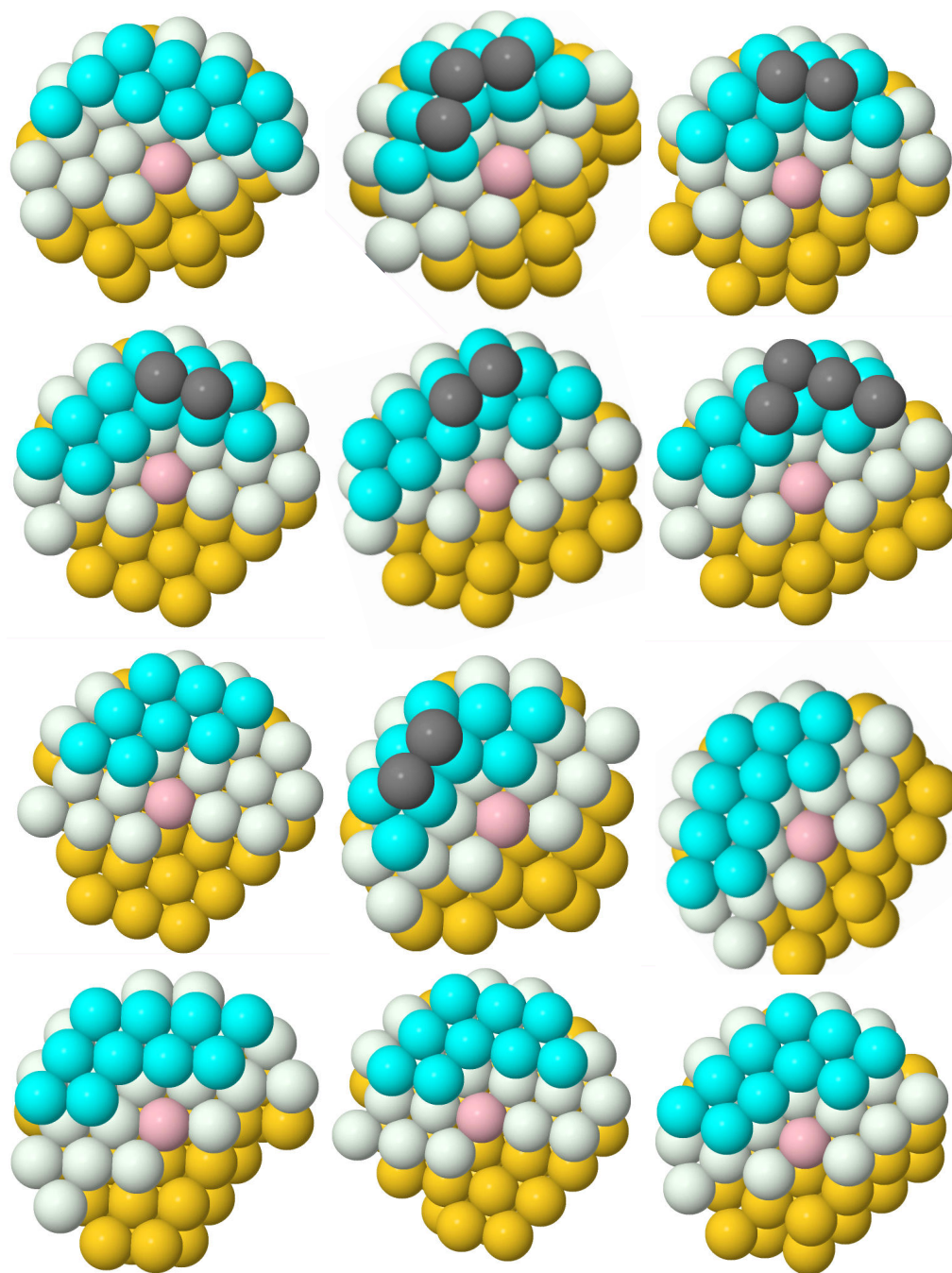
Figure B-14. 12 Structures from Group of StepTB. The center atom is pink, while atoms at the same layer are white. Atoms in the layer below white atoms are gold, while atoms one layer above center atom are cyan. Atoms above cyan atoms are gray and twin boundaries are dashed line.

Figure B-15. 12 Structures from Group of StepUnderTB. The center atom is pink, while atoms at the same layer are white. Atoms in the layer below white atoms are gold, while atoms one layer above center atom are cyan. Atoms above cyan atoms are gray and twin boundaries are dashed line.
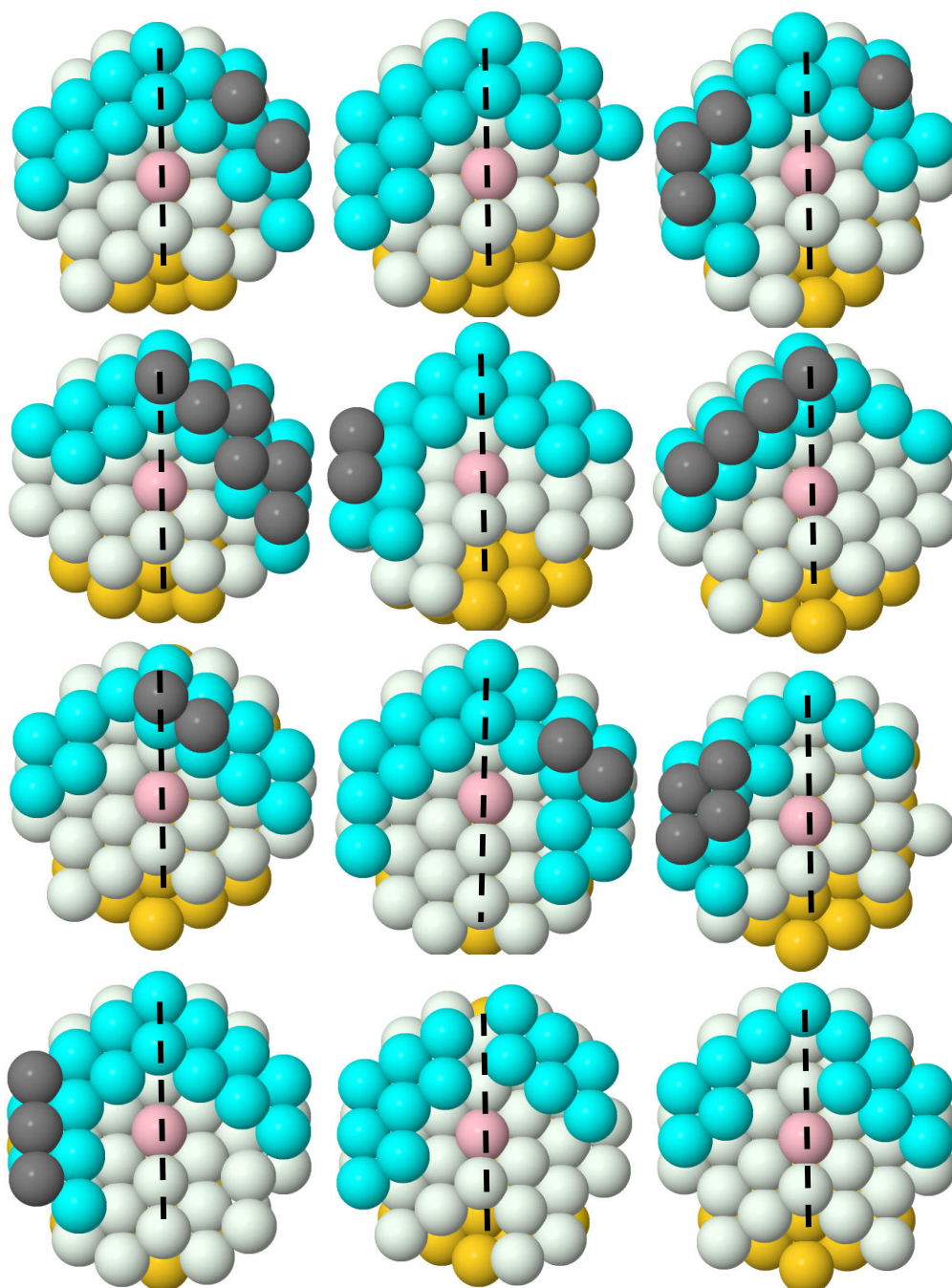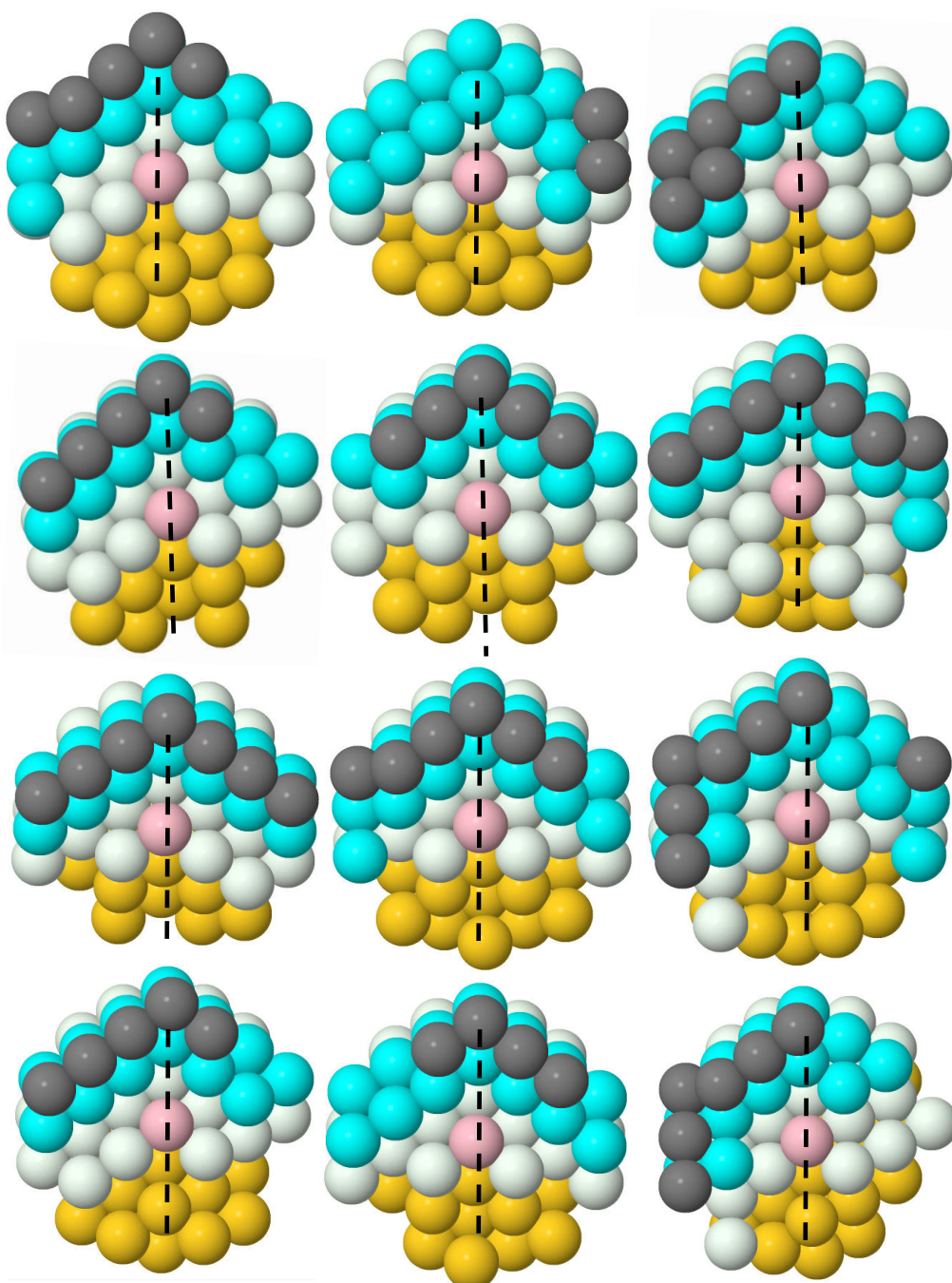
BIBLIOGRAPHY

(1) Cheng, T.; Huang, Y.; Xiao, H.; Goddard, W. A. Predicted Structures of the Active Sites Responsible for the Improved Reduction of Carbon Dioxide by Gold Nanoparticles. *The Journal of Physical Chemistry Letters* **2017**, *8* (14), 3317–3320. https://doi.org/10.1021/acs.jpclett.7b01335.

(2) Foiles, S. M.; Baskes, M. I.; Daw, M. S. Embedded-Atom-Method Functions for the Fcc Metals Cu, Ag, Au, Ni, Pd, Pt, and Their Alloys. *Phys. Rev. B* **1986**, *33* (12), 7983–7991. https://doi.org/10.1103/PhysRevB.33.7983.

(3) van Duin, A. C. T.; Dasgupta, S.; Lorant, F.; Goddard, W. A. ReaxFF: A Reactive Force Field for Hydrocarbons. *The Journal of Physical Chemistry A* **2001**, *105* (41), 9396–9409. https://doi.org/10.1021/jp004368u.

(4) Kresse, G.; Hafner, J. *Ab Initio* Molecular-Dynamics Simulation of the Liquid-Metal–Amorphous-Semiconductor Transition in Germanium. *Physical Review B* **1994**, *49* (20), 14251–14269. https://doi.org/10.1103/PhysRevB.49.14251.

(5) Kresse, G.; Joubert, D. From Ultrasoft Pseudopotentials to the Projector Augmented-Wave Method. *Physical Review B* **1999**, *59* (3), 1758–1775. https://doi.org/10.1103/PhysRevB.59.1758.

(6) Sun, K.; Cheng, T.; Wu, L.; Hu, Y.; Zhou, J.; Maclennan, A.; Jiang, Z.; Gao, Y.; Goddard, W. A.; Wang, Z. Ultrahigh Mass Activity for Carbon Dioxide Reduction Enabled by Gold–Iron Core–Shell Nanoparticles. *Journal of the American Chemical Society* **2017**, *139* (44), 15608–15611. https://doi.org/10.1021/jacs.7b09251.

(7) Behler, J.; Parrinello, M. Generalized Neural-Network Representation of High-Dimensional Potential-Energy Surfaces. *Physical Review Letters* **2007**, *98* (14). https://doi.org/10.1103/PhysRevLett.98.146401.

(8) Huang, Y.; Chen, Y.; Cheng, T.; Wang, L.-W.; Goddard, W. A. Identification of the Selective Sites for Electrochemical Reduction of CO to C_{2+} Products on Copper

Nanoparticles by Combining Reactive Force Fields, Density Functional Theory, and Machine Learning. *ACS Energy Letters* **2018**, 2983–2988. https://doi.org/10.1021/acsenergylett.8b01933.

(9) Huang, Y.; Kang, J.; Goddard, W. A.; Wang, L.-W. Density Functional Theory Based Neural Network Force Fields from Energy Decompositions. *Physical Review B* **2019**, *99* (6), 064103. https://doi.org/10.1103/PhysRevB.99.064103

A p p e n d i x   C

SUPPORTING INFORMATION FOR CHAPTER IV

C1. Methods

C1.1 ReaxFF

The copper nanoparticle investigated in this study is computationally synthesized in the same way as in previous work[1]. The embedded-atom model (EAM)[2] was used to model the interactions between copper atoms. To simulate the chemical vapor deposition (CVD) synthesis, copper atoms are added to the simulation box in a rate of 3.2A/ns for 30ns. After the nanoparticle condenses, a total of 38 simulated annealing cycles is applied to relax the initially formed structure. Each cycle involves a heating step from 300K to 1200K in 5ps, high temperature step at 1200K for 5ps, cooling step from 1200K to 300K in 5ps, and room temperature step at 300K. At last, the final copper nanoparticle is relaxed using the reactive force field[3] at 300K for 20ps.

C1.2 DFT

The density functional theory (DFT) calculations are performed in VASP[4]. The PBE functional[5] is used to obtain electronic energy. The plane wave basis up to a kinetic energy cutoff of 400eV is used to describe the wave function. Since copper is metallic, the method of Methfessel-Paxton of order 1 is used for smearing. The smearing width is 0.2eV. The convergence criteria for electronic energies is $1e^{-5}$eV, and the geometries are optimized until the force converged to be within an error of 0.01eV/A.

ΔE_{CO} and ΔE_{OCCOH} are calculated in the same way as in previous work[1]:

$\Delta E_{CO} = E_{*CO} - E_* - E_{CO}$

$\Delta E_{OCCOH} = E_{*OCCOH} - E_{[*CO, CO]} - 0.5 \times E_{H2}$

C1.3 Neural Network Machine Learning Model

The neural network used in this study is of the type by Behler and Parrinello[6]. However, instead of summing up contributions from all atoms, only the contribution from the target

surface atom is used. In this study, instead of the atomic energy, the quantity to be fitted using machine learning is the CO adsorption energy.

As we have shown earlier[1, 7], the CO adsorption energy can be sufficiently described on the surface of the nanoparticle by considering all the atoms within 8A of the surface site. Thus, a copper cluster of 8A radius about each surface atom is extracted from the nanoparticle to compute the CO adsorption energy. Subsequently, the same cluster is used as the input to the machine learning model. Since we are only considering the chemical behavior of the chosen surface site, only molecular descriptions about that site are used as input to the neural network. Similar to our previous model, two-body and three-body features are used. The overall structure of the neural network machine learning model is shown as below:

And mathematically, the above model is represented as follows:

$$G_{i\alpha}{}^{(2)} = \Sigma_j \phi_\alpha{}^{(2)} (p_{ij}), \; G_{i\beta}{}^{(3)} = \Sigma_{jk} \phi_\beta{}^{(3)} (p_{ij}, q_{ijk}) \; (1)$$

$$E_{CO} = F_{NN} (\{G_{i\alpha}{}^{(2)}, G_{i\beta}{}^{(3)}\}; w, b) \; (2)$$

Where $G_{i\alpha}{}^{(2)}$ and $G_{i\beta}{}^{(3)}$ are the 2- and 3-body descriptors from the 2- and 3-body geometrical features p_{ij} and q_{ijk}, e.g., the 2-body term can include the interatomic distance $p_{ij} = R_{ij}$, and the 3-body term can include the angle formed by three atoms $q_{ijk} = \theta_{ijk}$. Finally, the function F_{NN} (G; w, b) represents the network that transforms the input descriptors G into a single value using the parameters with weights w and biases b. The final value calculated from the whole model is the CO adsorption energy, as represented by equation (2).

The molecular descriptors as input to the neural network can be extracted in many ways. In this study, the set of piecewise cosine functions is used because it is a more systematic way of constructing locally based symmetry functions.

$$R_\alpha^k = R_{inner} + (\alpha - 1)h_k \quad \text{where } \alpha = 1, 2, ..., M_k$$

$$\varphi_\alpha^{(k)}(R_{ml}) = \{1/2 * \cos((R_{ml} - R_\alpha^k)/h_{k\pi}) + 1/2, \; |Rml - R_\alpha^k| < h_k \text{ ,Otherwise (3)}$$

$$G_{\alpha,l}^{(2)} = \Sigma_m \varphi_\alpha^{(2)} (R_{ml}) \; (4)$$

$$G_{\alpha\beta\gamma,l}^{(3)} = \Sigma_{m,n}\varphi_\alpha^{(3)}(R_{ml})\ \varphi_\beta^{(3)}(R_{nl})\ \varphi_\gamma^{(3)}(R_{mn})\ (5)$$

where:

$\varphi_\alpha^{(k)}(R_{ml})$ is the piecewise cosine function over the interatomic distance R_{ml}

$k = 2,3$ corresponds the 2-body and 3-body terms, and

$h_k = (R_{outer} - R_{inner})/M_k$ is the width of the piecewise cosine functions.

The set of piecewise cosine functions are described by 4 quantities: the inner cutoff R_{inner}, the outer cutoff R_{outer}, the number of two-body functions M_2, and the number of three-body functions M_3. Here, the $M_2=12$ and $M_3=3$ are used, corresponding to a set of 30 unique descriptors for each copper cluster. Because each cluster is only of 8 angstroms, we can include all the atoms in the descriptor. Thus, R_{outer} is set to 8A. Since only 12 two-body functions are used, the width of each piecewise cosine function is relatively large, thus, R_{inner} can be set to 0. Once the input atomic descriptors are assembled about the target surface site, it is fed through a two-layer neural network each with 50 nodes to produce one output, which is then fitted to the adsorption energy.

C2. Implementation and Training of the Neural Network Model

Once the structure of the neural network is constructed, the weights and biases of the neural network model are initialized using the Xavier initializer[8]. Then using the 8:1:1 split of the data set for training, validation and testing, we obtain the following RMSE as a function of training iterations, as shown in Figure C-2(a). The final RMSE of the training set, validation set, and test set are 0.111eV, 0.117eV, and 0.123eV. The overall distributions between the DFT energies and the neural network predicted values also agree, as shown in Figure C-2(b).
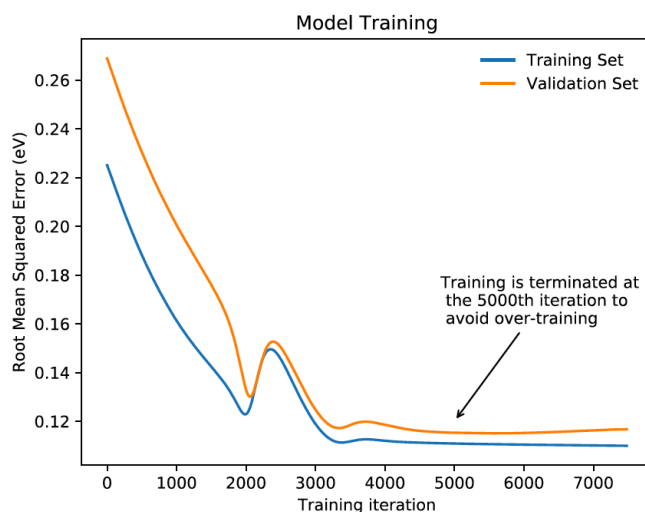
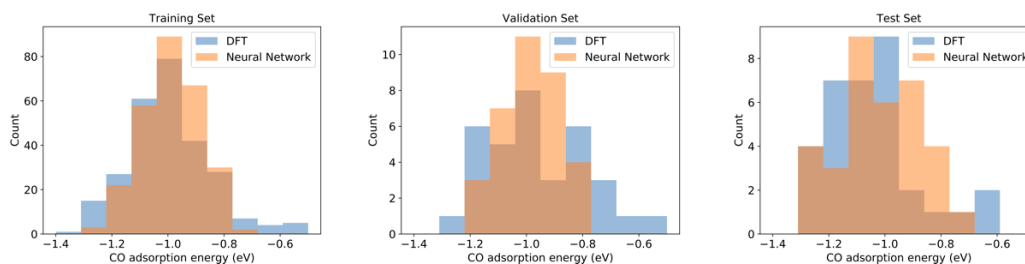***Figure C-1.*** RMSE of the training set and validation set as functions of the training iterations.

Figure C-2. Distribution of the energies between the DFT values and the neural network predicted values for the training set, validation set, and the test set.

Unit: eV	DFT range	NN range
Training Set	[-1.284, -0.458]	[-1.262, -0.715]
Validation Set	[-1.276, -0.543]	[-1.158, -0.820]
Test Set	[-1.314, -0.433]	[-1.278, -0.761]

Table C-1. Energy ranges between DFT and neural network for the training set, validation set, and test set. Because CO does not adsorb on certain unfavorable sites, these sites are treated as high adsorption energies. Due to this, the upper end of the range has much larger error to include the unfavorable outliers than the lower end. However, NN predicts the lower end of the ranges very well, indicating that good CO adsorption sites are well identified.

NN sizes	Training set RMSE	Validation set RMSE	Test set RMSE
30x2	0.110 eV	0.123	0.140
40x2	0.115	0.118	0.135
50x2	0.108	0.119	0.122
60x2	0.103	0.116	0.117

Table C-2. RMSEs of the training set, validation set, and test set as functions of the neural network sizes. The notation *n*x2 indicates two hidden layers with *n* nodes are used in the neural network. Although the training set and validation set are fitted in similar accuracies between different sizes, the test set error is smaller when the size of the neural network increases. The neural network size of 50x2 is used to allow enough flexibility.

C3. Relationship between EOCCOH and C2 products selectivity

Hori et al. (2002)[9] reported the selectivity for C2 products on different crystalline surfaces of copper. Using their reported values and our theoretical *OCCOH reaction energy, EOCCOH, we found that the log of the ratio between C2H4 and CH4 correlates almost linearly EOCCOH, as shown in the following figure. This is not surprising because the reaction rates are typically exponentially dependent on energy as in the Eyring equation or Arrhenius equation. However, the good fit between the selectivity and EOCCOH implies that EOCCOH is a good descriptor for the selectivity of C2 products.
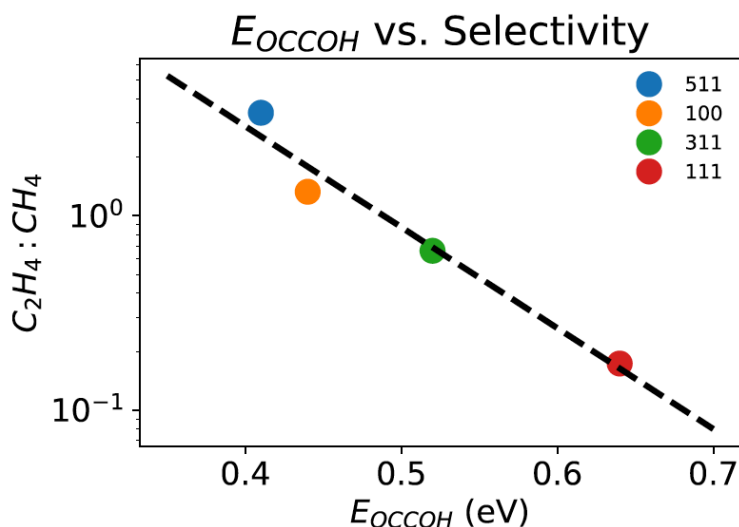

Figure C-3. Experimental C2H4:CH4 ratio and the reaction energy of EOCCOH. Note that the logarithm of the ratios is used for the y-axis.

C4. Surface terminations of the Twin boundaries

Based on the configurations of the adsorbed *OCCOH on the copper clusters, there are 4 ways of placing the intermediate on the surface, as shown in the following figure, Figure C-4. This is due to two factors. First, the (100) surfaces intersecting at the twin boundary can be concave or convex, as indicated by the purple figure in Figure 4-4(a) in the main text and the side view in Figure C-4. Second, the plane formed by the adsorbed *OCCOH can be in the same plane as the page, or perpendicular to the page, as shown in top view in Figure C-4.

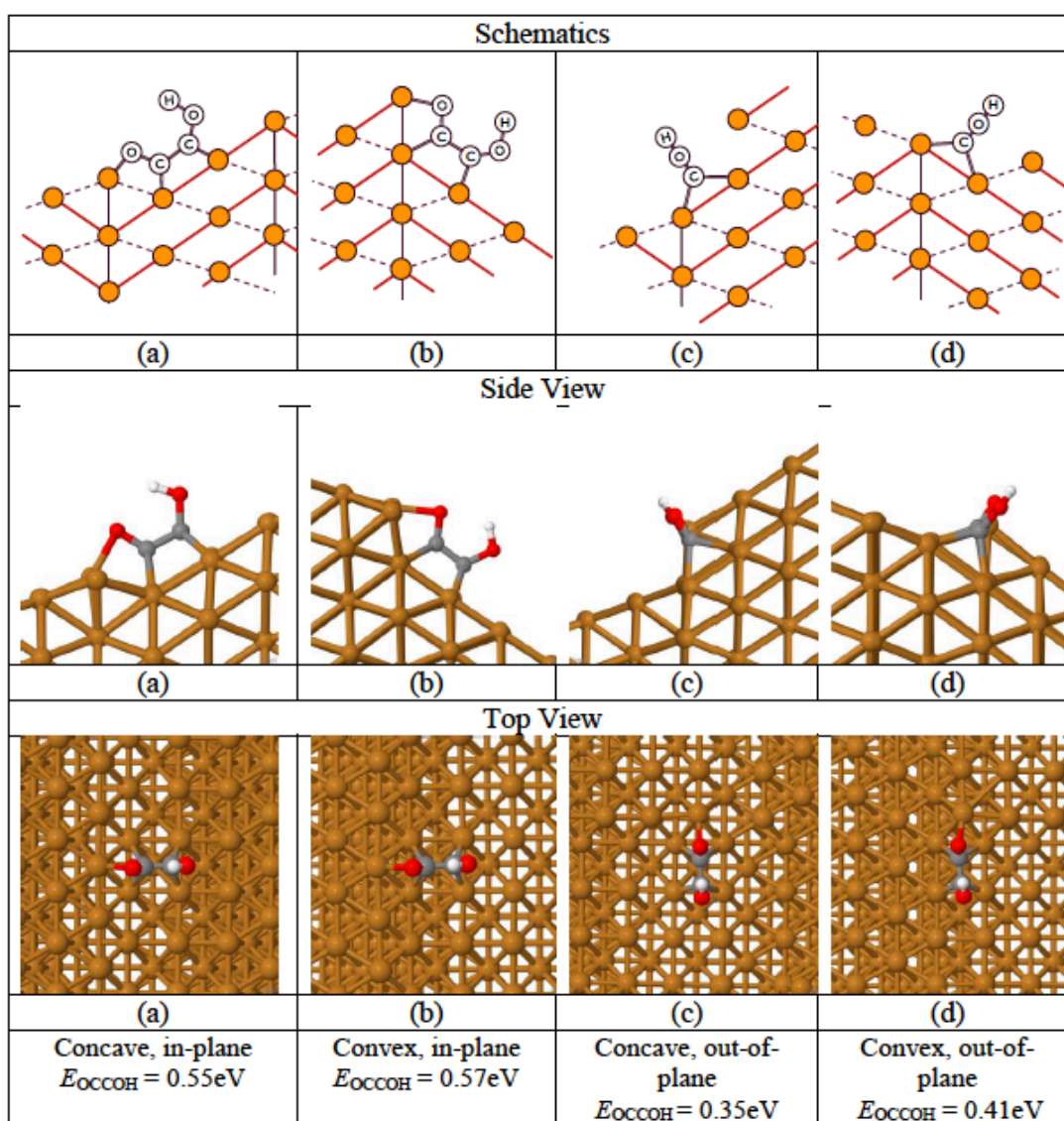| Schematics			
(a)	(b)	(c)	(d)
Side View			
(a)	(b)	(c)	(d)
Top View			
(a)	(b)	(c)	(d)
Concave, in-plane $E_{OCCOH} = 0.55eV$	Convex, in-plane $E_{OCCOH} = 0.57eV$	Concave, out-of-plane $E_{OCCOH} = 0.35eV$	Convex, out-of-plane $E_{OCCOH} = 0.41eV$

Figure C-4. The four configurations of *OCCOH binding at the twin boundary of copper. (a): *OCCOH adsorbed in-plane at the concave site; (b): *OCCOH adsorbed in-plane at the convex site; (c) *OCCOH adsorbed out-of-plane at the concave site; (d) *OCCOH adsorbed out-of-plane at the convex site.

C5. Prediction of Faradaic Efficiencies

The data for currents J_{C2+} and J_{H2} as functions of the grain boundary density d_{GB} are obtained from Figure 3(d) and (g) of reference [10]. First, since J_{H2} does not depend on d_{GB}, and the terminal value is 3.1 mA/cm2 for large d_{GB}, we then keep J_{H2} constant for this approximation. For C2+ production, J_{C2+} is fitted linearly as in the experimental data. Then we have:

$$J_{C2+} = 0.18 * d_{GB} - 0.399$$

$$J_{H2} = 0.31$$

Where d_{GB} is in units of μm-1, J_{C2+} and J_{H2} are in units of mA/cm2.

Our periodic structure has twin boundary density of 649.5 μm-1. Thus, the faradaic efficiency is then $J_{C2+} / (J_{C2+} + J_{H2}) = 97.4\%$

Also, [11] reported a copper structure with a large abundance of twin boundary sites with spacing of 5~70nm, which corresponds to densities of 14.3 to 200 μm-1. The corresponding faradaic efficiencies are 41.2% to 92.0%.

The results are summarized in Figure 4-5 of the main text.

BIBLIOGRAPHY

(1) Cheng, T., Xiao, H., and Goddard, W. A. (2017). Nature of the Active Sites for CO Reduction on Copper Nanoparticles; Suggestions for Optimizing Performance. Journal of the American Chemical Society, 139(34), 11642–11645.

(2) Daw, M. S., Foiles, S. M., Baskes, M. I. (1993). The embedded-atom method: a review of theory and applications. Materials Science Reports, 9(7–8), 251–310.

(3) van Duin, A. C. T., Dasgupta, S., Lorant, F., and Goddard, W. A. (2001). ReaxFF: A Reactive Force Field for Hydrocarbons. The Journal of Physical Chemistry A, 105(41), 9396-9409.

(4) G. Kresse and J. Hafner. Ab initio molecular-dynamics simulation of the liquid-metalamorphous-semiconductor transition in germanium. Phys. Rev. B, 49:14251, 1994; G. Kresse and J. Furthmüller. Efficiency of ab-initio total energy calculations for metals and semiconductors using a plane-wave basis set. Comput. Mat. Sci., 6:15, 1996.; G. Kresse and J. Furthmüller. Efficient iterative schemes for ab initio total-energy calculations using a plane-wave basis set. Phys. Rev. B, 54:11169, 1996.;

(5) J. P. Perdew, K. Burke, and M. Ernzerhof. Generalized gradient approximation made simple. Phys. Rev. Lett., 77:3865, 1996; J. P. Perdew, K. Burke, and M. Ernzerhof. Erratum: Generalized gradient approximation made simple. Phys. Rev. Lett., 78:1396, 1997.

(6) Behler, J., and Parrinello, M. (2007). Generalized neural-network representation of highdimensional

potential-energy surfaces. Physical Review Letters, 98(14), 1–4.

(7) Cheng, T., Huang, Y., Xiao, H., and Goddard, W. A. (2017). Predicted Structures of the Active Sites Responsible for the Improved Reduction of Carbon Dioxide by Gold Nanoparticles. Journal of Physical Chemistry Letters, 8(14), 3317–3320.

(8) Glorot, X. and Bengio, Y. (2010). Understanding the difficulty of training deep feedforward neural networks. Proceedings of the 13th International Conference on Artificial Intelligence and Statistics, 9, 249–256.

(9) Hori, Y., Takahashi, I., Koga, O., and Hoshi, N. (2002). Selective formation of C2 compounds from electrochemical reduction of CO_2 at a series of copper single crystal electrodes. Journal of Physical Chemistry B, 106(1), 15–17.

(10) Feng, X., Jiang, K., Fan, S., and Kanan, M. W. (2016). A Direct Grain-Boundary-Activity Correlation for CO Electroreduction on Cu Nanoparticles. ACS Central Science, 2(3), 169–174.

(11) Morris Wang, Y., Sansoz, F., Lagrange, T., Ott, R. T., Marian, J., Barbee, T. W., Hamza, A.V. (2013). Defective twin boundaries in nanotwinned metals. Nature Materials, 12(8), 697–702.